Electrostatically gated nanofluidic membranes: Technological developments and use of electrochemically polarizable materials

THÈSE N^{O} 8366 (2018)

PRÉSENTÉE LE 9 MARS 2018

À LA FACULTÉ DES SCIENCES ET TECHNIQUES DE L'INGÉNIEUR
LABORATOIRE DE MICROSYSTÈMES 4
PROGRAMME DOCTORAL EN MICROSYSTÈMES ET MICROÉLECTRONIQUE

ÉCOLE POLYTECHNIQUE FÉDÉRALE DE LAUSANNE

POUR L'OBTENTION DU GRADE DE DOCTEUR ÈS SCIENCES

PAR

Stefano Silvio Giovanni VARRICCHIO

acceptée sur proposition du jury:

Dr G. Boero, président du jury
Prof. Ph. Renaud, directeur de thèse
Prof. L. Bocquet, rapporteur
Prof. T. Braschler, rapporteur
Prof. M. Gijs, rapporteur

ÉCOLE POLYTECHNIQUE
FÉDÉRALE DE LAUSANNE

Suisse
2018

"Tactics is what you do when there is something to do;
strategy is what you do when there is nothing to do."
— Ksawery Tartakower

"Cu mancia faci muddichi."
— Proverbio Siciliano

Dedicato a mia Madre.
Ma anche a mio Padre.

Acknowledgements

A PhD thesis is an individual work shaped by the many contributions received during four years. I have to thank many persons for those contributions –on the technical/scientific level but, and expecially, on the personal level– without whom my work wouldn't have been possible.

First I would like to thank my thesis advisor, **Prof. Philippe Renaud** for the freedom I have been granted during those years al LMIS4, for the time he dedicated me (an increasingly rare quality in nowadays academia), and for the solid trust he always demonstrated in me, my project and my capabilities. If I look back at the past four years I realize which privilege I had doing my thesis under his direction and how much I have learned from him in terms of critical thinking and problem solving.
I would like to thank the members of my jury, **Prof. Lyderic Bocquet**, **Prof. Thomas Braschler**, **Prof. Martin Gijs** and **Dr. MER Giovanni Boero** for their critical review of my thesis and their constructive inputs.
My deepest gratitude goes to **Dr. Arnaud Bertsch**, probably the person with whom I interacted the most during my thesis, for the liters of red ink consumed for corrections of my texts/presentations/talks, and the hours of discussion spent to motivate me, to criticize my work and to contribute with brilliant ideas to my day-to-day struggles. His contribution is invaluable to me and his direct, often tough but sincere criticism appeared to be one of the most useful things happened during my thesis, which greatly helped me to acquire a new perspective on my own work when I was stuck in a local minima.
I would like to thank **Ludovic**, **Guillaume**, and **Joan** for having shared our Beautiful office In those years As long as the (few) celebraTions of our sucCesses and (abundant) disappointment when things went wrong. I would like to add tHat eating microwaved smElly fish right at the desk may not the the brighteSt of the ideas if healthy office relationship want to be preserved.
I would like to acknowledge the contribution of **Clarisse**, **Fatemeh** and **Margaux** with whom I had the chance to interact every time I had one idea/project/problem that could be somehow related to biology and biochemistry and of **Benoît "ca-c-est-cool" Desbiolles** for his disturbingly positive attitude (at least for a PhD student) and for being such a cool guy.
I'm grateful to the other persons working with nanofluidics at LMIS4, **Thomas**, **Davide** and **Mojtaba**, for the fruitful debates and especially to **Fabien** for having taken the time to coach me at the beginning of the thesis and having introduced me on the subject of nanofluidics.
This work would not have been possible without the master students **Nicolas Maïno** and **Mohamed**, that contributed to some aspects of the thesis with their time and curiosity. Partic-

ularly, thanks to **Brad Petkus** for having worked during nine long months under my supervision, for his commitment and positive attitude, and for having shared with me and the entire laboratory some "curious" aspects of the north-american culture.
Overall I had the chance to join a group composed of open and supportive people ready to share their advices and experiences as well as their after-work time. I would like therefore to thank the other lab members, **Amelie**, **Elodie**, **Richard**, **Marc**, **Tugba**, **Patrick**, **Jonathan**, both **David**, **Harald** and former members of LMIS4 with whom I interacted mostly on the personal level, for having created such nice environment.
I am also thankful to **Sylvie Clavel**, **Christine Vuichoud**, **Marie Halm** and **Lucie Auberson** for taking care of the administrative side and overall for having made my life so much easier during the last years.

A great share of this thesis was done in the CMi cleanroom. This state of the art facility provides the students with excellent equipment and technical support for micromachining process. The real strength of the CMi and what makes it a great place to work –beside the stable temperature of 21 °C– is the outstanding competence and commitment of its staff.
Therefore I would like to thank **Dr. Cyrille Hibert** for the countless hours of discussion, the endless good ideas, the last-minute debugging and overall for his constructive perspective on my project. Indeed, the idea of using templates to fabricate nanoporous membranes was born during from one (long) discussion with him. I would like to thank **Joffrey**, **Dzenek**, **Didier**, **PAM**, **Rémy**, **Giovanni**, **Kaspar** and the other members of the **CMi staff** for the things they taught me in those years, for keeping running around fixing our mess and overall for the good mood and positive environment they create in the cleanroom. Furthermore I would like to thank **Michail Zervas**, **Valentin Flauraud**, **Marta Jole Ildefonsa Airaghi Leccardi** (MAL for friends), **Elmira Shahrabi**, and **Laszlo Toth**, heavy CMi users, for having shared their precious tips and tricks and having somehow made with their brightness and spirit, the cleanroom a lighter place.

I would like to thank **Dmitry Mikulik**, **Pablo Romero Gómez**, and **Jelena Vukajlovic** from the laboratory of **Prof. Anna Fontcuberta i Morral** for the fruitful collaboration.
I am grateful to **Raphaël Trouillon** from the group of Prof. Gijs for the stimulating discussions and overall for having contributed with his experience with electrochemistry of carbon to some paragraphs of chapter 4 and as a coauthor of one paper.
Moreover I would like to express my sincere gratitude to the whole Intento team for giving me the chance to collaborate with a dynamic and interesting start-up project, and especially to **Andrea Maesani** for shoving me the importance of having an optimistic vision projected toward the future.

Success is not abundant in a PhD thesis, therefore becomes important to be ready to celebrate the positive results. For this I must thank the *"late lunchers"* group and more specifically **MC Letizia**, **Pietro**, **Marco**, **Matteo** and **Pierre** for being always ready and present to share a beer and a laugh (in this order) at Satellite.

I would like to spend some more lines to thank some professors and teachers that played an important role during my entire life as student. Thanks to **Prof. Martin Gijs** for having for the first time opened my eyes on this new micro-world with his class "technologies of

microstructures" and for having supported me in many occasions and on many levels during my whole time at EPFL ; thanks to **Prof. Niels Quack** for his help during my period at UC Berkeley and for his always pertinent, sharp and constructive remarks on my work ; thanks to **Prof. Sebastian Maerkl** for having thought me that *"a thesis is what you make out of it"*, words to which I tried to stick as much as possible during my PhD ; thanks to **Prof. Dario Floreano** for having somehow facilitated my arrival at LMIS4 and having thought me the importance of words in nowadays academia ; ed infine grazie a **Mirko Tantardini** che tanti anni fa per primo mi ha introdotto ai princípi del pensiero logico ed all'importanza del rigore.

Un grazie di cuore agli amici di una vita **Tenne**, **Frigi**, **Fuma**, **Bina**, **Nicola Pestalozzi**, **Cristy** e **Alessandra** ed agli amici più recenti **Nicola Foletti**, **Diego**, **Mariano** e **Thommy** per il sincero affetto ed i bei momenti passati assieme; grazie a **Nicola Deluigi** per il mutuo sostegno negli anni di tesi e per essere un pessimo attaccante a calcetto; a **Luca Sulmoni** per i lunghi(ssimi) pranzi a Sat durante i quali partite a scacchi e calcetto vincevano sul senso di colpa per non lavorare; a **Davide D'Amico** per le ossigenanti avventure alpine, a **Seb** ed **Elisa** per l'affetto ed il supporto morale (ma non per saper cucinare la carbonara); ad **Alice** e **Chiara** per essere state coinquiline e amiche nell'ultima decade; a **Bizzo**, **Silvio** e **Loïc** per le belle (ma corte) vacanze passate insieme; ed infine a **Raffaele Storni** per le settimanali, dolorosissime, bastonate a squash.
Un pensiero particolare va a **Niccoló Piacentini**, che negli ultimi anni ho scoperto essere un insegnante competente, un ascoltatore paziente, ed un amico sincero.
Sono inoltre profondamente grato a **Brunella** per un mucchio di cose ma in particolare per i bellissimi anni passati insieme, per avermi insegnato a cucinare la pasta con (pochi) broccoli e (tanta) pancetta, per essere stata un inestimabile supporto negli ultimi difficili mesi di tesi col collaudato metodo del bastone (tanto) e della carota (poca) ma soprattutto per i tanti, tanti sorrisi condivisi.
É per me molto importante inoltre ringraziare **Zia Nicky** e **Zia Anna** con le rispettive famiglie e la famiglia **Bellomo** ma in particolare mio **Zio Fabio** e famiglia per la vicinanza, l'affetto e il sostegno negli ultimi due anni che si sono rivelati piuttosto agitati sul piano famigliare.

Vorrei infine ringraziare mio fratello **Gabriele** per avermi mostrato come rimettersi in continuazione e testardamente in gioco e non sedersi sugli allori, mio padre **Marco** per avermi trasmesso la resilienza ed energia necessaria a portare a termine una tesi, e mia madre **Paola** per il suo supporto ed amore incondizionato e più recentemente per avermi dimostrato come affrontare gli imprevisti a testa alta.

Lausanne, 5 January 2018

Stefano Varricchio

Abstract

Solid-state nanoporous membranes able to control ionic flows at the molecular level could have important applications in fields of research such as water filtration, nanomedicine, energy production, drug delivery, and bio-chemical analysis. The ability to dynamically control the surface charge and the electrical potential inside nanopores extends the range of applications from passive to active devices, such as nanofluidic transistors.

In the first part of the thesis a new wafer-scale manufacturing method for solid-state nanoporous membranes based on casting of sacrificial templates is proposed. This way it is possible to individually define the position and geometry of every nanopore by design, independently from the materials used, which make this fabrication strategy adapted to the manufacturing of both passive and active nanofluidic devices.

In the second part of the thesis this technology was used to fabricate electrostatically gated nanofluidic membranes with nanopores integrating polarizable electrodes made of amorphous carbon inside the nanochannels. Those membranes demonstrated the ability to modulate the transmembrane ionic conductivity *via* the variation of the surface charge of the nanochannels with low voltages (800 mV) and modulation factors close to 100%.

Key words: nanofluidics, nanopore, transistor, polarizable electrode, flow modulation, silicon nanostructure

Sommario

Le membrane nanoporose, capaci di controllare il flusso di ioni a livello molecolare, hanno svariate applicazioni in numerosi campi di ricerca. Il filtraggio delle acque, la nano-medicina, la produzione di energia, ed il rilascio controllato o la detezione di bio-molecole sono alcuni esempi. Nello specifico, l'abilità di controllare dinamicamente la carica di superficie all interno dei nanopori estende la gamma di applicazioni di tali membrane da passive ad attive, delle quali l'esempio piu rappresentativo sono i transistor nanofluidici.
Nella prima parte di questo lavoro viene proposto un metodo innovativo e *wafer-scale* per la fabbricazione di membrane nanoporose basato sull utilizzo di nanostrutture sacrificali come stampo per i nanopori. Tale approccio rende cosi possibile definire posizione e geometria di ogni nanoporo tramite design, indipendentemente dai material usati, rendendo perciò questa strategia di fabbricazione adatta ad ottenere sia nanopori attivi che passivi.
Nella seconda parte della tesi, questa tecnica di fabbricazione é stata usata per ottenere membrane nanofluidiche a controllo elettrostatico effettuato tramite elettrodi polarizzabili in carbonio amorfo integrati in ogni singolo nanoporo. Le membrane cosi realizzate si sono dimostrate capaci di controllare la conduttività ionica dei nanopori tramite la diretta modulazione del potenziale di superficie dei nanopori stessi, a bassi voltaggi di gate ed esibendo fattori di modulazione vicini al 100%.

Parole chiave: nanofluidica, nanoporo, transistor, elettrodo polarizzabile, modulazione dei flussi, nanostrutture in silicio

Contents

Acknowledgements **i**

Abstract (English/Italiano) **v**

List of figures **xiii**

1 Introduction **1**
1.1 Working principles . . . 1
1.1.1 Surface charge . . . 2
1.1.2 The Electrical Double Layer (EDL) . . . 2
1.1.3 EDL overlap and permselectivity . . . 3
1.2 Flow modulation at the nanoscale . . . 4
1.2.1 Diffusion and convection . . . 4
1.2.2 Electrokinetic flows . . . 6
1.3 State of the Art . . . 8
1.3.1 Semiconductor-like applications . . . 9
1.3.2 Filtration of solutions and reverse osmosis . . . 10
1.3.3 Preconcentration . . . 11
1.3.4 Nanomedicine . . . 12
1.4 Motivation and project statement . . . 14

2 Fabrication of solid-state nanoporous membranes through sacrificial silicon templates **15**
2.1 Concept . . . 16
2.2 Sacrificial silicon nanostructures . . . 18
2.2.1 Method . . . 19
2.2.2 Results . . . 19
2.2.3 Discussion . . . 23
2.3 Directional deposition . . . 24
2.3.1 Method . . . 25
2.3.2 Results . . . 26
2.3.3 Electrical characterization . . . 29
2.3.4 Discussion . . . 30
2.4 Conformal deposition . . . 32

2.4.1 Method . . . 32
2.4.2 Results . . . 34
2.4.3 Electrical characterization . . . 38
2.4.4 Discussion . . . 39
2.5 Conclusion . . . 41

3 Theoretical functioning of a nanofluidic transistor 43
3.1 Surface charge . . . 44
3.2 The Electrical Double Layer (EDL) . . . 44
3.3 Poisson-Nerst-Planck-Stokes model . . . 45
3.4 Poisson-Boltzmann equation . . . 46
3.5 Debye-Hückel approximation . . . 48
3.6 Surface potential vs. surface charge - the Grahame equation . . . 51
3.7 Electrokinetic flows . . . 52
3.7.1 Microchannel with thin EDL . . . 52
3.7.2 Nanochannel with thick EDL . . . 53
3.8 Current modulation in a nanofluidic transistor . . . 54
3.8.1 Ideal solution - point-charge ions . . . 55
3.8.2 Steric correction of the ideal solution . . . 56
3.8.3 Discussion . . . 59
3.9 Conclusions . . . 60

4 Nanofluidic transistor with polarizable gate 61
4.1 Motivation . . . 61
4.1.1 Case study . . . 62
4.2 Polarizable electrode . . . 64
4.3 Choice of polarizable material . . . 66
4.3.1 Amorphous carbon as candidate for polarizable electrodes . . . 67
4.3.2 Results . . . 69
4.4 Fabrication of nanoporous membranes . . . 71
4.5 Measurements . . . 72
4.5.1 Setup description . . . 72
4.5.2 Gate leakages and equivalent circuit . . . 73
4.5.3 Quantification of leakage currents . . . 74
4.6 Results and discussion . . . 75
4.6.1 Test description . . . 75
4.6.2 Results . . . 76
4.6.3 Electrode stability over time . . . 78
4.7 Discussion . . . 79
4.8 Conclusions . . . 81

5 Conclusion **83**
5.1 Summary of results 83
5.2 Outlook 84

A Fabrication details for the nanoporous membrane **87**

Bibliography **89**

Acronyms **99**

Curriculum Vitae **101**

List of Figures

1.1 Surface charge and EDL . . . 3
1.2 EDL overlap: channel dimension vs. λ_D . . . 4
1.3 Electroosmosis and electrophoresis . . . 7
1.4 Pore dimension for different filtration membranes . . . 11
1.5 Principle of ion concentration polarization . . . 12
1.6 Nanoporous membrane for the release of chemicals . . . 13

2.1 Concept of nanopore fabrication through sacrificial templates . . . 17
2.2 Process-flow for the fabrication of Si templates . . . 18
2.3 Image processing and analysis of Si templates . . . 20
2.4 Si templates minimal CD vs. height . . . 21
2.5 Cylindrical Si nanotemplates characterization . . . 22
2.6 HSQ stability vs. critical dimension and geometry . . . 22
2.7 Influence of shape on stability of templates . . . 23
2.8 Influence of pattern density on the fabrication of Sitemplates. . . . 25
2.9 Process flow for evaporated membranes . . . 26
2.10 Cross-section of evaporated membrane before release . . . 27
2.11 Evaporated membrane after release . . . 28
2.12 Multilayered membrane made of 7 alternated layers of Pt and SiO_2 . . . 28
2.13 Effect of tilted evaporation . . . 29
2.14 I-V curve of two evaporated membranes . . . 31
2.15 Process flow for conformally deposited membranes . . . 33
2.16 Effect of templates pitch on membrane geometry . . . 35
2.17 Planarization with CMP and IBE . . . 36
2.18 Conformal membrane before release . . . 37
2.19 Conformal membrane after release . . . 38
2.20 I-V curve of conformal membranes . . . 39

3.1 EDL structure . . . 45
3.2 Debye length λ_D vs. ionic strength . . . 47
3.3 Semi-infinite domain: Co- and counter-ion concentration in the EDL . . . 49
3.4 Parallel plates domain: Co- and counter-ion concentration in the EDL . . . 50
3.5 Grahame equation and Debye-Hückel approximation . . . 52

3.6 Current and ionic concentration modulation - Point charge model 56
3.7 Comparison point charge - hard sphere models 58
3.8 Current and ionic concentration modulation - Hard sphere model 59
3.9 Current and ionic concentration modulation - Hard sphere model, low saturation 60

4.1 Schematics of a nanofluidic transistor 62
4.2 Diffusive, electrophoretic and electroosmotic flows in a nanofluidic transistor . 63
4.3 Metal-Oxide electrode vs. Polarizable electrode 64
4.4 Types of carbon depending on their atomic structure 67
4.5 Electrochemical cell for characterization of carbon films 68
4.6 Cyclic voltammetry of different types of carbon 69
4.7 Process flow for a nanofluidic transistor 72
4.8 Setup measurement 73
4.9 Gate leakage quantification 74
4.10 I-V characteristic in function of V_G 75
4.11 Nanofluidic transistor fabrication result 76
4.12 Modulation factor of the nanofluidic transistor 77
4.13 Evolution of the modulation factor over time 78
4.14 Contamination EDX analysis 79

1 Introduction

This introductory chapter gives an overview of the properties and characteristics of fluids when confined in channels of nanometric dimensions. The chapter does not delve in the details of physics but rather introduces the basic principles of nanofluidics and their applications to control flows at the molecular level. To conclude, the goal of this thesis are stated and contextualized with respect to the state of the art.

Definition Nanofluidics is defined as the study of the properties of fluids confined in cavities with at least one dimension smaller than 100 nm. Such properties can be exploited to fabricate devices able to precisely control the motion of liquids and molecules at the nanometer scale.[1]
Although properties of fluids at the nanometer scale or in close proximity of a surface have been studied in the past from traditional fields of science such as physics, chemistry, fluid mechanics, and biology, the terminology *"nanofluidics"* has been devised only recently with the advent of nanotechnology to distinguish the field from the expansion of microfluidics in the 1990.
Nanofluidics is therefore the interface of many fields of research and it is difficult to affirm whether it belongs to physics, chemistry, fluid mechanics, surface science, materials science or others, because it borrows concepts from –and contributes to– all the previously mentioned disciplines (and more).

1.1 Working principles

When reducing the dimension of the container where a liquid is confined, surface effects slowly start to take over bulk effects. At the millimeter scale the surface tension of the liquid begin to

dominate the gravity, allowing small droplets to withstand their weight and stick to surfaces. At the micrometer scale the viscosity of the liquid overcomes the inertial forces, allowing to observe the laminar flows on which most microfluidics applications are based on. At the nanometer scale, the presence of an electric double layer (EDL) that stems from chemical reactions at the solid-liquid interface, results in a non-uniform electrical charge distribution that has numerous consequences. As intuitively described by Whitesides, nanofluidic systems are, in other words, "all-interface".[2]

1.1.1 Surface charge

Let's consider an aqueous solution in contact with a solid surface. At equilibrium, a net surface charge density σ appears at the interface solid/electrolyte following two distinct mechanisms shown in figure 1.1 - left.[3, p. 291]

Ionization: By ionization or dissociation of surface groups. For example a silicon dioxide surface in contact with an aqueous electrolyte is rich in silanol groups SiOH which, after acidic dissociation, leaves behind a negatively charged surface, SiO^- + H^+.[4, p. 229]

Adsorption: By adsorption of ions from the solution onto the surface. For example the adsorption of Ca^{2+} ions to COO^- sites.

Those two phenomena are extremely common, resulting in almost any solid surface in contact with a liquid to acquire a net surface charge.

1.1.2 The Electrical Double Layer (EDL)

Because of the surface charge an electric field is established in close proximity to the surface independently from the charge regulation mechanism. The electrostatic forces generated results in an accumulation of ions of opposite charge (counter-ions) and a depletion of ions of the same charge (co-ions) close to the surface (Figure 1.1 - right). This region of non-uniform ionic charge density is called the *electric double layer (EDL)*. Further away from the surface the accumulation of counter-ions is counterbalanced by the Brownian motion of ions and therefore the ionic charge density exponentially fades to the values of the bulk. The extension of the EDL in the bulk is defined by the Debye length λ_D.
The term *"Double Layer"* stems from the presence of two regions with opposite charge, the surface and the accumulation of counter-ions, which simplified electrical model is a capacitor. The extension of the EDL is therefore dependent from the ionic strength of the electrolyte since at higher ionic strength the osmotic pressure from the bulk toward the charged surface increases, which decreases the extension of the EDL.

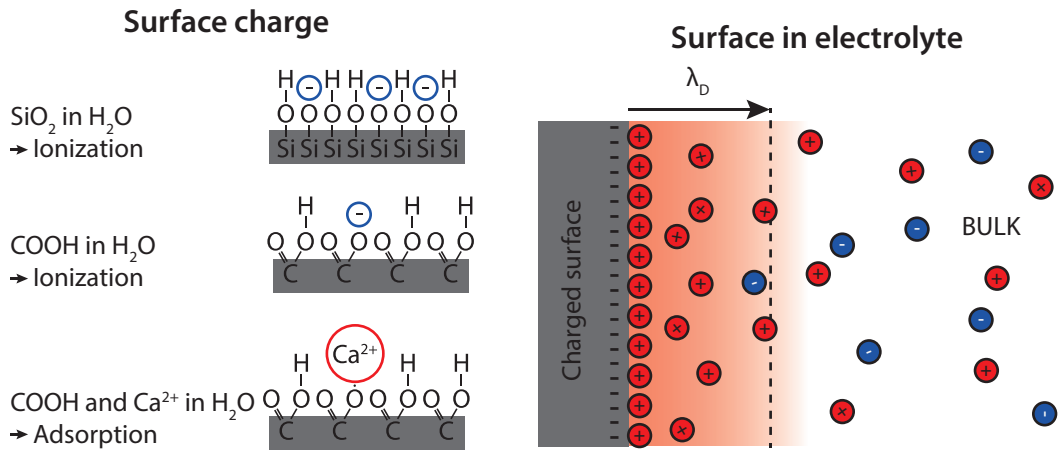

Figure 1.1 – **Left** Representation of mechanisms originating surface charge in case of SiO_2, COOH and COOH + Ca^{2+}. **Right** Representation of the EDL overlap inside a channel with radius $r < \lambda_D$. The channel presents an accumulation of counter-ions and a depletion of co-ions.

1.1.3 EDL overlap and permselectivity

When using channels with dimensions larger than the EDL, most of the liquid inside the channel, and therefore the channel itself, has the same charge density, ionic conductivity and pH as the bulk, the EDL being evanescently thin and therefore negligible compared to the dimension of the channel as shown in figure 1.2 - left. This approximation is not valid with channels smaller or with dimensions comparable to λ_D (typically the distinction is made for channels smaller than 100 nm), since at this scale the portion of the channel that has the properties of the EDL rather than the bulk isn't negligible anymore. In particular, when the critical dimension of the channel is smaller than $2 \times \lambda_D$, the EDL of the channel walls overlaps, and therefore the entire volume of the nanochannel can be considered as part of the EDL (figure 1.2 - right).

This phenomenon, called *EDL overlap*, alters the properties of nanochannels compared to the bulk proportionally to the magnitude of the EDL overlap. First, the electrical conductivity of the nanochannel is increased given the increased concentration of charge carriers; second, the repulsion of co-ions and enrichment of counter-ions results in channels which permittivity depends on the valence of the ionic species. Such preferential permeation for a specific ion through the nanochannel is defined as *permselectivity*. This phenomenon is related to the ionic strength of the electrolyte since it depends on the EDL overlap.
As an example, let's consider a nanochannel with diameter of 20 nm, filled with an electrolyte with ionic strength of 100 mM. At this ionic strength the Debye length λ_D is smaller than the diameter of the channel ($\lambda_D = 1$ nm) therefore the absence of the EDL overlap let the ions equilibrate in the middle of the channel where the concentration of both co- and counter-ions is equivalent to the bulk concentration $c_{0,\infty}$.
On the other hand, with the same channel geometry but with a liquid at a lower ionic strength of 0,1 mM, the Debye length becomes larger ($\lambda_D = 30$ nm) and the EDL overlaps in the center

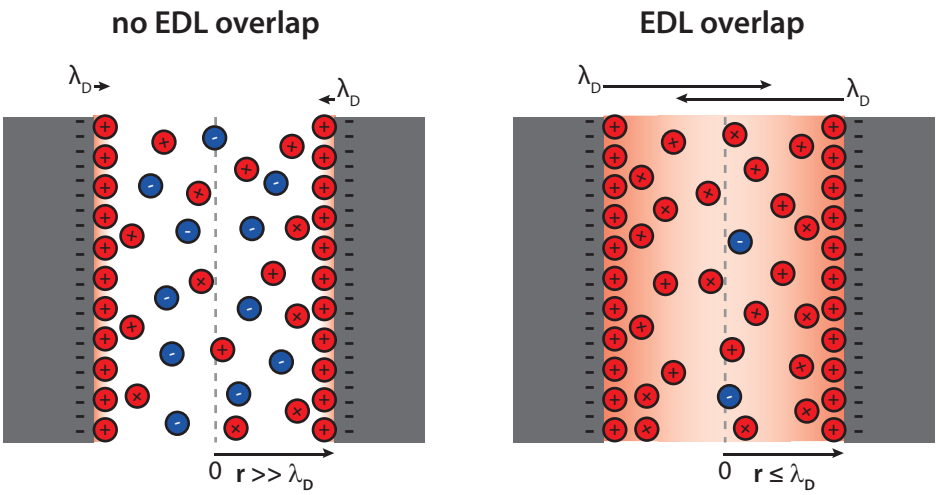

Figure 1.2 – Comparison between a *micro*-channel (**left**), without EDL overlap, and a *nano*-channel (**right**), with EDL overlap in the middle of the channel.

of the channel, where the potential cannot be considered null anymore. This results in a net accumulation of counter-ions in the nanochannel and in the partial exclusion of co-ions (in red and in blue respectively in figure 1.2).

1.2 Flow modulation at the nanoscale

1.2.1 Diffusion and convection

Definitions *Diffusion* is defined as the migration of molecules deriving from their Brownian thermal agitation.[4, p. 80] It is a stochastic process that tends to equilibrate the properties of a liquid volume as time goes on and can be observed as a net flow in the opposite direction of a concentration gradient. This phenomenon is described by Fick's law, which defines for a species i, the flow $\vec{j}_i$ as a function of its concentration spacial distribution c_i and its diffusion coefficient D_i as

$$\vec{j}_{i,\text{diff}} = -D\nabla c_i \tag{1.1}$$

Considering a molecule in a mono-dimensional system the time t that a particle would need to travel a distance x is given by the relationship $t = x^2/D_i$.
Convection on the other hand is defined as the transfer of a specie i by the movement of its surrounding medium $\vec{u}$ which leads to the convective species flux as $\vec{j}_{i,\text{conv}} = \vec{u} \cdot c_i$. The velocity of a fluid $\vec{u}$ is described by the well-known Navier-Stokes equation (further discussed in section 3.3).

Macro vs. nanoscale – The Reynolds number Mass transport at the macro and nano scale is governed by different mechanisms. Inertial forces, typically the cause of turbulences and convection in a fluid are related to the mass of the displaced liquid and therefore its volume, so they scale with the cube of the characteristic dimension of the system. Viscous forces on the other hand are opposed to this movement and depends on the the surface of the displaced volume, so they scale following the square of the characteristic dimension of the system.
At the macro-scale the mass transport is dominated by convective flows that literally carry the molecules from one side to the other of the volume under examination. When scaling down the system, the inertial terms decreases faster than the surface ones and, at a certain dimension, the viscous forces become dominant. This relationship is represented by the *Reynolds number, Re* a dimensionless number that estimate the behaviour of a liquid depending of the characteristic dimension of its container L the density ρ and dynamic viscosity η of the fluid, and u its velocity

$$Re = \frac{F_{\text{inertial}}}{F_{\text{viscous}}} = \rho \frac{Lu}{\eta} \tag{1.2}$$

Systems with $Re < 0.1$ describe systems for which the viscous forces dominates over the inertial forces,[4, p. 179]. For systems of small Reynolds number $Re < 0.1$, the Navier-Stokes equation can be approximated by the linear Stokes equation by removing the unsteady and turbulent terms (as further discussed in section 3.3, equation 3.6) and the resulting flow is designed as Stokes flows or creeping flows. Since the unsteady terms are neglected, the flow acquire properties that are not present at the macro-scale, namely symmetry and reversibility in time. This results in a typical behaviour of the fluid flowing in parallel sheets without mixing. Liquids in nanochannels where $L \leq 100\,\text{nm}$ typically fall in this category.
As an example let's consider a nanochannel of 100 nm (which is considered as the upper bound to define a nanochannel [2]), filled with an aqueous solution of density $1\,\text{kg}\,\text{m}^{-3}$ and viscosity of $1 \times 10^{-3}\,\text{Pa}\,\text{s}$ (at 293 K)[3, p. xxviii]. In order for this system to overcome the limit of Stokes flows of $Re \leq 0.1$ the liquid should flow in the channel at a velocity of $u = 1000\,\text{m}\,\text{s}^{-1}$, which is irrealistic.

Convection vs. diffusion - the Peclet number When further reducing the dimension of the systems from the micrometer to the nanometer scale, the Reynolds number reduces drastically, while on the other hand the diffusive flows become dominant. The relationship between the convective and diffusive flows is represented by the Peclet number *Pe*

$$Pe = \frac{j_{\text{advective}}}{j_{\text{diffusive}}} = \frac{Lu}{D_i} \tag{1.3}$$

A high Peclet number represents a system where diffusion has a negligible impact on the flow of species which is typical of macro-scale systems. A low *Pe* on the other hand is typical of micro and nano-systems and describes flows where diffusion dominates on advection. As

an example, let's consider the same relatively big nanochannel as before, with $L = 100\,\text{nm}$ filled with an acqueous solution of KCl, a symmetric electrolyte with diffusion coefficient $D_{\text{KCl}} = 2{,}0 \times 10^{-9}\,\text{m}\,\text{s}^{-1}$ (see paragraph 3.4). In order for the advective forces to overtake the diffusive ones (i.e. $Pe \geq 1$) the flow velocity must be at least equal to $u = 20\,\text{cm}\,\text{s}^{-1}$, which is, again, not realistic. This demonstrate how nanochannels are completely dominated by diffusion and how advective forces can be usually neglected.

1.2.2 Electrokinetic flows

Definition Let's consider a particle with charge q immersed in external electrical field $\vec{E}$. The particle is subject to an electrostatic force known as the Coulomb force expressed as $\vec{F} = q\vec{E}$.[3, p. 55]
In the case of a charged particle in a liquid electrolyte, the motion of ions following an external electric field is defined by two electrokinetic phenomena named *electrophoresis* and *electroosmosis*.
The term *Electrophoresis*, derived from the greek *phoresis* = *"being carried"*, defines the migration of a charged particle under the influence of Coulomb force exerted by an external electric field.
The term *Electroosmosis* is defined as the motion of a *liquid* in response to one applied electric field. Contrary to electrophoresis, which is referred to the movement of single ions, electroosmosis is a property of the liquid. This flow is typically equal to zero in a bulk with equilibrated charge density $\rho = 0$, but results in a net flow when the volumic charge is non-uniform as is in the EDL. Since the electroosmotic flow (EOF) is proportional to the volume (and therefore the extension) of the EDL, the magnitude of the EOF is dependent on the ionic strength of the electrolyte, which is not the case for electrophoretic flow (EP). Both electrophoresis and electroosmosis are well known phenomena with an extensive literature about principles and applications. The interested reader is referred to *"Micro-and nanoscale fluid mechanics: transport in microfluidic devices"* from J. Kirby for further informations.[4]

Isolated particle and micro-nano channels Let's consider the case of a charged particle suspended in an electrolyte and immersed in an electric field (figure 1.3, left). The particle is then subjected to two different forces: first, the Coulomb force exerted from the external electric field attracts the particle toward the electrode of opposite polarity to its own charge. Second, the solvent surrounding the particle, since its volumic charge is non-null and rich in counter-ions, under the influence of the same electric field, is attracted in the opposite direction, resulting in a viscous drag on the particle. For a single particle those two forces results in the EP and EOF which are always of opposed direction since the charged particle and the EDL surrounding it are of opposed polarity. At low ionic strengths the EOF will be dominant because the larger extension of the EDL results in a bigger volume of electroosmotic flow, whereas at high electrolyte concentration the EOF will be much smaller and the EP will

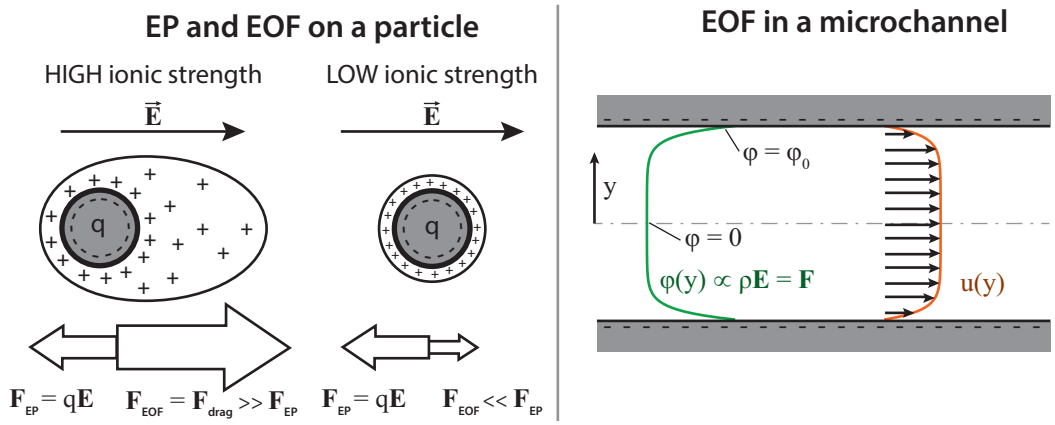

Figure 1.3 – Graphical representation of electrophoretic flow (EP) and electroosmotic flow (EOF) for both a charged particle and a micro channel.

dominate.

Similarly, let's consider a liquid-filled micro-channel with dimension $r \gg \lambda_D$ and with a net surface charge immersed in an electric field. In this case the EDL is present at the channel walls, so when an external electric field is applied, the EDL moves along the external electric field dragging the liquid at the center of the channel through viscous interaction, resulting in a net EOF in the channel (figure 1.3, right). The movement of liquid across a channel creates one accumulation of the solvent on one side of the channel, resulting in a so-called *electroosmotic pressure* opposed to the movement of the liquid itself.

The opposite phenomena arise when an electrolyte is forced through a nanochannels through an external pressure, resulting in an electrical potential difference observed at the extremities of a channnel, called *streaming currents*. This principle is extensively used in microfluidics either to build electroosmotic pumps or to control flows.

A peculiarity of EOF flows is the velocity profile across the microchannel which presents a characteristic "flat" profile, in opposition to pressure-driven flows where the velocity has a parabolic profile. This flat velocity profile is particularly useful in chromatography techniques since it strongly reduces the dispersion of molecules and therefore increases the resolution of the system.

In the case of nanochannels, the observed EOF is not any more the result of the viscous drag of the moving EDL on the liquid at the center of the channel, since most of the volume of the nanochannel itself *is* the EDL. This means that first, the system has a lower inertia and therefore responds more rapidly to the variations of the external voltage; second, that in the case of a charged particle entering the nanochannel, the EP and EOF would not be opposed anymore, the counter-ions being strongly depleted inside the nanochannel.

Summary In nano-sized capillaries the EDL overlap engender an enrichment of counter-ions inside the channel which, since transport of species is dominated by diffusion ($Pe \ll 1$), drastically influences the migration of counter-ions across the channel. Given the high fluidic resistivity and low Reynolds number of nanochannels ($Re \ll 1$), flow control is often achieved with EP and EOF rather than with pressure differentials.

1.3 State of the Art

Motivation Peculiar behaviour of fluids confined in nano-channels are dictated by the dominance of liquid-solid interactions over bulk properties. The study of interfacial fluids inside nanochannels is motivated from the need to provide a better understanding in different fields of science and engineering such as storage of energy in capacitors and batteries, corrosion, lubrication and adhesion, molecular recognition, sensing and biocompatibility. [2]
Biological systems are particularly efficient in exploiting properties of nanofluids such as permselectivity and ion exclusion to actively control fluxes of ions or proteins across the lipid bilayer of a cell. However, engineering biological nanopores is a difficult task since those category of nanopores are typically sensitive to environmental parameters such as pH, mechanical stress, high voltages, and thermal fluctuations and their modification requires to precisely control the synthesis of a mutant nanopore and its proper refolding, both technical challenges that nowadays are difficult to overcome.[5], [6] On the other hand, solid-state nanopores exhibit greater stability than their biological counterparts and the techniques to manufacture them in a controlled way are abundants. Being able to reliably engineer and modulate the properties of artificial nanochannels, mimicking this way the control of ionic and molecular flows exhibited by transmembrane proteins, would revolutionize many different applications.[7], [8] In this section are discussed the principal ones.

Early stages In the past, before the term *"nanofluidics"* was even devised, properties of nanofluids were exploited for industrial filtration and separation. Track etched and Nafion membranes are the most significant examples.
Track etched nanoporous membranes (present on the market since 1970) are filtration membranes made of a thin sheet of polymeric material. The nanopores are obtained in a two step process: first the irradiation of the polymer sheet with heavy ions locally damages the polymer and chemically modifies its structure, second the latent track of the ion is transformed into a hollow nanopore by a chemical etching. This way it is possible to obtain nanopores in the range of 10 nm to 3000 nm and up to tenths of micrometers long, depending of the materials used.[9]
Nafion membranes were introduced by DuPont in the late 1960 and, given their high proton conductivity and small pore dimension, are considered to be the better choice for proton-exchange membranes. They are obtained through copolymerization of two components, vinyl ether comonomer and tetrafluoroethylene (TFE), which results in an intrinsecally nanoporous material with pores in the range of the single nanometer (typically 4 nm). [10], [11].

What made track-etched and Nafion membranes commercially successful is the possibility to fabricate big surfaces with little cost without losing control over pore dimension and pore density. Those approaches are however limited if the geometry and material of nanopores need to be finely engineered to mimic the complex behaviour of biological nanopores.

Since those early stages, progress in microfabrication, material science and metrology, issued mainly from fabrication techniques for microelectronics and micro electromechanical systems (MEMS), provided the field of nanofluidics with the tools to build devices for new applications based on the *active* control of fluids at the molecular level.[12]

1.3.1 Semiconductor-like applications

Different analogies can be found between the transport of charged species in electrolytes and the transport of electrons/holes in semiconductors: the laws governing electrofluidic phenomena are almost identical to the ones that describe drift-diffusion in semiconductors and in both cases the flow of current is determined by the migration of charged species in response to thermal fluctuations and electric fields accordingly to Boltzmann statistics.[13], [14]
Such parallelism between nanofluidic and semiconductor devices has been widely exploited to fabricate nanofluidic equivalents of electrical components such as nanofluidic diodes and nanofluidic transistors. Those nanofluidic devices are capable to control the ionic flow through a nanochannel as their electronic counterpart controls the flow of electrons through a semiconductor. Although those nanofluidic components will never be able to compete with semiconductor ones in terms of fast electronic switching and high current applications, given the lower mobility of ions in liquid compared to electrons or holes in a semiconductor, a number of other applications can be enabled by controlling ionic flows with molecular precision.[15]

Surface charge The extension of the EDL, and the resulting ionic enrichment, responsible for the variation of conductivity inside nanochannels is proportional to the absolute surface charge of the nanochannel-electrolyte interface. Nanofluidic devices have been fabricated for which the conductivity of a nanochannel can be passively controlled through either the modification of the surface charge with surfactants [16] or through changes in the density of SiO^- surface groups through the variation of the pH of the electrolyte around the isoelectric point of the nanochannel material.[17], [18] This approach has found practical applications in EOF pumps where engineered nanopores with tailored surface charge, diameter and length showed flow rates and efficiencies orders of magnitude higher than with other techniques. [19]–[22]

Nanofluidic diodes Further control on ionic flows can be achieved by introducing a controlled asymmetry in the nanochannel. Those asymmetric devices are characterized by a preferential direction of flow across the channel according to the charge and valence of the ions and are defined as nanofluidic diodes. This type of devices are built either by patterning the nanochannel walls with an asymmetric surface charge along the channel axis, positive at one end and negative at the other,[23]–[26] or by introducing geometrical asymmetry with conical nanochannels.[27]–[29]

Nanofluidic transistors Nanofluidic transistors, on the other hand, are nanochannels whose permeability to a charged molecule can be actively modified by modulating their surface charge with an additional third electrode. Like their semiconductor counterpart (field effect transistor (FET)) where the source-drain conductivity is modulated by the electric field of the gate electrode, in a nanofluidic transistor the migration of charged species across the nanochannel is controlled by modulating the extension of the EDL with a third gate electrode.[1] Unlike passive devices like diodes, the capability to modulate the surface charge by means of an external electrode rather than with a coating, a surfactant or by choosing the appropriate material during fabrication, allows to modulate the properties of the nanochannel in real-time, paving the way for new applications. For instance, nanofluidic transistors have shown the ability to modulate both ionic current and flow of charged fluorescent molecules, between two reservoirs at the extremities of a nanochannel. [30], [31]
The concept of active nanofluidic devices has also been applied to fabricate reconfigurable nanofluidic diodes, where the surface potential along the channel axis can be actively modulated. Such tunable nanofluidic diodes were demonstrated with both planar nanochannels[32] and with nanoporous membranes[33].
More complex active devices were also produced for the demonstration of a bipolar transistor with hourglass-shaped nanopores having a P-N-P charge distribution along the channel axis [34], [35] and multiple electrodes along the nanopore axis [36]–[38].

1.3.2 Filtration of solutions and reverse osmosis

From the initial Nafion and track etched membranes, filtration membranes have been adapted for various applications being a cost effective solution compared to other methods like vacuum filtration, centrifugation and spray drying.[18] Filtration membranes are widely used in chemical industries, water purification plants, fuel cells, food processing and biotechnology[39] to specifically remove undesired components from a mixture based on dimension, charge and affinity of the pollutant with the membrane. Filtration membranes are classified by the size of their pores ranging from 1 nm up to some micrometers (figure 1.4).

Reverse osmosis Membrane with the smallest nanopores (0,1 nm to 1 nm) are used for water purification through reverse osmosis, a process that consist of forcing a solution by hydraulic pressure through a semipermeable membrane in the direction opposite to the

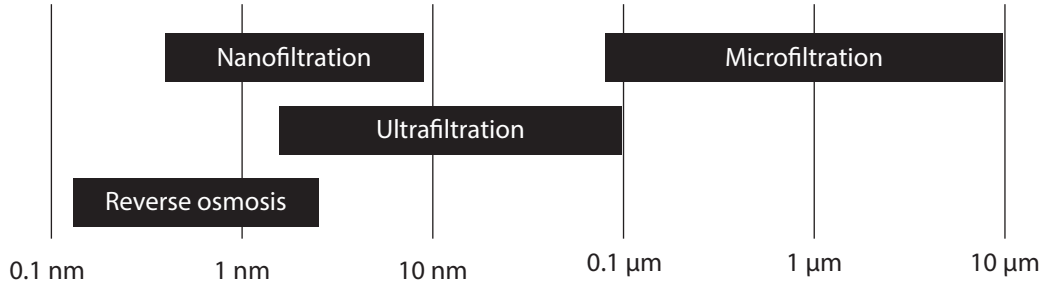

Figure 1.4 – Pore dimension for different filtration membranes. Adapted from [40]

osmotic pressure of the system. The small dimension of the nanopores leaves water molecules flow thorugh the membrane while ionic species such as salt ions and bigger molecules are mostly retained.[41] The process is used for purification and desalination of water, mainly to obtain drinkable water. Since the technology for reverse osmosis is well established, research has focused mostly on preventing fouling of such membranes, thus increasing the production capacity and decreasing the maintenance costs. [42]

Nanofiltration Nanofiltration membranes, having slightly bigger pores within the range of 1 nm to 10 nm, have a low rejection rate of monovalent ions and high rejection rate of divalent ions but allow a higher flow compared to reverse osmosis membranes. Typically, molecules bigger than 300 Da to 500 Da are retained. [43]

Ultrafiltration Membranes with nanopores in the range of 1 nm to 100 nm, and repelling molecules with molecular weights typically of 300 Da to 300 000 Da are defined as ultra filtration membranes. They differentiate from reverse osmosis and nanofiltration membranes because the osmotic effects are small and the pressure to drive the liquid must mainly overcome the viscous resistance of the liquid through the membrane. Those membranes are mainly used in biotechnology since ions, solvent and small molecules pass through while bigger molecules such as proteins and enzymes are retained. [18], [44], [45]

Microfiltration Microfiltration membranes exhibits pores with dimensions greater than 100 nm which are mainly used to extract suspended bacteria, large colloids, or particulates, from solutions. [46]

1.3.3 Preconcentration

When a flow of species of charge opposed to the surface charge preferentially diffuses through a nanochannel such in the case of membranes for reverse osmosis and nanofiltration, charged species accumultates on one side of the nanochannel and depletes on the other side. The accumulation and depletion does not regard only the species that crossed the nanochannel

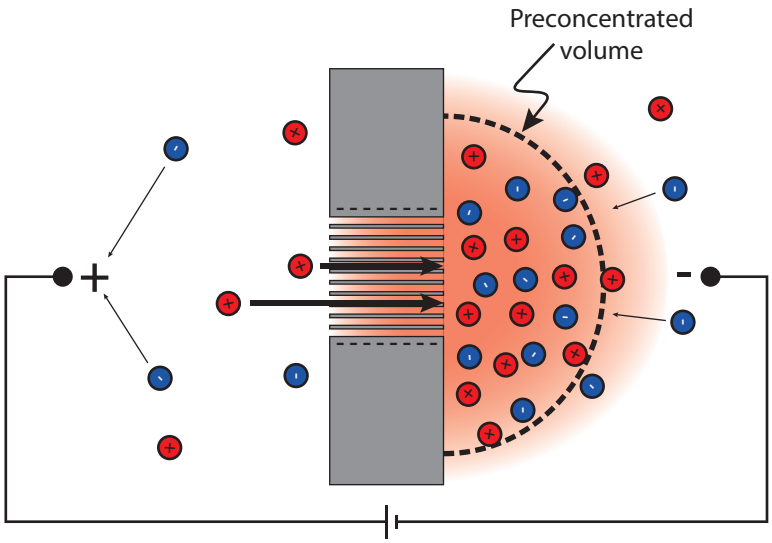

Figure 1.5 – Principle of ICP. The permselectivity of a nanoporous membrane results in the concentration of both counter- and co-ions in proximity of the membrane. Adapted from [47]

but, because of electroneutrality, is immediately compensated by a flow of ions of the opposite charge (figure 1.5). Such electrokinetic phenomenon resulting from the permselectivity of a nanochannel is called ion concentration polarization (ICP).[47]

Devices that exploits this phenomena to locally concentrate molecules for further detection are of high efficiency since they allow concentration independently from the hydrophobicity and binding characteristics of the molecules of interest, are controllable via an external electric field and don't suffer from clogging.[48] Proper engineering of preconcentration systems in terms of nanopore dimension, membrane porosity and surface properties will increase the sensitivity of detection systems significantly.[49] Nanofluidic devices have shown up to million-folds preconcentration of peptides and proteins.[50] Critical parameters for the engineering of such systems are the nanopore dimensions and the material which dictates the surface charge and the nanopore affinity with the molecules of interest.

1.3.4 Nanomedicine

One of the most exciting fields of research that is affected by advancements in nanofluidics is the manipulation and measurement of molecules and chemical processes, especially in biological systems.[51]

Nanopore sensing Those unique abilities of nanofluids have been exploited mostly for sensing the translocation of molecules through a nanopore and great effort has been devoted to probe the composition and properties of deoxyribonucleic acid (DNA) molecules.[52], [53] Among the different kinds of sensing with a nanopore that have been developed in the years,

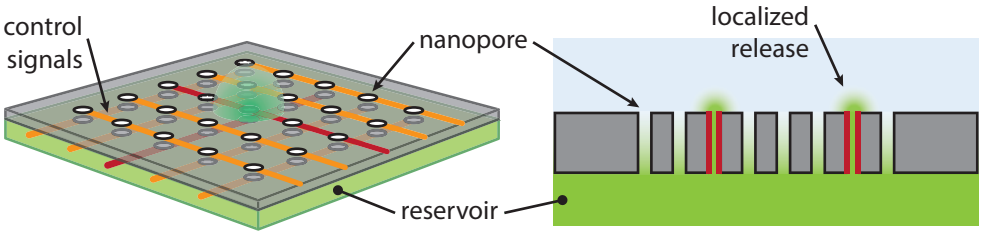

Figure 1.6 – Graphical representation of nanoporous membrane for the release of chemicals with nanopores individually addressable. The drawing highlights the potential to integrate and parallelize a multitude of independent devices to modulate the concentration of chemicals only in specific areas.

most of them are based on the same concept of the Coulter counter.[54] This consist in deducing shape and dimension of a molecule based on the modification of the electrical conductivity when a molecule is translocating through the nanopore. By analysing the shape of the resistive pulses in relation to the pore geometry its possible to deduce the relative volume occupied by the particle and therefore extract informations on its geometry.[55]
Specifically engineered solid-state nanopores were used to individually detect a wide range of proteins (14 kDa to 465 kDa), DNA, and DNA-bound proteins by blockade current. [56], [57] Particularly, engineering with precision the geometry of the nanopore and its surface interactions with the analyte allows to gain new insights on the shape of complex molecules and their folding/unfolding by affecting their residence time in the nanochannel, or by allowing rotations and reconfigurations inside the nanochannel, all informations deducible from the shape of the output resistive pulses.[58], [59] Such passive systems are however limited by the too rapid translocation time of the molecule of interest inside a nanopore, and suffer from a limited temporal resolution.[57], [60], [61]
Efforts have been made to slow down the translocation time, and increase the temporal resolution of the sensors. The application of a Al_2O_3 coating modified the surface charge of a polyethylene terephthalate (PET) nanopore and increased the interaction between a bovine serum albumin (BSA) protein and the wall of the nanopore, therefore reducing the translocation speed of proteins. [62] The same nanofluidic effect was exploited to slow down a DNA molecule in a nanopore, by actively modulating the surface charge with a nanofluidic transistor rather than with a passive coating.[63] Similarly, a nanofluidic transistor has been used as a sensor to detect the translocation of DNA and antibodies by using the gate voltage to reduce the translocation speed of molecules through the nanopore and dynamically modify the dimension of the nanopore, and therefore its selectivity.[64]

Drug delivery systems The nanotechnological revolution has led to massive efforts in developing new drug delivery methods based on nanoparticles or nanovescicles to specifically target drugs to the cells of interest[65]–[68] but devices based on active nanofluidic properties didn't emerged as products even if they are potentially able to perform fast, precise, high resolution and on-demand delivery of drugs (figure 1.6).

This is probably due to the complex technology required to fabricate nanochannels able to control flows at the nanoscale. A feasibility study demonstrated how a membrane made of an array of addressable nanopores may be able to selectively control the release of neurotransmitters that chemically stimulates neurons only in close contact with the targeted nanopores and therefore would function as an artificial synapse.[69] Alternative applications of those kind of membranes may be used to actively control the release of a cocktail of drugs in the appropriate concentration and only when needed. The closest example to a nanofluidic drug delivery system, was a passive nanoporous membrane for controlled release of BSA which nanosieve dimension was tailored to obtain a controlled flow rate of $15\,\mu g\,d^{-1}$. When implanted *in-vivo*, the device showed an extended duration of BSA release from 10 to 45 weeks compared to subcutaneous injections, demonstrating this way the potential of nanofluidic devices in nanomedicine applications.

1.4 Motivation and project statement

Technological advances to fabricate and pattern nanochannels with dimensions down to some nanometers have enabled the development of active nanofluidic devices of which the nanofluidic transistor is the biggest proponent. Applications of active nanofluidics are slowly diffusing to other fields of application such as electroosmotic pumps, nanomedicine, biological sensing, preconcentration devices but the introduction of those technologies is still hindered by the lack of methods to rapidly fabricate nanofluidic channels with enough freedom in channel geometry and materials.[2], [70]–[72]

To fill this gap, the first part of this work proposes and characterizes an innovative fabrication method for manufacturing nanoporous membranes, which allows greater freedom in terms of engineering pore geometry and materials, the two parameters that mostly concerns the potential of nanoporous membranes.
In the second part, after a functional introduction on the basics of theoretical nanofluidics, this method is used to fabricate a electrostatically gated nanoporous membrane which gating is done with a polarizable electrode made of amorphous carbon.

2 Fabrication of solid-state nanoporous membranes through sacrificial silicon templates

In this chapter is presented an innovative fabrication method for solid state nanoporous membranes based on the use of sacrificial silicon templates to define the placement and geometry of nanopores with nanometric precision. First the Si templates are fabricated and characterized. Then the importance of the deposition method for the membrane, whether directional or conformal, is discussed in detail and the resulting structures are presented as well as their relevance for specific applications. This chapter is mostly based on two publications from 2015 and 2017. [38], [73]

Technological advances in the field of micro and nano-fabrication recently demonstrated unique applications based on peculiar properties of nanofluidics. The ability to modulate relevant parameters of nanochannels such as critical dimensions or the span of the electrical double layer, extended the use of nanoporous membranes from passive applications as water-desalination to active ones as nanofluidic diodes or transistors.[23], [26], [30], [33] Nanofluidic devices actively controlling the behaviour of liquids at the molecular level could lead to breakthroughs in nano-medicine, filtration, energy production or bio-chemical analysis[18], [51], [70], [74].
Although nanofluidics is relevant to many fields of research, its development has been hindered by the lack of reliable and flexible manufacturing techniques enabling engineering of key parameters such as nanopore geometry, surface charge, and materials [70]–[72], [75].

State of the Art of nanoporous membranes fabrication Different methods have been developed to fabricate solid-state nanoporous membranes.
The most widespread and commercially successful are track-etched membranes whose pores

are defined through heavy atom bombardment of polymeric films.[76] A new approach to synthesize polymeric membranes through self-assembly of block-copolymers has recently been emerging.[77] Those approaches allow the synthesis of large surface membranes with control over porosity and pore dimension, however they fall short when non-polymeric materials or more strict pore positioning are desired.[78] To extend the choice of materials beside polymers, the intrinsic properties of aluminium anodization were exploited to define a self-assembled hard-mask for the material of interest.[26], [33] Although these methods allow quick fabrication of membranes with controlled porosity and pore size they rely on stochastic methods and are thus inappropriate when a more rigorous control over single-pore geometry and positioning is required.
Methods that independently define the shape and placement of the pore were developed using focused ion beam (FIB) or electron beam lithography (EBL). FIB based methods, which independently sculpt every single nanopore of the membrane[79], [80], are used for the fine control they offer over nanopore geometry but, due to their serial nature, are time consuming and inappropriate to fabricate large numbers of nanopores. EBL followed by deep reactive ion etching (DRIE) is faster and more time-efficient than FIB, but the geometries one can obtain are limited by the use of DRIE on the membrane material.[36] In order to increase the range of materials and properties at the nanopore-liquid interface, an effort was made to coat nanopores with different materials using techniques ranging from atomic layer deposition (ALD)[37], [81] to organic coatings.[23] This effectively changes the surface charge of nanopores or electrically insulates the underlying electrodes. Other techniques rely on the control of intrinsic properties of materials such as Nafion[82] or on the controlled creation of defects to define nanopores[83]. Finally, techniques based on sacrificial structures to define the shape of the nanopores were developed using track-etched membranes[84] or SiO_2 layers [85]–[87] as a template. Those approaches can be more laborious than the ones previously cited but are more general and often offer greater flexibility in terms of design and choice of material. However, even by using sacrificial templates made of SiO_2 to define the placement and positioning of nanopores, the fabrication method still strongly influences the capability to engineer the membrane, since the use of hydrofluoric acid to remove SiO_2 templates[86], [87] limits the use of metals in the process. A manufacturing method allowing to simultaneously define material, position and shape of nanopores in reasonable times is still missing.

2.1 Concept

The concept proposed here is an innovative and wafer-scale method to fabricate solid-state nanoporous membranes in a wide range of materials and geometries based on sacrificial silicon templates.
The presented method defines the geometry of each nanopore by means of a silicon sacrifical nanostructure which is subsequently used as negative cast for the nanopores. It can be summarized in three parts: first, the sacrificial templates are created through EBL followed by DRIE; second the membrane material is deposited on and around the template; finally the

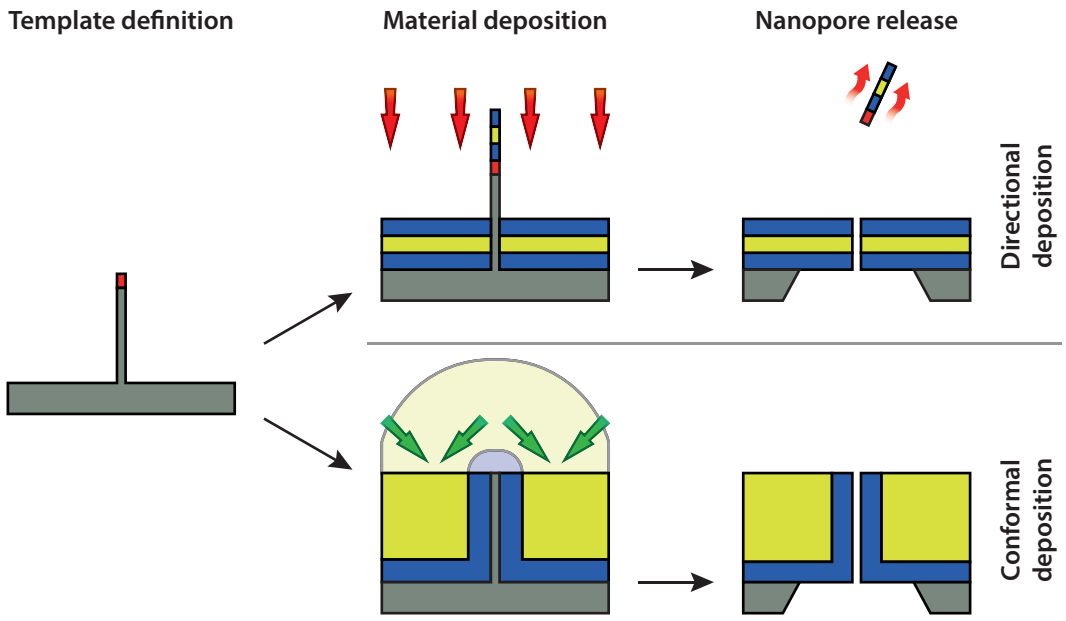

Figure 2.1 – Concept of the fabrication of nanoporous membranes through silicon templates. Starting from a sacrificial silicon template (**left**) its possible to obtain either multilayered membranes, either high aspect ratio nanopores by choosing the appropriate deposition method.

selective removal of the templates with XeF_2, a gas known to etch Silicon with high selectivity, reveals the pore whose shape result to be the exact negative of the silicon template, and releases the free-standing membrane (figure 2.1).

Comparison to other fabrication methods The advantage of the strategy presented here is that the geometry and material of the nanopores can be freely chosen accordingly to the application.

First, the use of a combination of EBL and DRIE to define the shape of silicon structures allows to control the placement and geometry of every single pore by design, independently from other nanopores and from the material used for the membrane. In principle free-shaped, non-round, conic or high aspect-ratio nanopores can be manufactured in the same chip. Furthermore, since the micromachining of silicon nanostructures is a reliable, well controlled and uniform process at the wafer scale[88], membranes with different designs can be fabricated in parallel on the same wafer, thus introducing the possibility to obtain a multitude of distinct samples in a time-effective way compared to serial fabrication processes such as FIB milling.

Secondary, XeF_2 has the advantage to be extremely selective to silicon[89]–[91], thus enabling the use of virtually any material that is not attacked by XeF_2 gas, therefore removing the silicon

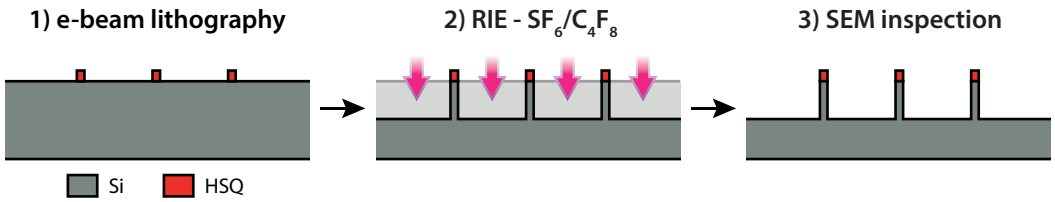

Figure 2.2 – Process-flow for the fabrication of Si templates. Initially a electron beam lithography (EBL) defines the shapes of the pillars (**left**). The templates are then carved in the bulk silicon (**center**) through anisotropic reactive ion etching (RIE). The resulting structures are shown at the **right**.

sacrificial structures but leaving intact anything else included the deposited materials and thus the nanopores. The list of materials that withstand XeF_2 is large, and it comprehend most of metals, ceramic, polymers and organic materials independently from the the way they were deposited. The only materials substantially attacked by XeF_2 reported by Williams[90], [91] are silicon, silicon nitride (stoechiometric and not), titanium and tungsten, leaving out a wide choice of options to be used for the membrane. Beyond the good selectivity, XeF_2 etching is a process in gas phase particularly appropriate to create suspended membranes since it further prevents any issues typically related to DRIE processes such as temperature gradients, physical ion bombardment and backside pressure.

In the rest of the chapter the fabrication of the silicon sacrificial templates is first described and characterized, then the influence on the used deposition method, whether directional through evaporation or conformal through sputtering or chemical vapor deposition (CVD), is presented.

2.2 Sacrificial silicon nanostructures

Vertical silicon nanowire (SiNW) show promising applications in biochemical sensors, solar cells, and microfluidics among many others. They are mostly obtained via bottom-up approaches, thus relying on intrinsic properties of matter at the nanoscale.[92], [93] Although those approaches are convenient in terms of quantity of Si nanostructures obtained and simplicity of the process, they fall short when a more strict control over dimensions, positioning and geometry of the structures is required.
In this section is presented and characterized a top-down method for the fabrication of SiNW and nanoFins on crystalline silicon wafers with critical dimensions under 30 nm and high aspect ratio. The process relies on EBL to individually define the shape and placement of the nanostructures, followed by DRIE to carve the structures in the bulk silicon (figure 2.2).

2.2.1 Method

Wafer preparation 200 nm of Si_3N_4 were grown by plasma enhanced chemical vapor deposition (PECVD) on a double side polished silicon wafer < 100 > of 100 mm in diameter. The Si_3N_4 frontside was then thinned until about 60 nm remained using He/CHF_3 based DRIE, and then dipped in HF 49% for 4 min to remove the nitride left frontside, thus leaving a smooth and clean silicon surface for EBL. This way the backside layer is partially thinned too, but 120 nm of Si_3N_4 are left which is enough to be used as hard mask for a KOH etch step later in the process.

Silicon structures fabrication The nanopore geometries were defined with a frontside EBL. The wafer surface was first activated through 600 W O_2 plasma for 2 min to enhance e-beam resist adhesion. The wafer was then spin-coated frontside with about 140 nm of hydrogen silsesquioxane (HSQ) 6%, a negative tone e-beam resist, at 3000 rpm(Dow Corning, XR-1541-006). E-beam patterns were then written at a dose of 8500 $\mu C\,cm^{-2}$ then developed in TMAH 25% for 2 min[1]. The combination of high dose and long development time in TMAH was found to enhance both the contrast and tolerance to imprecise development time, resulting in a better reproducibility of the lithography accordingly with previously reported results.[94] Once developed the HSQ patterns were then further cross-linked through O_2 plasma, (600 W for 2 min), in order to increase the selectivity to the following etching step. The e-beam lithography step, due to the small surface of the membranes, takes only 90 s for the entire wafer. The sacrificial structures were finally obtained through transfer of the HSQ patterns into the wafer Si bulk through a room temperature continuous anisotropic DRIE using SF_6 as etchant and C_4F_8 as passivator. The etching is based on a published process[95] and was further optimized for our specific design (28 sccm of SF_6 and 55 sccm of C_4F_8, coils frequencies of 13,56 MHz, and coil power of 1500 W and platen power of 15 W on an Alcatel AMS200 SE).

2.2.2 Results

Using the process previously presented, arrays of silicon nanostructures were defined through EBL and carved in the bulk of a silicon wafer using a continuous DRIE process based on SF_6 and C_4F_8. The nanostructures were fabricated with three different geometries (round, linear and wavy), three different etching times (4 min, 6 min and 8 min) and with a pitch of 1 µm or 3 µm. An array has a total surface of 20 × 20µm.

Columnar structures Round HSQ masks with diameters ranging from 10 nm to 70 nm were used to fabricate uniform arrays of columnar templates. Arrays of structures 930 nm to 2400 nm tall and with different diameters were obtained.

[1] Please note, if you ever try to replicate this process be really careful when handling concentrated TMAH. It is highly neurotoxic and skin contact is enough for poisoning.

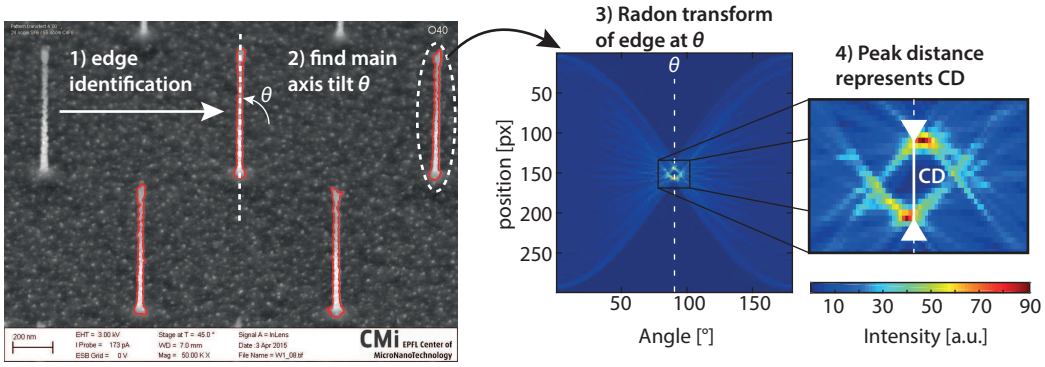

Figure 2.3 – Image processing and analysis of Si templates. First the edges of the Si structures are identified (**left**), then the Radon transform is calculated on the structures contour to identify the main lines in function of the angle (**center**). Finally the width of the structure is extracted as the distance between the two highest peaks of the Radon transform (**right**).

To quantify the resulting dimensions an image analysis of scanning electron microscopy (SEM) micrographs (with magnification x50k) was done on a pool of 35 randomly chosen structures belonging to the same array for structures of every different mask diameters. As visible in figure 2.4, the roughness of the structures is not negligible compared to their width; and even by smoothing the oulined-shape, the walls are neither perfectly parallel, nor perfectly straight. A robust image processing protocol is therefore necessary since a manual measurement would be strongly user dependent.
To analyse the shape of silicon templates, first they were identified on the SEM micrograph and their contour outlined through thresholding of the two-dimensional gradient of the grey-scale image (i.e. identifying the edges, shown in red in image 2.3). Second the tilt θ of the best-fitting ellipse on the extracted region was used as representative of the inclination of the template on the micrograph. Finally, the two main peaks of the radon transform at the angle θ represents the dimension of the structure (figure 2.3).[96]

For an etch process of 4 min, round silicon structures (nanopillars) with diameters down to 40 nm and 1220 nm tall were fabricated with HSQ masks of 50 nm in diameter. Structures 1690 nm tall (6 min etch) showed an increase in the minimal diameter that could be successfully fabricated to 49 nm, and structures 2260 nm tall (8 min etch) were obtained with minimal diameters of 70 nm (figure 2.4).

The maximal aspect-ratio for columnar structures was about 30-34 regardless of the height (figure 2.4). Columnar structures with smaller diameters or higher aspect-ratio collapse during the processing. A reduction of diameter of about 3 nm to 5 nm due to lateral under-etch is consistently observed and becomes more pronounced for lower diameters, probably due to a local load effect, altering the ratio SF_6/C_4F_8. Using this result as a design rule, nanopillars with diameter as small as 30 nm and 1 µm tall could be obtained (figure 2.5).
Etching times higher than 8 min were not investigated since all the 130 nm of HSQ used as a mask are consumed at this point, resulting in a selectivity of the etch process of about 17,

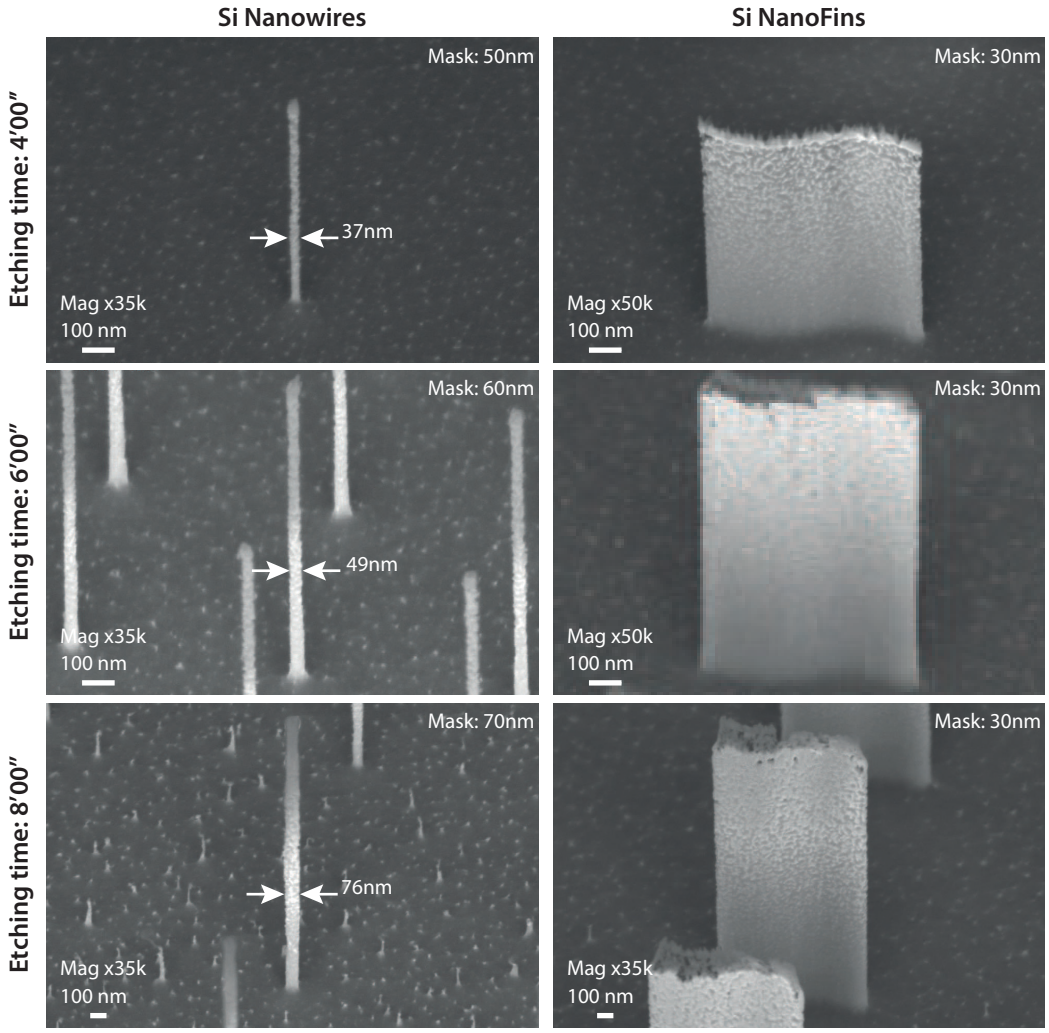

Figure 2.4 – Minimal critical dimension achievable vs. the template height and geometry.

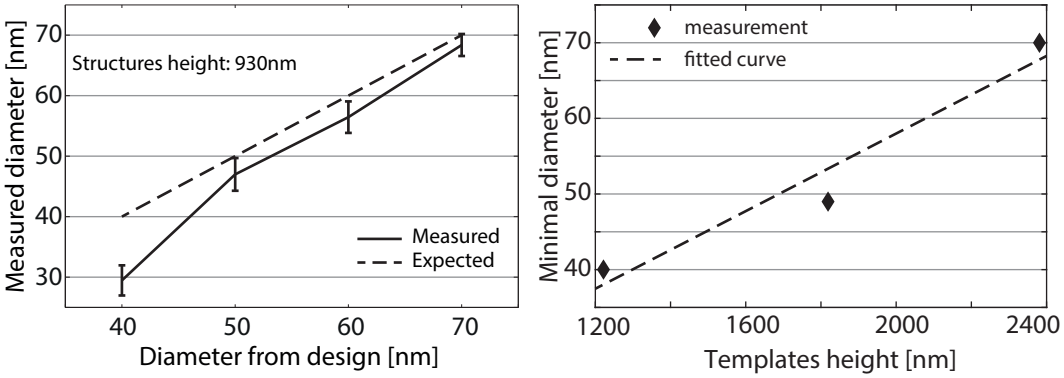

Figure 2.5 – Characterization of cylindrical Si nanotemplates. **Left:** Measured diameter vs. the diameter in the design. **Right:** Relationship between the minimal diameter achieved according to the nanotemplate height.

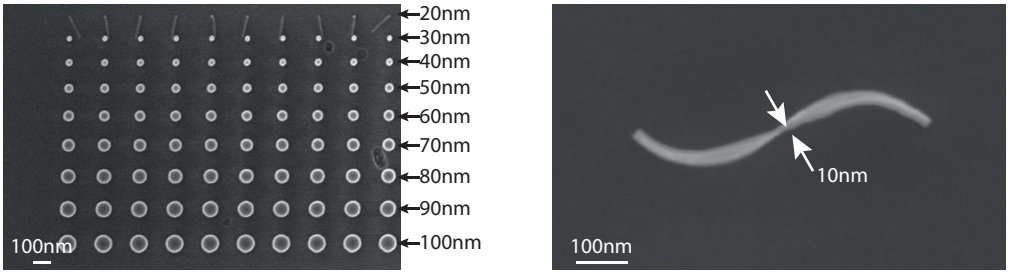

Figure 2.6 – Hydrogen silsesquioxane (HSQ) structure stability after development in TMAH. Round nanopillars show to be stable down to 30 nm (**left**), while wavy nanofins present increased stability down to 10 nm in critical dimension (**right**). The wider dimension where the structure bends is a perspective effect due to the flexibility of the structure. All structures are 130 nm tall.

Silicon to HSQ.

The main bottleneck we observe in obtaining smaller diameter pillars consist in the aspect ratio (AR) of the HSQ mask. For a HSQ thickness of 140 nm the smallest standing structure were pillars of 30 nm in diameter. Structures with smaller footprint collapsed during the drying after development because of surface tension. Collapsed 20 nm HSQ structures are visible in figure 2.6 - left.

Linear structures Because of their shape linear structures are expected to have a higher stability than round structures, and thus to collapse less easily while drying. Nano-fins were thus obtained with 1 µm long linear masks and widths ranging from 10 nm to 70 nm. With such geometry the critical dimension (CD) of the thinnest structure could be reduced to 20 nm compared to 40 nm for columnar structures (930 nm tall components), thus showing the greater stability of linear geometries with respect to round ones.

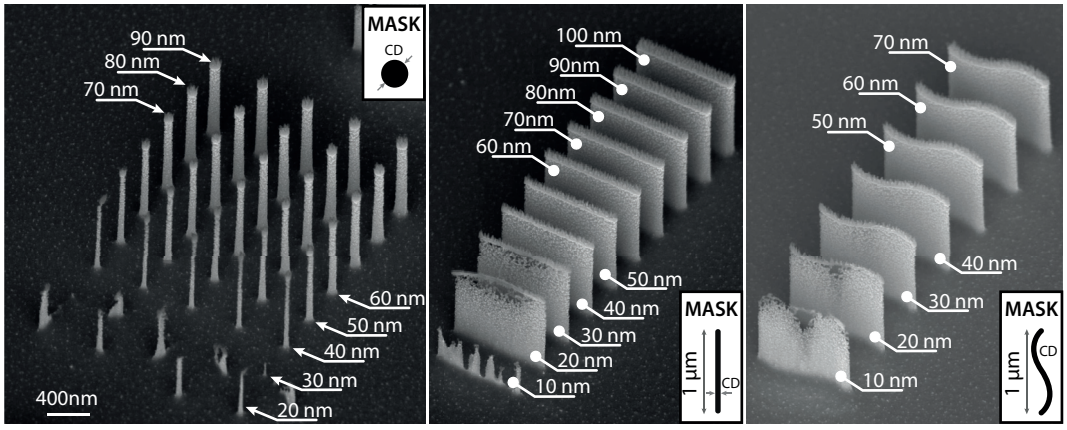

Figure 2.7 – Influence of shape on stability of templates. Wavy nanofins (**right**) showed greater stability than linear (**center**) or cylindrical (**left**) structures, resulting in smaller critical dimensions and higher aspect-ratios.

Wavy structures To further increase the stability of the template structures, the mask design was modified into a wavy line. With such a wavy design we couldn't observe any collapse of the HSQ mask while drying as visible in figure 2.6 - right, even at critical dimension (CD)=10 nm, which is a significant improvement compared to previous designs.
The sacrificial structures are now limited by the lateral under-etch, which starts to appear in the middle of structures with CD ≤ 20 nm.

It is important to notice that, since the etching process was optimized for columnar structures, an angle of about 1° could be observed in the FIB cross-sections for linear structures, likely because a local load effect slightly alters the SF_6/C_4F_8 ratio around the structures. This may seem negligible at first sight but in the case of linear and wavy structures it results in a base consistently 20 nm wider than the tip (i.e. mask design), regardless of the size of the mask.

Etch uniformity Characterization of the etching depth as a function of the distance from the center of the wafer was carried out on four different wafers. Results shows a divergence of ±5% along the radius, with a variability of less than 2% between the four different wafers.

2.2.3 Discussion

Considerations on HSQ mask stability The minimal size of the structure is indeed limited by the HSQ aspect ratio (maximal AR of ≈ 10) and the intrinsic stability of the template. The size of the templates could therefore be reduced if a thinner layer of HSQ is used, allowing to

obtain more stable masks at small sizes. A thinner mask would reduce the maximal height of the template, limited by the selectivity to HSQ of the etching process (about 10:1). This HSQ thickness of 130 nm was chosen as a trade-off between stability of the structures, structure size and structure height.

Influence of etching The DRIE process used to carve the silicon nanostructures can be tuned to control the shape of the nanopores. The quantity of passivator (C_4F_8) and etchant (SF_6) gasses used during the etching step determines the verticality of the walls of the template. An excess of SF_6 results in structures with a tip wider than the base (under-etch) whereas a greater quantity of passivator returns structures where the base is wider than the tip because of the accumulation of C_4F_8 on the wafer. Furthermore, the density of the patterns influences the optimal ratio of SF_6/C_4F_8 similar to a "load effect": the denser the pattern, the higher the area to passivate, the higher the flow of C_4F_8 needed for optimal results. Indeed, for structures with the same critical dimension, pattern densities higher than the the one for which the etching was optimized, gives suboptimal results since the pillars are not stable, and the underetch start to be dominant, especially toward the tips of the templates as shown in figure 2.8.
Supplementary tests reinforced this hypothesis by showing a dependence of the angle of the templates from the template density. Although the variation in the verticality of the templates is low in absolute ($\approx \pm 1°$) it has a strong impact on the final shape of the structure, because it significantly increases the footprint of the structure. Since the final shape of the nanopore is directly related to the shape of the template this aspect has to be considered in the design phase.
Two guidelines can be given based on these considerations: first, the mentioned "load effect" creates a trade-off between uniformity of the structures and local variation of template density. Second, by tailoring the SF_6/C_4F_8 ratio conical sacrificial structures (and therefore conical pores) can be easily obtained. In our case the etching process was optimized for columnar structures of 50 nm. The same etching recipe is thus suboptimal for structures with slightly greater surface such as nanofins, which therefore resulted with a base slightly wider than the tip.

2.3 Directional deposition

The adoption of evaporation as deposition method for the membrane provides a wide choice of materials, ranging from dielectric to conductive materials, with different surface properties, uniformity of films, range of deposition (typically 1 nm to 1000 nm), and gives the unique possibility to obtain vertically stacked multi-layers. This way functional membranes with asymmetrically or heterogeneously charged nanopores can be obtained. This can be particularly useful to integrate multiple electrodes along the nanopore.[36]
As proof-of-concept we fabricated multilayered nanoporous membranes made of a layer of Pt enclosed between two layers of SiO_2, embedding arrays of nanopores with conical section and having different geometries.

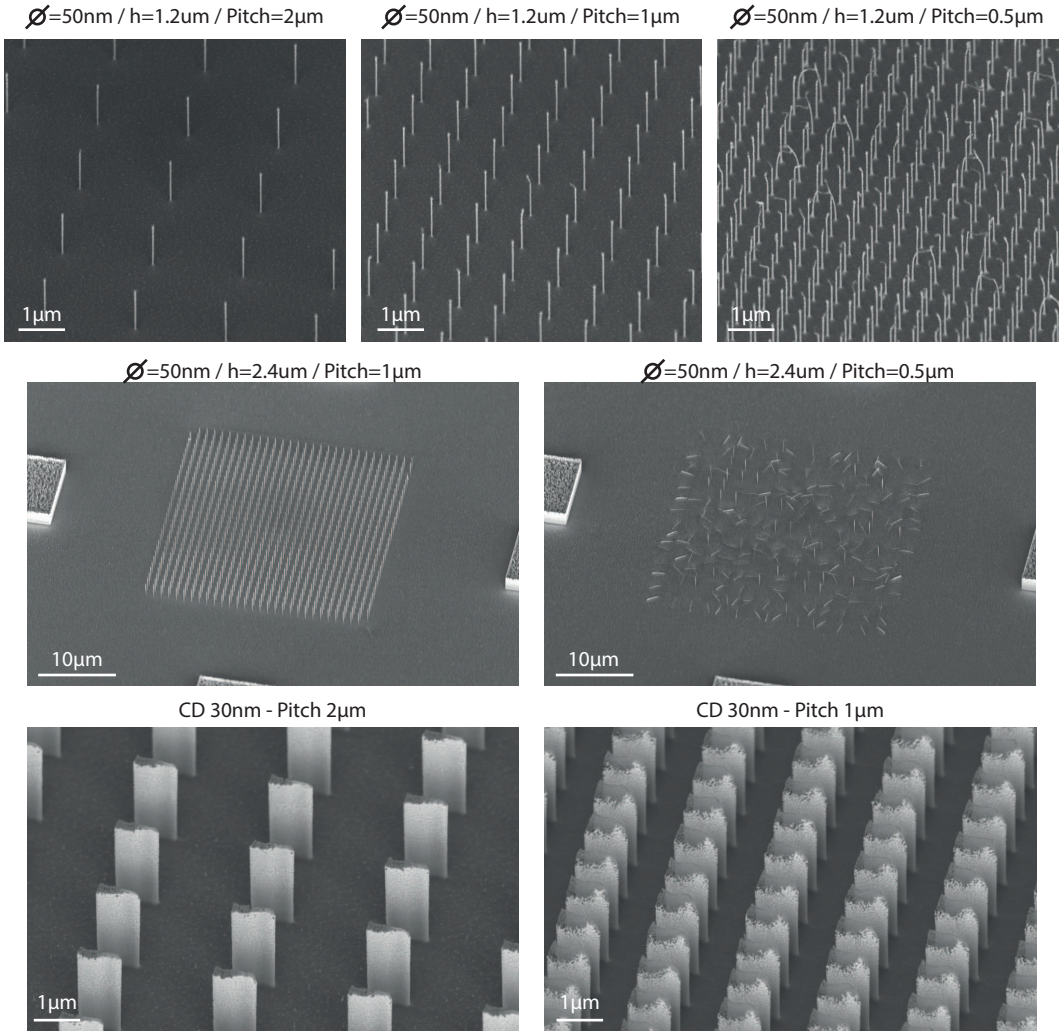

Figure 2.8 – Influence of pattern density on the fabrication of Sitemplates.

2.3.1 Method

Evaporated membranes On top of the silicon sacrificial templates described previously the following materials were deposited by evaporation in this order: 50 nm SiO_2 + 5 nm Ti + 300 nm Pt + 5 nm Ti + 50 nm SiO_2 (figure 2.9.2). The layer of 5 nm of Ti was evaporated to enhance the adhesion of the SiO_2 and Pt layers. On top of that 750 nm of silicon was sputtered to temporary protect the sacrificial silicon structures during the successive backside lithography (figure 2.9.3). This temporary protection layer will then be removed simultaneously with the sacrificial templates in the last step of the fabrication. Platinum and SiO_2 were chosen as they are materials widely used as electrodes or insulators respectively, thus showing the potential to integrate different electrodes along the membrane.

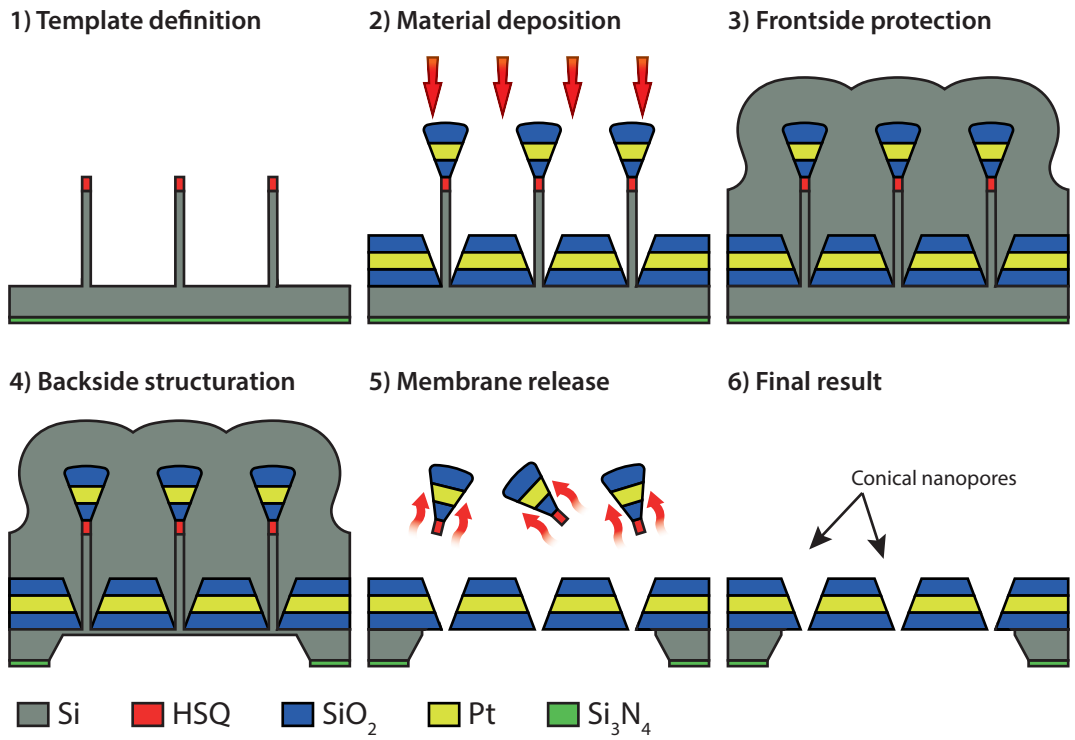

Figure 2.9 – Graphical representation of the major steps of the fabrication of multilayered nanoporous membranes through directional evaporation on sacrifical silicon templates. First, the templates are fabricated with the desired nanopores geometry **1)**, then the multilayers composing the membrane are evaporated on top of the sacrifical templates through evaporation **2)** and protected with a sputtered layer of Si **3)**. The backside of the wafer is then structured **4)** and the nanopores are finally released through XeF_2 etch **5)**. The resulting membranes are made of the evaporated films and integrate conical nanopores **6)**.

Membrane release To release the membranes a combination of KOH and XeF_2 etching was used (figure 2.9.4). First the Si_3N_4 layer backside was structured as hard mask using standard photolithography technology (2 µm of AZ9260) followed by He/CHF_3 based DRIE to expose the silicon underneath. Then the wafer was etched backside with KOH (40% at 60 °C for approximately 19 hours) using a waterproof teflon chuck to protect the frontside until 5 µm to 10 µm of silicon were left. The wafer was then cleaved into chips with the help of a diamond pen. To finally release the freestanding membranes, the last micrometers of silicon on backside, the silicon protection layer, and the sacrificial structures were removed through XeF_2 pulsed etching in groups of 4 chips (50 × 30 seconds at 2700 mbar).

2.3.2 Results

Directional deposition of thin-films through evaporation holds the promise to fabricate nanochannels made of heterogeneous materials along the pore axis using the sacrificial structures previously shown as template.
Figure 2.10 shows the cross-section of the Pt and SiO_2 layers deposited on a linear template

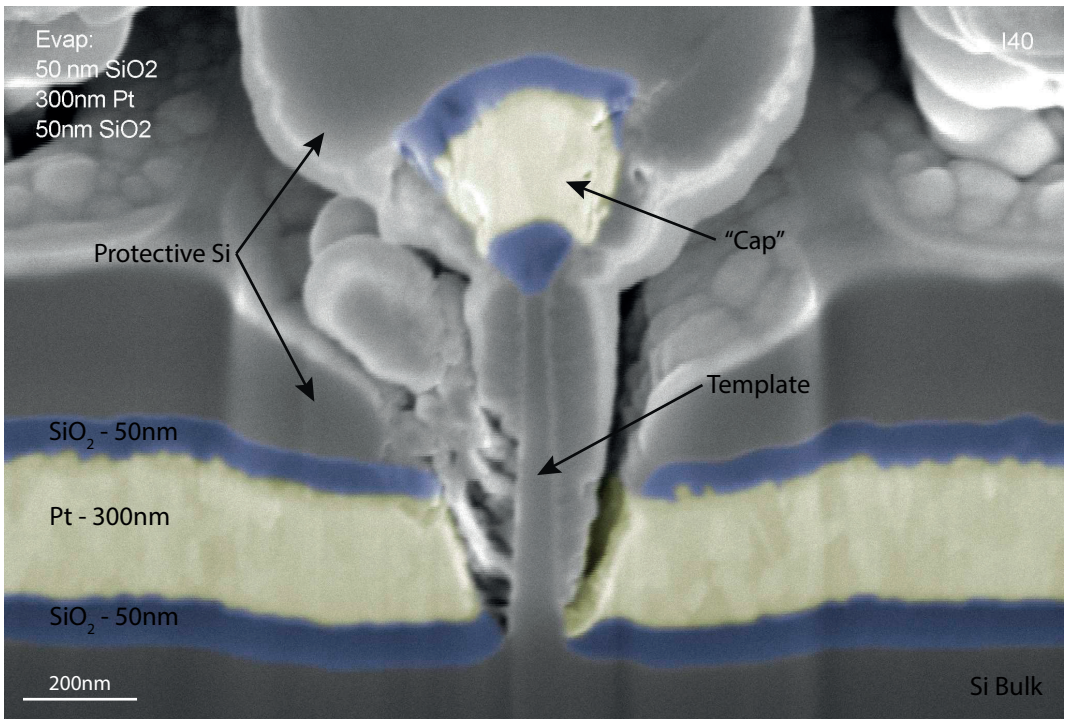

Figure 2.10 – Colored tilted SEM micrograph of the FIB cross-section of a linear template before XeF_2 release. The evaporated layers of SiO_2 and Pt are highlighted. The template is visible in the middle as long as the three layers of SiO2–Pt–SiO2. The "cap" that creates the conical shape of the pore is visible on top of the template. Note, the image is taken at 45°, so the structure is in fact taller than it appears.

structure 930 nm tall and with a CD of the HSQ mask of 20 nm. The Pt layer and the the two SiO_2 layers enclosing it are artificially coloured and are well distinguishable on the picture. After XeF_2 release the silicon template and the silicon protection layer visible in figure 2.10 are etched away and only the evaporated material is left, the result is a suspended membrane with porosity and pore geometry controlled both front- and backside as shown in figure 2.11. Some defects (less than 1%) were observed due to the bending of sacrificial columnar templates at CD close to the limit of stability of the structures. Those defects are only present in the membranes obtained with pillars and not in the ones from the linear and wavy templates given their higher stability.
In order to show the capability to stack multiple layers in the same nanopore, up to 7 layers of alternated SiO_2 and Pt, each 60 nm thick, (with 5 nm of Ti in between layers to promote adherence) have been evaporated as presented in figure 2.12.

Pore dimension To evaluate the final dimensions of the pores, image analysis was performed on 119 pores of the membrane based on columnar templates with diameter of 40 nm (shown in figure 2.11). The result shows a CD= 64 nm ± 17 nm. The final size analysis was performed on columnar structures with 40 nm of diameter since the etching process was specifically

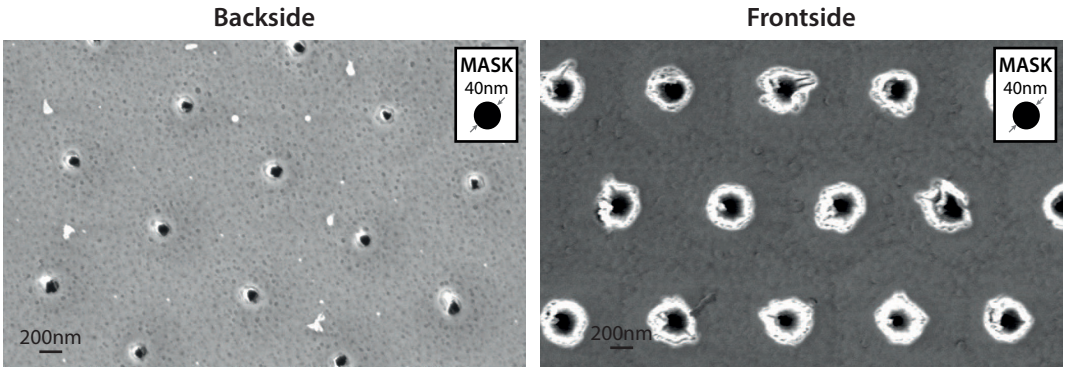

Figure 2.11 – SEM micrograph of the backside (**left**) and frontside (**right**) of an evaporated nanoporous membrane after XeF_2 release.

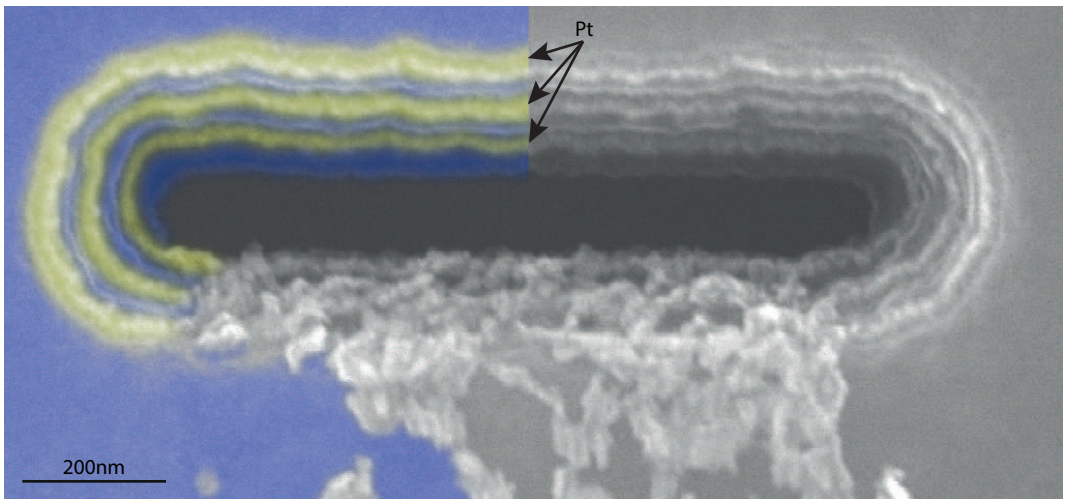

Figure 2.12 – Colored SEM micrograph of a multilayered nanopore with a stack of four alternated SiO_2 (in blue) and three Pt (in yellow) layers.

optimized to this structure.
Membranes with linear and wavy templates resulted in pores wider than expected from design due to the wider base of the template previously mentioned and further discussed later in the document.

Impact of evaporation A fundamental aspect resulting from the choice of evaporation as deposition method is the lateral growth of the film during deposition. This results in a distinctive "cap" on top of the sacrificial structure (visible in figure 2.10) which laterally grows proportionally to the thickness, thus shadowing the deposition at the base of the structure. The outcome is a conical nanopore, as visible on figure 2.10, which angle depends on the deposition conditions and is thus specific to the material. In our case we measured this angle to be $28° \pm 2°$ (Note that figure 2.10 is tilted 45° and the angle is more acute than appears on the figure).

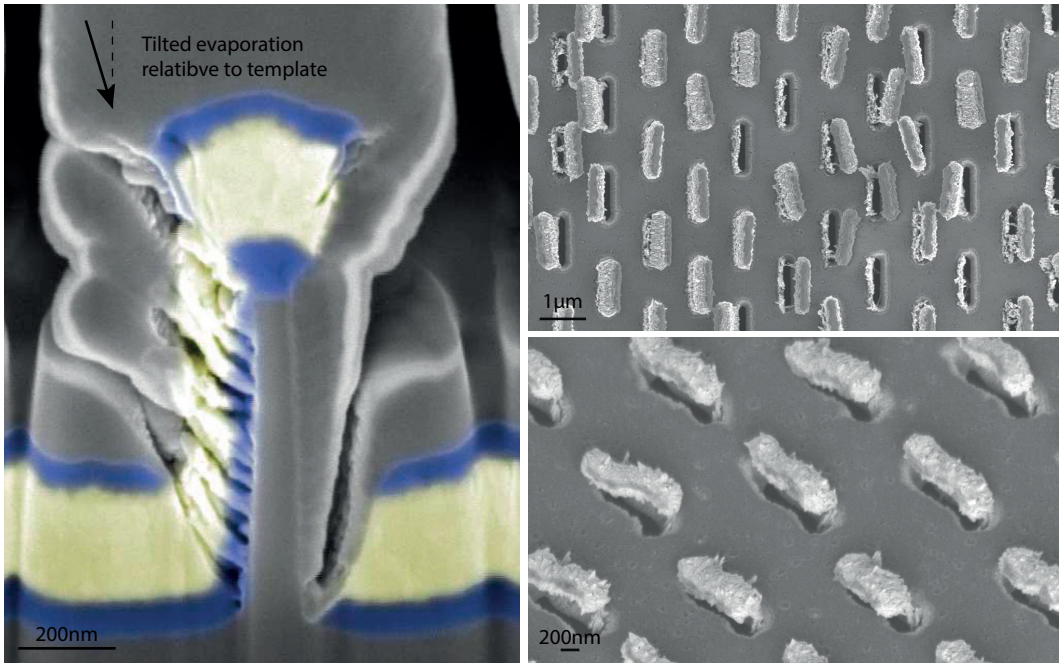

Figure 2.13 – Colored SEM micrograph showing the effect of tilted evaporation. **Left:** FIB cross-section where its possible to observe that the three layers are deposited on the side of the template, thus connecting the "cap" with the base. **Right:** Results after template release on linear (**top**) and wavy (**bottom**) sacrificial structures.

One other important aspect to consider is the directionality of evaporation which should be as perpendicular as possible to the wafer surface. A tilted evaporation results in a deposit of material on the flank of the structure as can be seen in figure 2.13, on the left side of the template. A more pronounced tilt would deposit enough material to connect the "cap" with the membrane underneath such that during XeF_2 release it would not fall as expected but rather stay attached to the membrane, as happened in the case presented in figure 2.13 - right. Such side deposit do not appear to have consequences on the nanofluidic behaviour of the membrane as long as it does not affect the critical dimensions of the pores.

2.3.3 Electrical characterization

In addition to SEM inspection two different tests were conducted to assess proper definition of the membrane geometry and their integrity. First the porosity deduced through electrical conductance was compared with the values expected from design, second we quantified the current rectification effect expected due the conical shape of the nanopores. Both tests used the same experimental setup but with electrolytes at different ionic strength. The setup

consists in two reservoirs filled with 850 mL of KCl solution separated by the membrane to study. A voltage was then applied across the membrane with a potentiostat and the resulting current response registered. Both electrode/electrolyte interface were made by means of two Ag/AgCl electrodes fabricated by anodization of Ag wires in 0,1 M HCl solution and equilibrated overnight.
The total pore surface of the membrane was assessed by measuring the conductivity of a membrane with 441 round pores of CD= 64 nm in 1 M KCl at ±0,5 V. At such concentration the EDL effect is negligible[12] and therefore the resistivity measured is directly related to the number of pores and their surface. The measured electrical resistance of the membrane with a total pore surface of 1,89 μm^2 is 5,825 MΩ ($0{,}906 \times 10^{-7}$ Sμm^{-2}). The membrane was then peeled of the silicon chip, leaving only the aperture made by KOH etching to connect the two reservoirs with an open surface of $\approx 30 \times 30\mu m$. The resistivity measured in this case is 8,123 kΩ ($1{,}367 \times 10^{-7}$ Sμm^{-2}). Although this calculation doesn't account for different effects taking place such as the entrance resistances, it can help identify broken or defectives membranes. Here the increase in conductance when the membrane is removed is coherent with the increase of total surface, i.e. the normalized conductivities measured in both cases corresponds ($0{,}906 \times 10^{-7}$ vs. $1{,}367 \times 10^{-7}$ Sμm^{-2}) thus proving the absence of leakage and the integrity of the membrane.
The current response of two membranes was then measured (figure 2.14). The measurement was obtained through cyclic galvanostatic chronoamperomery with steps of 0,1 V within the range −0,5 V to 0,5 V in a solution of 0,1 mM KCl. The voltage has been cycled 3 times and for each value the current has been stabilized during 180 s before measurement. The measurement is then done during 10 s with a sampling rate of 10 Hz. The results are shown in figure 2.14 where the ionic conductivity of two different membranes, one with round pores of 60 nm and one with wavy pores with CD of ≈ 150 nm are reported. As expected a slight rectification effect can be observed due to the conical section of the pores[29], [97]. Due to the comparable overall surface of the membranes and the fact that at 0,1 mM in both membranes there is overlap of the EDL inside the pores, the behaviour of the two membranes is similar.

2.3.4 Discussion

Considerations on materials One other fundamental characteristic of this fabrication process is the variety of materials that can be used to create the stacked membrane and the membrane thickness. Virtually any stack of evaporable material but silicon can be obtained, contrary to subtractive methods previously mentioned where the etching chemistry limits the process. Gold membranes of 100 nm of thickness with porosity controlled by design were also fabricated with the objective to easily functionalize the nanopores with thiols. For example material-selective adhesion could be used to pattern some channel region to prevent fouling [98] or to immobilize particles of interest in the desired zones of the nanopore. Simulations have shown that the grafting of polymers inside channels could change the electric potential distribution inside the pore [99] opening new opportunities for nanofluidic developments.
Non-linear effects such as current rectification arises from the conical shape of nanopores

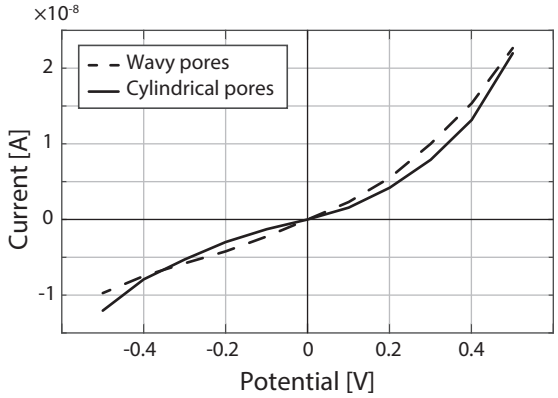

Figure 2.14 – Current–voltage curves across two different membranes measured in KCl 0.1 mM electrolyte. The curves show a slight rectification effect characteristic of pores with conical shapes, thus proving the integrity of the membrane.

[29]. Those properties can find application for biomolecule manipulation as well as transport control [70]. As previously shown this is due to the lateral growth of the evaporated thin-film that in our case results in a cone of angle $28° \pm 2°$. This peculiarity of the process depends on the evaporated material, its deposition temperature and can therefore be controlled. However to our knowledge the lateral growth during evaporation strongly depends on the material and therefore design guides cannot be provided for this aspect of the fabrication.
One emblematic property of this process is the possibility to stack multiple layers of different materials to compose the pore thanks to the combination of XeF_2 and evaporation. In this case a critical aspect to consider is the stress of the thin films and their mutual adherence. This aspect is however related to all free-standing multilayered membranes and isn't a specific characteristic of this fabrication method. In our case the membrane proposed in figure 2.12 where multiple layers of Pt and SIO_2 were stacked to compose the membrane didn't show problems of stress nor peeling after release. The variety in materials and the possibility to stack multiple layers provides unprecedented options in the choice of materials and their selective functionalization or patterning inside the nanopore, paving the way to actively gated membranes and stimulation or sensing inside the nanopore.

Significance compared to other fabrication technologies Other methods allow to obtain multilayered and nanoporous membranes or to functionalize the nanopores surface to modify their properties.
Multimaterial membranes were used to fabricate ionic field effect transistor through substractive method [37] or used to sense DNA translocation.[36] The presented fabrication method extends the materials with which such structures can be fabricated, and in particular the materials used to embed electrodes in such devices as their electrochemical properties are of crucial importance in those applications.
Functionalization of pore surface is one other research field where this fabrication method can have an impact. Different methods able to modify the physico-chemical properties of

nanopores such as ALD or covalent nanopore modification have been developed.[6] The presented technology will simplify and even extend the capability of such devices thanks to the wide choice of stacked evaporable material. For example partial or even heterogeneous functionalization of the same pore can be achieved through appropriate choices of membrane material and material-selective coatings.

2.4 Conformal deposition

The choice of a conformal process such as sputtering or CVD as deposition method for the membrane material –rather than evaporation– has several implications.
First, it allows the deposition of a wide range of materials with different technologies, from sputtering to different variants of CVD, as long as the material is deposited adherent to the template.
Second, the possibility to stack different layers on top of each other to constitute the membrane enables a fine engineering of the membrane mechanical and interfacial properties. This concept is illustrated in figure 2.15 where a stack of two materials is used to compose the membrane. The underlying material (pink) is deposited first and then covered with a second material (blue). At the end of the process the pink layer dictates the solid-liquid interface behaviour of the nanopore while the blue material doesn't contribute to the nanofluidic properties of the device but provides the desired mechanical properties to the structure. This allows the use of materials for the interface nanopore-electrolyte that are usually not suitable for monolithic membranes for the sake of cost, mechanical properties or quality of deposition.

As proof-of-concept we present here a passive nanoporous membrane made of a thin layer of a-C:N:H[100] as interface material and SiO_2 as structural material, embedding nanopores with critical dimensions from 30 nm to 70 nm, 1,2 µm long, with round and elongated geometries. a-C:N:H can be easily deposited through CVD and has a wide polarizable window [101], it is therefore an ideal candidate for nanopore-liquid interface material in gating applications. SiO_2 on the other hand is inert, electrically insulating and mechanically robust which justify its choice as structural material.

2.4.1 Method

Membrane deposition The material composing the membrane-electrolyte interface (the membrane material, in pink in figure 2.15.2) and the material physically supporting the membrane (the support material, in blue in figure 2.15.2) were conformally deposited on top of the templates through PECVD. The membrane material was a thin-film of a-C:N:H, 250 nm thick, deposited through PECVD (Oxford PlasmaLab 100, 50 W of RF generator power, 800 mtorr deposition chamber pressure at a temperature of 45 °C for 40 min).[100] On top of it a layer of 2 µm of SiO_2 was deposited as support material through PECVD (Oxford PlasmaLab 100, 20 W of RF generator power, 1500 mtorr deposition chamber pressure at a temperature of

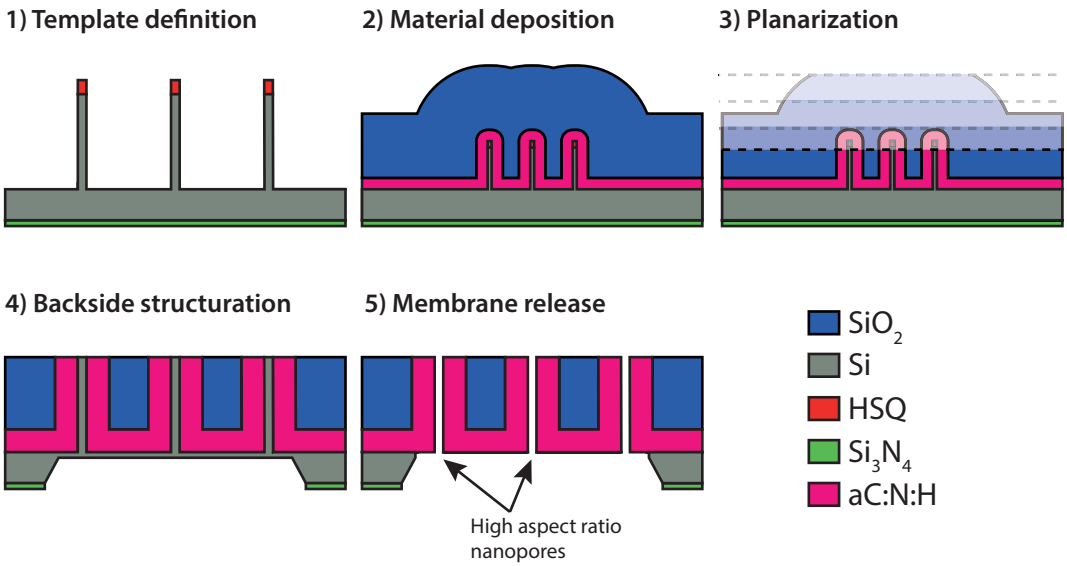

Figure 2.15 – Graphical representation of the major steps of the fabrication of nanoporous membranes through conformal deposition on sacrifical silicon templates. First, the templates are fabricated with the desired nanopores geometry **1)**, then the hydrogenated amorphous carbon–nitrogen (a-C:N:H) (pink) and SiO_2 (blue) layers composing the membrane are deposited on top of the sacrifical templates through PECVD **2)** and planarized thorugh a combination of CMP and IBE **3)**. The backside of the wafer is then structured **4)** and the nanopores are finally released through XeF_2 etch **5)**. **6)** The resulting membranes are made of the first material deposited (a-C:N:H) and their shape is the exact negative of the templates.

300 °C for 40 min).

Planarization The deposited materials were then planarized using a combination of chemical mechanical polishing (CMP) and ion beam etcher (IBE) (figure 2.15.3). A short CMP step (ω_{head} = 65 rpm, ω_{plate} = 75 rpm, head pressure = 0,76 bar, polishing time = 1 min, backside pressure = 0,76 bar, slurry 30N50 from KLEBOSOL, on a pad IC1000 from DOW with a specific gravity of 0.794) is used to level the wafer and remove the excess of material over the templates. Once the surface is leveled, IBE (Veeco NEXUS IBE350, 600 W, at an incidence angle of 60°) is used to uniformly erode the support material until the buried silicon templates surface.

Membrane release To release the membranes a combination of KOH and XeF_2 etching was used (figure 2.15.4). First the Si_3N_4 backside layer was structured as hard mask using standard photolithography processes (2 µm of AZ9260 as photoresist) followed by He/CHF_3 based DRIE to expose the silicon underneath. The wafer was then etched in KOH (40% at 60 °C for about 19 hours) using a waterproof teflon chuck to protect the frontside until only a few microns of silicon were left. At this point the wafer was diced and stored in this state until needed. Just before use, to completely release the membranes from the last microns of silicon and remove the sacrificial nanostructures, the chips were etched with pulsed XeF_2 gas (50 × 30 s at

2700 mbar).

2.4.2 Results

Impact of conformal deposition process on design The process used to depose SiO_2, being not perfectly conformal, left some voids between nanostructures when the pitch wasn't greater than the height of the structures. This is a well known and characterized process exploited even to fabricate nanochannels.[102] In our case, given the high aspect-ratio of the structures, the relationship between the desired thickness of a membrane and the minimal distance between pores (pitch) needs to be considered when designing the membrane. Membranes with templates too closely packed together will result in small bumps around the pores and a thinned membrane, whereas a membrane with templates sufficiently spaced from each other will not suffer from these limitations. In figure 2.16 an array is shown with 1 µm tall structures either spaced 1 µm (left) or 3 µm (right). The FIB cross-sections on top show how the void is a direct consequence of the deposition method and pitch between nanostructures. The SEM micrographs at the bottom show the effect of the presence of voids on the structure of the membrane after planarization. Such voids are not present when the pitch is greater than twice the height of the nanostructures, thus the membrane is flat as shown in figure 2.16.

Planarization characterization The process of uncovering the buried silicon nanostructures through planarization and thinning of the membrane material is of utmost importance, since the thickness and surface quality of the membrane depends on it.
CMP is the reference process for planarization and thinning of films but suffers from some important drawbacks: it's difficult to obtain a uniform etch rate at the wafer scale and the whole process is strongly material-dependant which means that the results on heterogeneous structures would have to be optimized for every material combination. IBE doesn't suffer from those problems since it is not a material-dependent process and has an uniform etch-rate at the entire wafer scale. However, IBE isn't suitable for planarization since its nature tends to preserve the surface topography of the wafer rather than planarize it. The strategy we adopted efficiently combines CMP and IBE to take advantage of both techniques. First, an uniform flat surface is obtained with a short CMP step (≈1 min) that levels the wafer without significantly affecting the native uniformity of the film. Then IBE is used to uniformly etch the entire frontside of the wafer until the buried silicon nanostructures surface from the surrounding material (figure 2.17). In order to prevent prematurely reaching the underlying a-C:N:H layer or the silicon structures early during the CMP step, about 1 µm of SiO_2 in excess has been deposited, this way the CMP process will "see" only the SiO_2 layer on top, independently of the material underneath.

More in detail, a suboptimal CMP process for SiO_2 was characterized on three different wafers for three different etch times (1 min, 2 min and 3 min). The thickness and uniformity of the SiO_2 film was measured before and after CMP on 25 points with an interferometer to evaluate

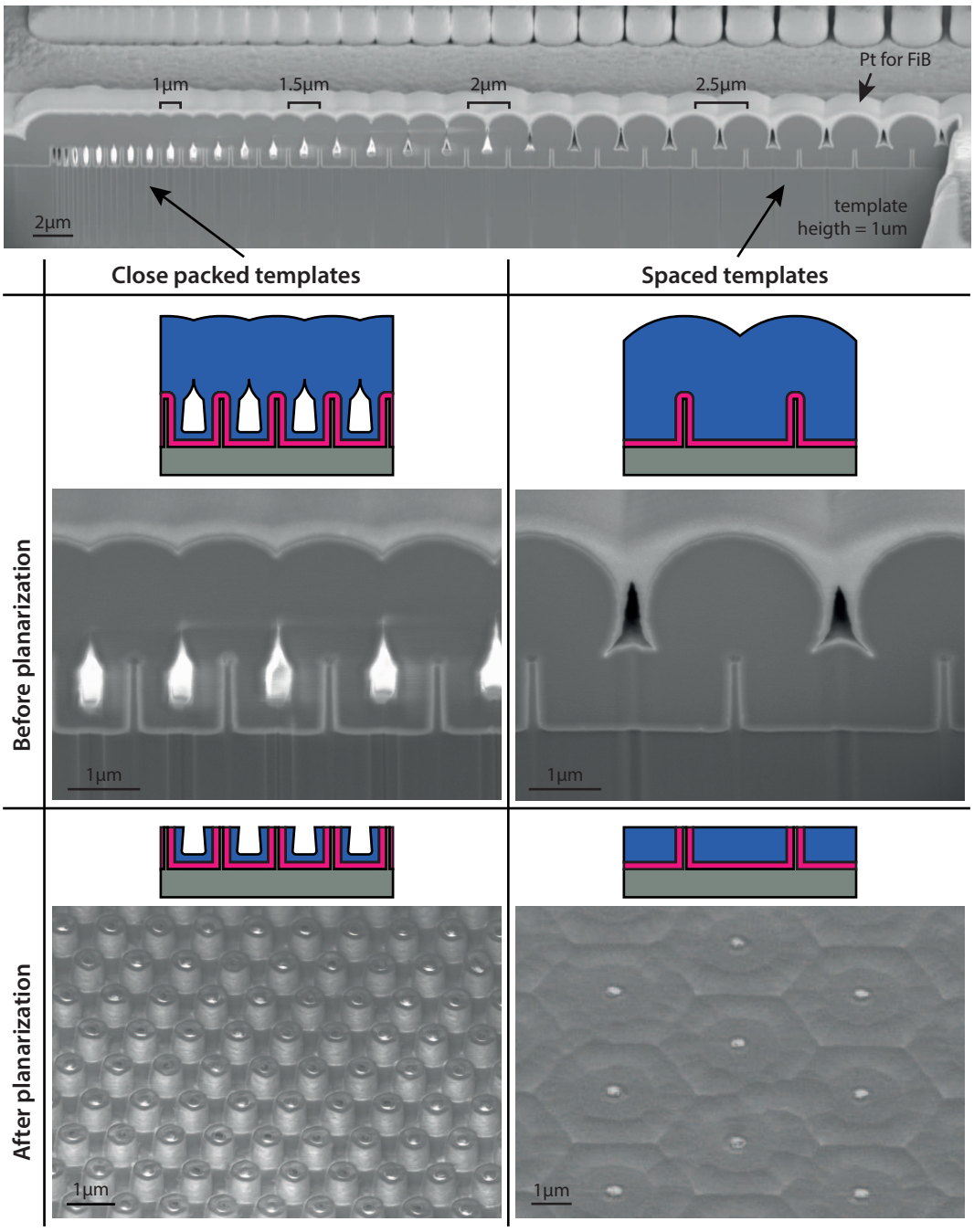

Figure 2.16 – FIB and SEM micrographs showing the effect of the nanostructure pitch on the nanoporous membrane (all images are taken with a tilt of 45°). When the pitch between silicon nanostructures is smaller than twice their height (**left**), voids form between the structures. When the pitch is greater (**right**), the nanostructures are well covered and no voids are observable. The **bottom** images shows the impact of a proximity effect once the samples are planarized. Voids present when nanostructures are closely packed cause a thinning of the membrane between nanopores (**left**). When the nanostructures are spaced enough, the membrane shows no defects (**right**). Scale bars on all figures are 1 µm

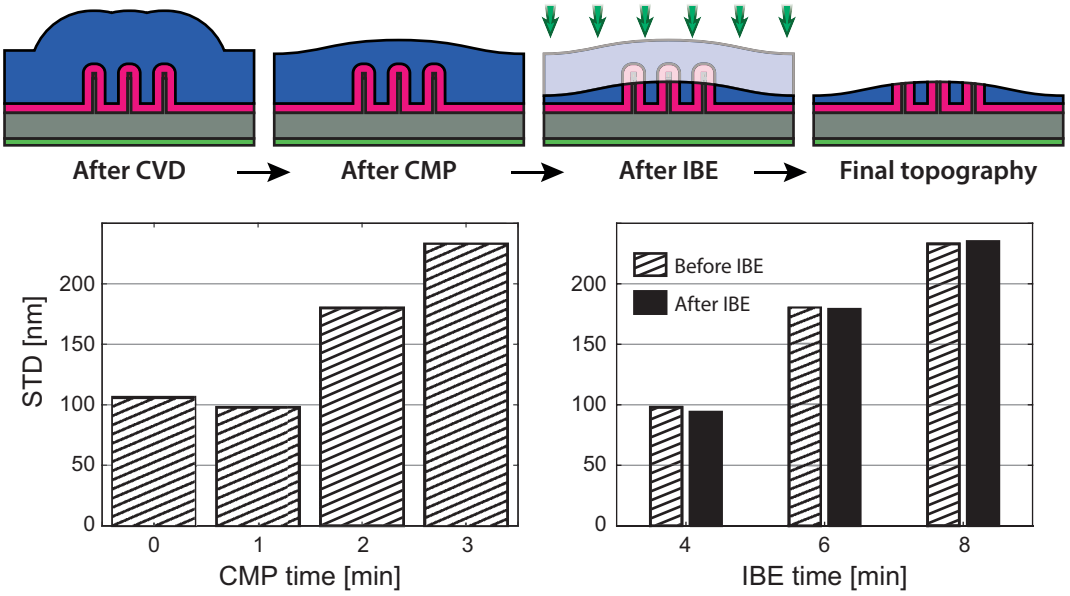

Figure 2.17 – The diagram at the **top** shows the rationale of the planarization process developed, consisting of a short polishing step with CMP (1 min) to remove the "bumps" over the templates, followed by an IBE etch to expose the buried silicon nanostructures. At the **bottom - left** is shown the increase in the standard deviation (STD) of a SiO_2 layer with CMP time, measured on three different wafers. At the **bottom - right** , the same three wafers are measured before and after IBE at 4 min, 6 min and 8 min etch, showing no significant variation in STD of the films after IBE.

the rate and uniformity of the process. Although the etch rate can be considered constant ($350\,nm\,min^{-1}$) the uniformity of the film decreases with the CMP time. It is clear from figure 2.17 - left how, after 1 min of CMP, the non-uniformity of the SiO_2 film, represented by the standard deviation of the thickness of the SiO_2 layer on the entire wafer surface, increases with the etch time. The same wafers were then processed with IBE at three different times (4 min, 6 min and 8 min) to characterize etch rate and uniformity of the process. Figure 2.17 - right, shows how the measured standard deviation remains unchanged before and after IBE etch, and this independently from the etch time. Furthermore the measured IBE etch rates are extremely reproducible and were measured to be $(80 \pm 3)\,nm\,min^{-1}$.
The precision and control provided by this technique was consistently used to level and thin SiO_2 films with a precision of $\pm 10\,nm$ independently of the combination of materials used and without having to adapt the CMP nor IBE parameters.

Membrane release and final results By combining the controlled nanostructure fabrication and the planarization method previously mentioned, arrays of silicon templates embedded in a-C:N:H and SiO_2 were fabricated. The fabricated array had 441 template nanostructures disposed in an hexagonal lattice and spaced 1 µm and 3 µm. The structures didn't show defects and had uniform thickness and template geometry along the entire array (figure 2.18 - top-left).

Figure 2.18 - top-right shows further magnification on nanopillars and wavy nanofins silicon

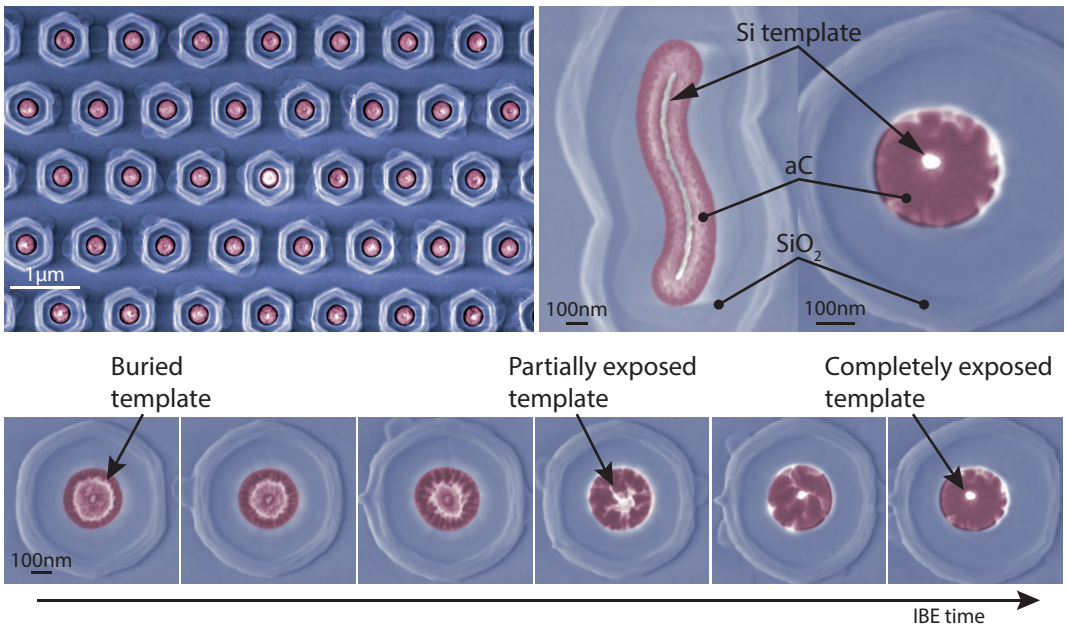

Figure 2.18 – Colored SEM micrographs showing the templates embedded in the a-C:N:H/SiO_2 matrix before XeF_2 release. **Top-left**: An entire membrane (30 µm × 30 µm) , where all 441 template nanopillars with diameters of 40 nm uniformly surface from the surrounding a-C:N:H without showing defects. Scale bar is 1 µm. **Top-right**: Two templates of different shape (nanofin and nanopillar) surfacing from a-C:N:H and SiO_2. The silicon templates can be easily distinguished in the middle, as well as the amorphous carbon surrounding them, colored in pink. Scale bars are 100 nm. The **bottom** image shows a time-lapse image of the IBE process to expose the silicon templates.

templates embedded in a-C:N:H and SiO_2 right before XeF_2 release. In figure 2.18 - top-right the 40 nm silicon template is clearly distinguishable as a brighter spot in the middle of the image. The amorphous carbon layer surrounding the template is a slightly recessed in the SiO_2 film because of its minimally different etch rate during IBE process. Wavy template nanofins with critical dimensions of 30 nm shown in figure 2.18 - top-right were successfully processed without any modifications of the fabrication process used for the template nanopillars. No differences in terms of uniformity or stability of the process were observed compared to the columnar templates or depending on different materials combinations tested.

Following a partial backside KOH etch, the silicon template nanostructures were removed through XeF_2 etching, revealing nanopores whose shape corresponds to the negative of the silicon nanostructures (figure 2.19).
As previously discussed, XeF_2 has a key role in the fabrication process, since its high selectivity to Si allows a wide spectrum of materials to be used without having to adapt the release of the nanopores to the material used and without compromising the final geometry of the nanopore being XeF_2 purely chemical (*i.e.* without the physical ion bombardment characteristic of plasma etching).

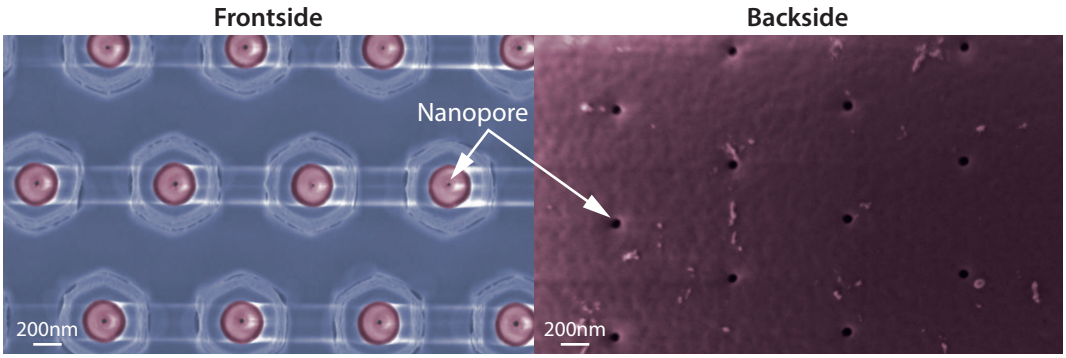

Figure 2.19 – Colored SEM micrograph of the frontside (**left**) and backside (**right**) of a conformally deposited membrane with 40 nm nanopores, after XeF_2 release. The a-C:N:H layer is in pink, while the SiO_2 layer is in blue.

2.4.3 Electrical characterization

To verify the functionality and integrity of the membrane, its transmembrane electrical resistance was measured and compared to theoretical predictions.
A membrane with 441 circular nanopores of 40 nm of diameter and 630 nm long was placed between two reservoirs filled with 850 mL of KCl 1 M (figure 2.20 - left). A voltage was then applied across the membrane with two Ag/AgCl electrodes fabricated by anodization of a silver wire in 0,1 M HCl and equilibrated overnight in a solution of KCl 1 M, and the current flowing across the membrane in function of the transmembrane voltage was measured with a potentiostat (figure 2.20 - right). To calculate the resistance of the membrane any nanofluidic effects were neglected since the high electrolyte concentration results in no overlap of the electrical double layer, therefore the theoretical resistance of the system is dictated purely by its geometrical parameters. The total resistance of the system is the sum of the geometrical resistance of the membrane R_{mem}, the access resistance for each pore on both sides of the membrane R_{acc}, and the resistance of the KOH pyramid, R_{KOH}. The bulk resistance R_{bulk} and the electrode-electrolyte interface resistance were neglected. The geometrical resistance for a membrane with n pores of diameter $2r$ and length L is defined as :

$$R_{mem} = \rho_{\text{KCl}} \frac{L}{n\, A_{\text{pore}}} = \rho_{\text{KCl}} \frac{L}{n\, r^2 \pi} \tag{2.1}$$

where ρ_{KCl} is the resistivity of KCl 1 M. The access resistances were estimated using the formula given by Hall as[103]

$$R_{acc} = \rho_{\text{KCl}} \frac{1}{n\, 4r} \tag{2.2}$$

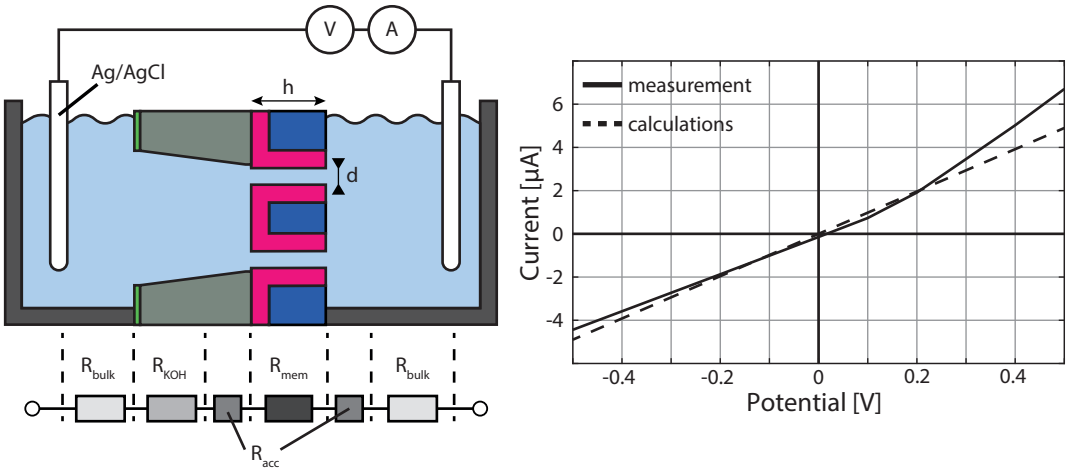

Figure 2.20 – The diagram of the setup used to measure the transmembrane resistivity is shown on the **left**. At the bottom is represented the equivalent electrical circuit used to calculate the theoretical I-V curve. On the **right** is shown the I-V current measured as a function of the transmembrane voltage applied in a 1000 mM KCl solution through a membrane with 441 nanopores and diameters of 40 nm and thickness of 630 nm. The dashed lines correspond to the geometrical resistivity calculated for the tested geometry.

and the KOH pyramid resistance was calculated as

$$\begin{aligned} R_{KOH} &= \rho_{\mathrm{KCl}} \int_0^h \frac{dx}{(d+\frac{x(D-d)}{2h})^2} \\ &= \rho_{\mathrm{KCl}} \frac{2h}{d-D}\left(\frac{2}{D+d}-\frac{1}{d}\right) \end{aligned} \tag{2.3}$$

where d and D are respectively the size of the small and large side of the KOH pyramid and h is the thickness of the wafer. The total electrical resistance of the membrane is therefore

$$R_{tot} = R_{\mathrm{KOH}} + R_{\mathrm{mem}} + 2\,R_{\mathrm{acc}}. \tag{2.4}$$

A fracture, leakage or defect in the membrane would result in currents greater than expected and, since the measurements are in good agreement with theoretical data, we can assume the integrity of the membrane and absence of leakages. This demonstrates the high control over geometrical parameters achievable with the presented fabrication strategy.

2.4.4 Discussion

Considerations about pore geometry In applications such as nanofluidic transistors[30] or diodes[23], the critical dimension of the nanochannel has to be smaller than twice the Debye length for the EDL overlap to occur. [1], [104], [105]
By controlling the geometry of the nanopore it will be possible to fabricate membranes capable

Table 2.1 – Numerical values of parameters used in equations 2.1 to 2.4.

Variable	Value	Variable	Value
n	441	r	20×10^{-9} m
L	630×10^{-9} m	$1/\rho_{\mathrm{KCl}}$	11,88 S m^{-1}
d	60×10^{-6} m	D	600×10^{-6} m
h	380×10^{-6} m		
R_{mem}	$95{,}69 \times 10^{3}\ \Omega$	R_{acc}	$2{,}38 \times 10^{3}\ \Omega$
R_{KOH}	$1{,}61 \times 10^{3}\ \Omega$	R_{tot}	$102{,}08 \times 10^{3}\ \Omega$

to discriminate specific molecules or particles. Experiments have shown that by engineering longitudinal irregularities inside nanopores the shape and volume of translocating objects can be deduced.[106] Such nanopores could be fabricated by slightly modifying the fabrication process previously presented by using an alternate Bosch-process to fabricate corrugated templates. This would result in nanopores with corrugations where the roughness of the structure is defined by the scalloping effect.[107]
The same nanopores with controlled corrugation but made of hydrophobic materials could be used to produce membranes with extremely low hydrodynamic resistance, which may be particularly efficient in the study of streaming currents.
At last, the presented method allows controlled fabrication of high aspect-ratio nanopores regardless of the materials used, which is impossible to imitate with other manufacturing techniques. This opens up interesting perspectives for electro-osmotic control of flows where effects of back-pressure flows will be mitigated by the higher hydrodynamic resistance of high aspect-ratio nanochannel.

Discussion on materials Membranes made of a-C:N:H-SiO_2 and purely SiO_2 were successfully fabricated with the very same process and showed the same quality in terms of pore geometry and yield. The possibility to change and stack materials as desired without the need to adapt the fabrication process, and the variety of materials that can be used has many implications.
The compromise between interface properties and mechanical stability of the membrane often necessary for monolithic membranes can be easily avoided. The function to mechanically support the membrane is entrusted to the passive material (in this case SiO_2) whereas the interface properties of the nanopore can be optimally chosen for the desired application (a-C:N:H in our case) as long as it can withstand XeF_2. The etch selectivity of XeF_2 to silicon enables the fabrication of nanopores made of exotic or expensive materials with lengths and geometries that would not be possible with other techniques for sake of mechanical stability, material-stress or cost. Additionally to a-C:N:H-SiO_2 and monolithic SiO_2, we did explore the use of other materials. A membrane with 200 nm of Platinum (Pt) at the nanopore-electrolyte interface and SiO_2 as structural material, was fabricated with the same process used for a-C:N:H-SiO_2 and SiO_2 membranes. Furthermore, the number of combined materials isn't

limited to two. Additional layers can be integrated in the stack that once planarized could behave as functional electrodes directly integrated in the membrane.
This flexibility in the choice of materials opens new opportunities for easy functionalization of nanopores since the most appropriate membrane-material/surface-chemistry couple can be chosen.[75] Simulations have shown that grafting charged polymers inside nanopores dramatically impacts the potential distribution inside nanochannels,[99] or that nanopores functionalized with polyethylene glycol (PEG) may prevent fouling in an efficient way.[98]
For example, high aspect-ratio gold nanopores, easily functionalizable with thiol-terminated molecules, can be fabricated in a reliable and cost efficient way with the presented method by stacking a thin layer of gold and chrome (for adhesion) and a thick layer of SiO_2 as structural support.
One other promising class of materials to investigate are polarizable materials such as boron doped diamond (BDD), diamond-like carbon (DLC) or a-C:N:H.[101], [108]–[110]
Nanopores made of polarizable materials at the nanopore-electrolyte interface are suitable for gating applications since they are capable to apply a potential at an interface without leakage currents. This way it is possible to directly modulate the magnitude and polarity of the surface charge at the nanopore-liquid interface with low or null leakage currents, thus getting rid of the insulating layer and its electric field damping as further explained in section 4.2. [30], [111], [112]

2.5 Conclusion

In this chapter a new method for the fabrication of solid-state nanoporous membranes with controlled porosity, pore geometry, thickness, and material composition was demonstrated. The method relies on the use of sacrificial silicon nanostructures used as templates to cast the nanopores, thus being compatible with a wide range of materials.
Critical aspects and limitations of the use of sacrifical templates for the fabrication of nanoporous membranes, including an attainable maximal aspect-ratio of 35, the relation with the template shape and its stability, and the trade-off between porosity and membrane thickness were discussed in the first section.
The impact of the choice of the deposition method to cast the nanopores, –whether directional through evaporation or conformal through CVD and sputtering– was showed and thoroughly discussed.
The use of directional deposition allows to manufacture multilayered membranes embedding nanopores with conical shapes in a wide variety of materials, also providing the possibility to control the pore material along the pore axis by stacking multiple layers.
The use of conformal deposition methods results in nanopores with smaller CD and greater aspect ratios than with evaporation (down to 30 nm in diameter and with an aspect ratio of 35), but does not allow the possibility to engineer the material along the nanopores.
The functionality and integrity of the fabricated membranes as well as the high control provided on geometrical parameters has been proven through transmembrane resistivity mea-

surements and extensive SEM inspections and image processing.
Manufacturable alternatives of nanopore geometries and materials enabled by the presented method leading to innovative applications of nanofluidic membranes were also discussed.
The proposed method relies on cleanroom process which are widespread, reliable, well controlled, quick and uniform at the wafer scale (unlike, for example FIB). The process is easily integrable within a more complex process flow (e.g. for microfluidic channels fabrication) and endows the integration of multiple membranes with different properties and geometries within the same device.
The presented method therefore provides a new tool to fabricate nanoporous membranes at the wafer scale with simultaneous control over nanopore shape, material and placement. The freedom in tailoring the membrane characteristics to the desired application will open new perspectives in the field of functional materials or active control of molecules inside nanopores [75].

3 Theoretical functioning of a nanofluidic transistor

In this chapter the physical phenomena happening in close contact of a surface and more specifically inside a nanochannel are mathematically described. This chapter is meant as a support for the arguments discussed in the next chapter rather than as a rigorous description of all the nanofluidic phenomena inside a nanochannel, exhaustively discussed in the literature.

To describe the behaviour of liquids confined in nanometric volumes, concepts of fluid mechanics, electrochemistry and electrostatics known for decades were combined. This chapter first describes the origin of surface charge and the resulting electric double layer (EDL). Then the Poisson-Boltzmann model and its linear approximation are introduced to describe the influence of the critical dimension of a nanochannel. The implications of the surface potential of a nanochannel of a fluidic transistor are shown with the Grahame equation and finally an overview and quantification of electroosmotic and electrophoretic flows in nanochannels are given. The interested reader can refer to the following selection of rewiew papers and books that describe these phenomena in details and from different points of view:

- Daiguji and Sparreboom *et al.* introduce the underlying principles of nanofluidics without delving too deep in the mathematical descriptions and highlights their role in the functioning of nanofluidic diodes and transistors.[1], [12]
- Schoch and coworkers tackle the physical properties and operational mechanisms of nanofluidics from a mathematical point of view. This is one of the most cited papers in the entire field of nanofluidics with most than 1000 citation according to *Google Scholar* and 786 according to *Web of science*[1].[105]
- Bocquet and Charlaix focus on the interplay of fluid dynamic effects over different length scales, and describe a parallelism between nanofluidics and semiconductor physics.[14]

[1] on date 17. October 2017

- Pardon and coworkers thoroughly discuss the specific case of the nanofluidic transistor and analyse the relevance of different models and assumptions. It is the most complete review on nanofluidic transistors to date.[112]
- Brian J. Kirby in his book *"Micro-and nanoscale fluid mechanics: transport in microfluidic devices."* gives the most complete overview of nano and micro fluid mechanics, starting from the basics until the most advanced applications, with extensive details on matemathical derivations. The following chapter is based on this book for what concerns the mathematical developments.[4]

3.1 Surface charge

When a solid is in contact with a liquid a net surface charge is induced by two distinct phenomena: adsorption of specific ions, regulated by their affinity to the surface, and dissociation of chemical groups in the solvent. The latter phenomena is particularly relevant in nanofluidics since the surface charge of SiO_2, probably the most used material for nanochannels interface, is due to the acid dissociation of silanol groups in water following:

$$SiOH \underset{\longleftarrow}{\overset{K_a}{\longrightarrow}} SiO^- + H^+ \tag{3.1}$$

where K_a is the acid dissociation constant, often defined in its logarithmic form $pK_a = -\log K_a$. The quantity of SiO^- groups that induce a net surface charge is dictated by the quantity of H^+ ions in the solution meaning that the surface charge depends from the pH of the solvent. The surface charge q_{surf} can therefore be expressed as a function of the pH and pK_a as

$$q_{surf} = -e\Gamma \frac{10^{\alpha(pH-pK_a)}}{1+10^{\alpha(pH-pK_a)}} \tag{3.2}$$

where Γ is the total density of SiO^- and SiOH sites, α is a parameter describing the spread of values for pK_a in a non-ideal solution[2], and e is the elementary charge. The interested reader can refer to [4, p. 229] and the Appendix B of the same reference where the dissociation process for different materials and solvents are described in detail.

3.2 The Electrical Double Layer (EDL)

As described in section 1.1.2 the electric double layer (EDL) stems from the presence of a surface charge q_{surf} at the solid-liquid interface generating a potential difference between the surface and the bulk $\varphi_0 = \phi_{surface} - \phi_{bulk}$. The EDL consist in a region characterized by an accumulation of *counter-ions* and a depletion of *co-ions* in close proximity to the interface and is modelled as two layers in series: a region of counter-ions bound to the surface, the so called *Stern layer*, and a diffuse region rich in counter-ions gradually fading toward the bulk. as shown in figure 3.1 - left. The potential at the interface Stern/diffuse layer with respect to

[2] $\alpha = 1$ for ideal solution. For real solutions typical values are between 0,3 and 0,7.

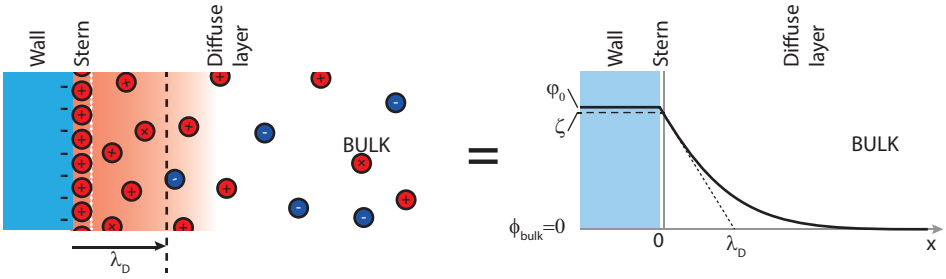

Figure 3.1 – Structure of the EDL in the case of a negatively charged surface.

the bulk is named ζ-potential, which is often mistakenly referred as the surface potential φ_0 (figure 3.1 - right). The ζ potential is typically measured in electroosmotic experiments and at high ionic strength and low surface charges the approximation $\zeta = \varphi_0$ can be made.

3.3 Poisson-Nerst-Planck-Stokes model

The ionic population at equilibrium inside the EDL can be described with three differential equations:

The Poisson equation describes the relationship between the net local charge density ρ_E in the EDL and the electric potential φ as:

$$\nabla^2\varphi = -\frac{\rho_E}{\varepsilon} \tag{3.3}$$

where ε is the permittivity of the electrolyte. The local charge density ρ_E is expressed as

$$\rho_E = \sum_i F c_i z_i \tag{3.4}$$

where F is the Faraday constant and z_i and c_i are the valence and concentration respectively of each different ionic species i.

The Nernst-Plank equation describes the mass transport of charged species $\frac{\partial c_i}{\partial t}$ in relation to their electrochemical potential profile and the convective flows $\vec{u}$. In absence of chemical reactions the equation is defined as:

$$\frac{\partial c_i}{\partial t} = \nabla\cdot\Big(\underbrace{D_i\nabla c_i}_{\text{diffusion}} + \underbrace{\frac{D_i}{k_B T} z_i e c_i \nabla\varphi}_{\text{electrokinesis}}\Big) - \underbrace{\nabla(c_i\vec{u})}_{\text{convection}} \tag{3.5}$$

Where D_i is the diffusion constant for each ion, e represents the elementary charge, k_B is the Boltzmann constant and T is the temperature of the system. The Nernst-Planck equation consist in three terms: a diffusive term equivalent to Fick's law, an electrokinetic term that describes the migration of ions when exposed to an electric field (electrophoretic flow (EP), further discussed in this chapter) and a convective term

that describes the influence of the solvent flow on the movement of the ions.

The Stokes equation describes the convective flows $\vec{u}$ in relation to external forces **F** such as external pressure p or electroosmotic forces, and is the approximation for incompressible and laminar flows of the more complex Navier-Stokes equation. It is defined as

$$\nabla p = \eta \nabla^2 \vec{u} \tag{3.6}$$

Those three partial equations can be summarized as:

$$\begin{aligned} \text{Poisson:} \quad & \varphi \propto c_i \\ \text{Nernst-Planck:} \quad & c_i \propto \varphi, \vec{u} \\ \text{Stokes:} \quad & \vec{u} \propto \mathbf{F}(\varphi, \mathbf{c_i}) \end{aligned} \tag{3.7}$$

3.4 Poisson-Boltzmann equation

Each ionic specie i present in the EDL obey to the Boltzmann statistics. Their concentration is therefore dictated by the Boltzmann distribution as a function of the electric potential as

$$c_i = c_{i,\infty} \exp\left(-\frac{z_i F \varphi}{RT}\right) \tag{3.8}$$

where $c_{i,\infty}$ is the bulk concentration of the ionic specie i and $R = k_B N_A$ is the universal gas constant. In the bulk $\varphi = 0$ and the equation simplifies to $c_i = c_{i,\infty}$.
The Boltzmann definition 3.8 can be combined with the Poisson equation 3.3 and equation 3.4 to obtain the general formulation of *non-linear* Poisson-Boltzmann model:

$$\nabla^2 \varphi = -\frac{F}{\varepsilon} \sum_i c_{i,\infty} z_i \exp\left(-\frac{z_i F \varphi}{RT}\right) \tag{3.9}$$

Normalization and Debye length The non-linear Poisson-Boltzmann equation 3.9 can be normalized by expressing the electric potential in terms of the thermal voltage $V_{\text{th}} = RT/F \approx 25\,\text{mV}$ as:

$$\nabla^2 \varphi^* = -\frac{1}{2} \underbrace{\frac{2F^2 I_c}{\varepsilon RT}}_{1/\lambda_D^2} \sum_i \frac{c_{i,\infty}}{I_c} z_i \exp\left(-z_i \varphi^*\right) \tag{3.10}$$

where $\varphi^* = \varphi \frac{F}{RT}$ and $c_{i,\infty}$ has been normalized to account for the ionic strength of the bulk I_c (in SI units: mM).
The variable λ_D is called the Debye length and gives a rough estimation of the extension of the

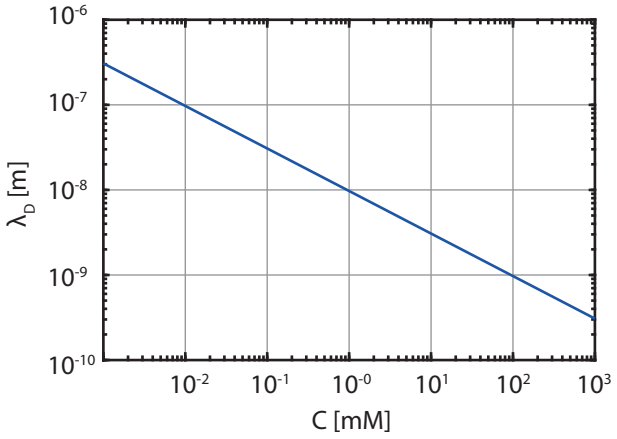

Figure 3.2 – Debye length λ_D vs. the ionic strength as described by equation 3.11

EDL into the bulk.

$$\lambda_D = \sqrt{\frac{\varepsilon RT}{2F^2 I_c}} \tag{3.11}$$

The Debye length is inversely proportional to the ionic strength of the solution, because the increase in concentration of the solution increases the the concentration gradient from the bulk to the surface and therefore the balance between the Brownian motion and the electrostatic forces. The EDL is reduced from 100 nm at $I_c = 1 \times 10^{-2}$ mM down to 0,5 nm at $I_c = 1 \times 10^{3}$ mM as shown in figure 3.2.
In nanofluidics this is important because it defines the minimal dimension $2 \times \lambda_D$ of a nanochannel for which the EDL of the walls begin to overlap and effects such as permselectivity and ionic exclusion start to be observable.

Importance of KCl as symmetric electrolyte If we consider an infinite flat surface in contact with a uniform solvent we can reduce the Poisson-Boltzmann equation to one dimension x as

$$\lambda_D^2 \frac{\partial^2 \varphi^*}{\partial x^2} = -\frac{1}{2} \sum_i \frac{c_{i,\infty}}{I_c} z_i \exp\left(-z_i \varphi^*\right) \tag{3.12}$$

In many nanofluidic experiments the electrolyte of choice is aqueous KCl that when dissolved in water it is completely ionized into solvated K^+ and Cl^-. KCl can be considered as a symmetric electrolyte since the number of K^+ and Cl^+ ions is equal, the ions have a symmetric valence of ± 1 and the diffusivity constants are almost identical for both ions (between $1{,}8 \times 10^{-9}\,\mathrm{m^2\,s^{-1}}$ to $2{,}0 \times 10^{-9}\,\mathrm{m^2\,s^{-1}}$ as reported by Lobo and coworkers[113]). KCl is therefore very interesting in nanofluidic experiments since it allows to strongly simplify the system by assuming $c_{i,\infty} = c_{K^+} = c_{Cl^-}$ (and therefore $c_{i,\infty}/I_c = 1$) and $z_{K^+} = 1$, $z_{Cl^-} = -1$. Equation 3.12 can be

therefore analytically solved and simplifies to:

$$\begin{aligned} \lambda_D^2 \frac{\partial^2 \varphi^*}{\partial x^2} &= -\tfrac{1}{2}[\exp(-\varphi^*) - \exp(\varphi^*)] \\ &= \sinh(\varphi^*) \end{aligned} \tag{3.13}$$

3.5 Debye-Hückel approximation

For voltages smaller than the thermal voltage (or for $\varphi^* < 1$) the non-linear normalized Poisson-Boltzmann (equation 3.10) can be linearized as a Taylor series of first order by setting $\exp(x) \approx 1 + x$. This results in the so-called Debye-Hückel approximation defined as:

$$\lambda_D^2 \frac{\partial^2 \varphi^*}{\partial x^2} = -\frac{1}{2} \sum_i \frac{c_{i,\infty}}{I_c} z_i^2 \varphi^* \tag{3.14}$$

Which for a symmetric electrolyte is simplified to

$$\begin{aligned} \lambda_D^2 \frac{\partial^2 \varphi^*}{\partial x^2} &= -\tfrac{1}{2}(\varphi^* + \varphi^*) \\ &= \varphi^* \end{aligned} \tag{3.15}$$

The linearised Poisson-Boltzmann equation can be used to analytically describe the evolution of both potential and concentration of ionic species in the electrolyte according to the distance x from the wall.

Semi-infinite domain solution In the case of a flat surface in contact with a infinitely extended liquid, the equation 3.15 can be solved with the boundary conditions of $\varphi = 0$ at $x = +\infty$ and $\varphi = \varphi_0$ at $x = 0$. This is called the semi-infinite solution and is valid for all systems when λ_D is much smaller than the characteristic dimension of the reservoir of the liquid under examination (figure 3.3).

$$\begin{aligned} \varphi(x) &= \varphi_0 \exp(-x/\lambda_D) \\ c_i(x) &= c_{i,\infty} \exp\left(-\tfrac{z_i F}{RT} \varphi(x)\right) \end{aligned} \tag{3.16}$$

In this equation λ_D determines the exponential constant of the potential as shown in figure 3.3, bottom.

Nanoslit solution On the other hand, when the characteristic dimension of the channel under examination is equal or smaller than λ_D, the solution must consider the influence of the other walls. A nanoslit is a nanochannel which has one dimension equal or smaller than

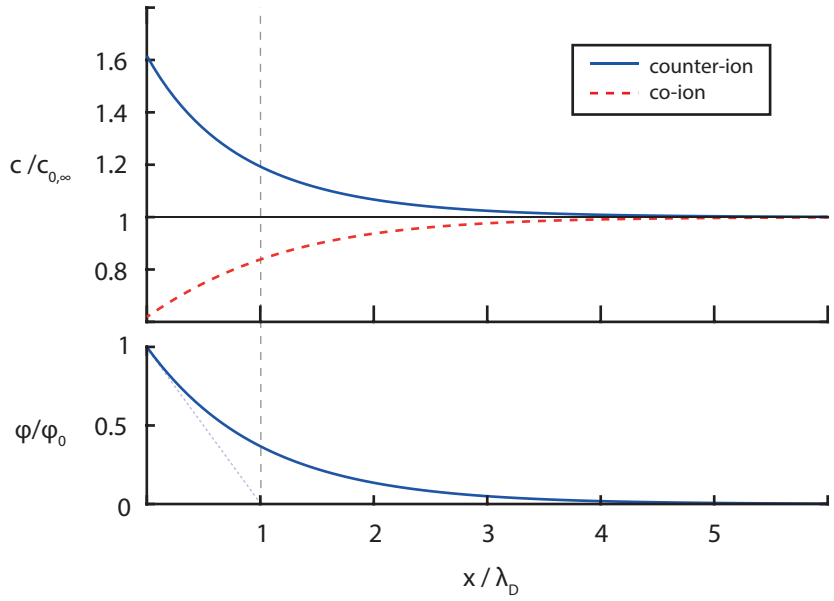

Figure 3.3 – Semi-infinite domain. **Top:** Co- and counter-ion concentration in the EDL. **Bottom:** Exponential decrease of the electrical potential φ away from the interface.

$2 \times \lambda_D$, typically 5 nm to 100 nm and the other two dimensions much greater than λ_D. This structure can be modelled as two infinite parallel plates spaced by a distance $\pm d$ from the origin. The linearized Poisson-Boltzmann equation can now be solved with the boundary conditions $\varphi(x = d) = \varphi(x = -d) = \varphi_0$ and $\varphi'(x = 0) = 0$ to obtain

$$\begin{aligned} \varphi(x) &= \varphi_0 \frac{\cosh(y/\lambda_D)}{\cosh(d/\lambda_D)} \\ c_i(x) &= c_{i,\infty} \exp\left(-\frac{z_i F}{RT}\varphi(x)\right) \end{aligned} \tag{3.17}$$

Figure 3.4 shows the evolution of the potential and concentration inside a 20 nm slit (d = 10 nm) which walls have an equivalent potential of $\varphi_0 = V_{\text{th}} = 25$ mV (which is relatively high, considered that it is the upper limit of validity of the Debye-Hückel approximation) at two different electrolyte concentrations. At 0,1 mM, $\lambda_D = 30$ nm $> d$ and therefore there is EDL overlap in the channel. It is possible to observe how the electrical potential is almost constant across the channel which results in a three-fold increase of the concentration of counter-ions inside the channel and one almost complete exclusion of the co-ions. At 100 mM, $\lambda_D = 1$ nm $\ll d$ and there is no overlap in the middle of the channel. The solution, when considering only one side of the nanochannel, is identical to the semi-infinite domain solution presented in figure 3.3. In this case the ionic enrichment is present only close to the walls of the channels but the local charge density equilibrate in the center.

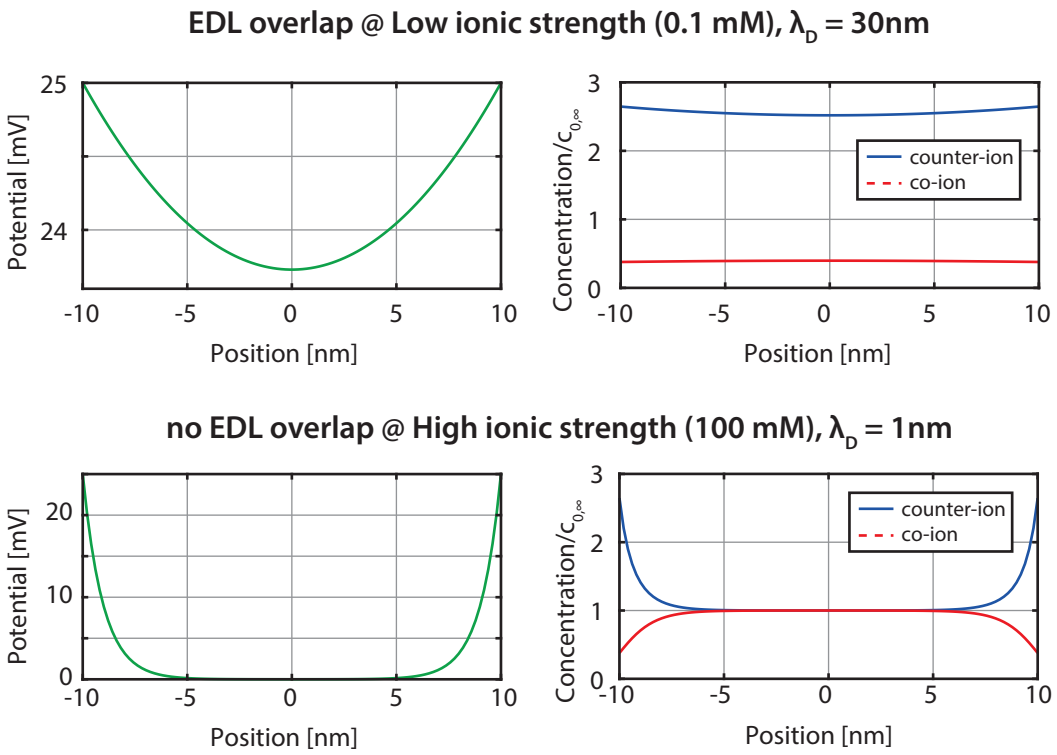

Figure 3.4 – Evolution of electrical potential (**left**), co- and counter-ion concentration (**right**) in a nanoslit with (**top**) and without (**bottom**) EDL overlap with characteristic dimension of 20 nm.

3.6 Surface potential vs. surface charge - the Grahame equation

The previous equations were derived by taking in to account a nanochannel which walls show an uniformly distributed surface charge. This is true for *passive* nanofluidic devices when the surface charge changes accordingly with the material in contact with the solvent. For example SiO_2 exhibit a negative charge while Al_2O_3 has a positive charge.[26] In *active* nanofluidic devices however the interest is to actively modulate the ionic enrichment/exclusion of the nanochannel by means of an external electrical potential. The relationship between the surface charge q_{surf} and the equivalent surface potential φ_0 is given by the Grahame equation,

$$q_{\text{surf}} = \frac{\varphi_0}{|\varphi_0|}\sqrt{2\varepsilon RT I_c \sum_i c_{i,\infty}\left[\exp\left(-\frac{z_i F\varphi_0}{RT}\right)-1\right]} \tag{3.18}$$

which for a symmetric electrolyte such as KCl simplifies to:

$$q_{\text{surf}} = \frac{\varepsilon\varphi_0}{\lambda_d}\left[\frac{2RT}{F\varphi_0}\sinh\left(\frac{F\varphi_0}{2RT}\right)\right] \tag{3.19}$$

For small values of $\varphi_0 < V_{\text{th}}$ the Debye-Hückel approximation is valid and equation 3.19 simplifies to $q_{\text{surf}} = \frac{\varepsilon\varphi_0}{\lambda_d}$. This expression can be interpreted with a parallelism with the formulation for an accumulated charge Q_{capa} inside a capacitor C at a given voltage V

$$\begin{aligned} q_{\text{surf}} &= \frac{\varepsilon}{\lambda_D} \cdot\varphi_0 \\ Q_{\text{capa}} &= C \cdot V \end{aligned} \tag{3.20}$$

Which shows how, in the Debye-Hückel approximation the EDL is interpreted as an equivalent capacitor of thickness λ_D at the interface.

Figure 3.5 shows the equivalence between surface charge q_{surf} and electrical potential φ calculated for symmetric ions by the non linear Grahame equation and with the Debye-Hückle approximation. At high ionic strengths the EDL, and therefore λ_D, is much thinner, resulting in a bigger "equivalent capacitance". It's possible to observe how for small voltages $V \in [-V_{\text{th}}, V_{\text{th}}]$ the linearization approximates well the Grahame equation, whereas for bigger values the Grahame equation is clearly under-represented when linearized. In green on the graph is shown as a reference for the reader the native charge density of $SiO_2 = -4{,}24\,\text{mC}\,\text{m}^{-2}$ at 1 mM.[25]

Figure 3.5 shows one important concept of active nanofluidic devices. The native surface charge density σ of most materials is relatively low compared to typical electrical potential used in electrochemistry, usually limited to a couple of volts above and below zero. Even at low concentrations with "large" EDL, the native surface charges of SiO_2 can be easily reproduced by applying a relatively low voltage on one electrode.

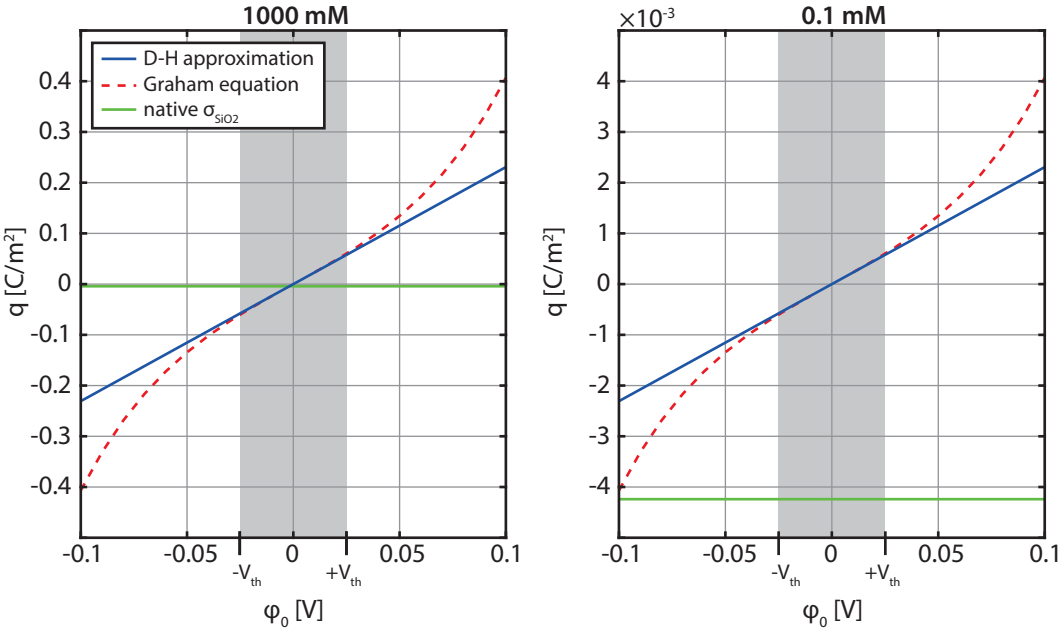

Figure 3.5 – Calculation of the equivalent surface charge in function of the surface potential φ_0 at two different electrolyte concentrations. The Debye-Huckel approximation estimates well the Grahame equation (3.19) for $\varphi_0 \in [-V_{\text{th}}, V_{\text{th}}]$. In green is represented the surface charge of SiO_2 as a reference for the reader.

3.7 Electrokinetic flows

As previously introduced in section 1.2.2, electrophoretic and electroosmotic flows are two electrokinetic phenomena that affect the motion of ions in a channel filled with an electrolyte when exposed to an external electric field.

One practical way to express both terms is to use an electrokinetic coupling matrix χ which express without ambiguity the flow of electrolyte Q and the current I according to the applied pressure p and electric field E.

$$\begin{bmatrix} Q/A \\ I/A \end{bmatrix} = \underbrace{\begin{bmatrix} \chi_{11} & \chi_{12} \\ \chi_{21} & \chi_{22} \end{bmatrix}}_{\chi} \begin{bmatrix} dp/dx \\ E \end{bmatrix} \tag{3.21}$$

3.7.1 Microchannel with thin EDL

Channel with neutral surface charge Let's consider a cylindric channel of length L, radius $r \gg \lambda_D$, and section $A = \pi r^2$ filled with an electrolyte of viscosity η having a neutral surface

to which a pressure p and an electric field E are applied. In the absence of EDL flow Q and current I are uncoupled and therefore the current is the expression of Ohm's law and the flow is determined by the hydrodynamic resistance R_h of the the channel.

$$\begin{bmatrix} Q/A \\ I/A \end{bmatrix} = \begin{bmatrix} r^2/8\eta & 0 \\ 0 & 1/\rho \end{bmatrix} \begin{bmatrix} dp/dx \\ E \end{bmatrix} \tag{3.22}$$

Where the hydraulic resistance R_h and "geometric" electrical resistances R_E of the channel are defined as

$$R_h = \frac{8\eta L}{Ar^2} \tag{3.23}$$

$$R_E = \rho \frac{L}{A} \tag{3.24}$$

Channel with net surface charge If the same microchannel with $r \gg \lambda_D$ of the previous paragraph acquires a net surface charge (as is always the case in practice) the electroosmotic and streaming potential components are included to show the influence of the electric field on the hydraulic pressure (i.e. the electroosmotic pressure) and *vice-versa*, the influence of pressure differential on the ionic current (i.e. streaming potential). Equation 3.22 becomes

$$\begin{bmatrix} Q/A \\ I/A \end{bmatrix} = \begin{bmatrix} r^2/8\eta & -\varepsilon\varphi_0/\eta \\ -\varepsilon\varphi_0/\eta & \frac{1}{\rho} + \frac{\varepsilon^2\varphi^2}{\lambda_D\eta r} \end{bmatrix} \begin{bmatrix} dp/dx \\ E \end{bmatrix} \tag{3.25}$$

where the term $\chi_{21} = \chi_{12} = -\varepsilon\varphi_0/\eta$ is commonly referred as the electroosmotic mobiliy μ_{EO} and the term $\frac{\varepsilon^2\varphi^2}{\lambda_D\eta r}$ has been added to consider the increase in conductance in the channel due to the ionic enrichment close to the walls.

3.7.2 Nanochannel with thick EDL

Equation 3.25 of the *thin-layer* solution assumes that $r \gg \lambda_D$ and there is no EDL overlap at the center of the channel, thus the double layer can be integrated to infinity as in the semi-infinite case. In the case of a cylindrical *nano*channel of length L, radius $r \leq \lambda_D$ and section A filled with an electrolyte, this assumption is not valid anymore and therefore the EDL must be integrated over a finite domain.[4, p. 338] *De facto* this adds some coefficients β_{ij} to the electrokinetic matrix, which represent the ratio of the response of the system in the case of a thick EDL over the response of the same system but in the case of vanishingly thin EDL. The electrokinetic matrix can be therefore defined as

$$\begin{bmatrix} Q/A \\ I/A \end{bmatrix} = \begin{bmatrix} \beta_{11}\, r^2/8\eta & -\beta_{12}\,\varepsilon\varphi_0/\eta \\ -\beta_{21}\,\varepsilon\varphi_0/\eta & \beta_{22}\, 1/\rho \end{bmatrix} \begin{bmatrix} dp/dx \\ E \end{bmatrix} \tag{3.26}$$

It's possible to observe how in χ_{11}, the presence of r^2 as numerator confirms that for smaller nanochannels the impact of the hydraulic pressure on the total flow Q becomes negligible while the impact of the electric field on the electroosmotic flow (factor χ_{12}) is not affected by the radius of the channel but rather by its length L, being the electric field $E = V_{\text{ext}}/L$. Furthermore the conductivity of the nanochannel, factor χ_{22}, is increased at high surface potentials and in small nanochannels, since both parameters result in a stronger ionic enrichment of the nanochannel.

3.8 Current modulation in a nanofluidic transistor

In order to evaluate the impact of the surface potential of the nanopore on its conductivity let's consider a cylindrical nanopore with radius $d/2 < \lambda_D$ and length L, with a surface potential φ_0 filled with a symmetric electrolyte with a bulk concentration of $c_{0,\infty} = 0{,}1\,\text{mM}$. The current density through an infinitesimal surface ΔS when exposed to an external electric field $\vec{E}_{\text{ext}} = V_{\text{ext}}/L$ is thus defined as the sum of the flow of each individual ionic species i flowing through the surface as

$$\vec{i} = F \sum_i c_i z_i u_i \, \Delta S \tag{3.27}$$

Where u_i is the velocity of each ionic species and F is the Faraday constant.
The current density can then be integrated in cylindrical coordinates over the section of the nanopore defined as $0 \le r \le d/2$ and $0 \le \theta \le 2\pi$ to obtain the overall current I flowing through the nanopore as

$$I = F \int_0^{2\pi} \int_0^{d/2} r \sum_i c_i z_i u_i \, dr \, d\theta \tag{3.28}$$

This equation can be developed with two assumptions: first, that in a long nanopore with $L \gg d$, the concentration profile of each ionic species can be assumed uniform along the nanochannel axis and dependent exclusively on the radius $c_i = c_i(r)$. Second, the concentration profile considers the system at stability, therefore the diffusion of the ionic species can be neglected. This way the velocity magnitude of the ionic species can be divided in two different components: the convective component resulting from the electroosmotic flow and the electrophoretic component, with $u_i = u_{\text{conv}} + u_{i,\text{EP}}$ giving

$$I = 2\pi F \int_0^{d/2} r \, u_{\text{conv}} \sum_i c_i z_i \, dr + 2\pi F \int_0^{d/2} r \sum_i c_i z_i u_{i,\text{EP}} \, dr \tag{3.29}$$

The solution for a generic electrolyte can therefore be given by considering

$$\begin{aligned} u_{\text{conv}} &= \frac{\varepsilon E_{\text{ext}}}{\eta} (\varphi_{\text{mid}} - \varphi_0) \\ u_{i,\text{EP}} &= \mu_{\text{EP},i} E_{\text{ext}} \end{aligned} \tag{3.30}$$

where φ_{mid} is the potential at the middle of the nanochannel (at $r = 0$), and $\mu_{\text{EP},i}$ is the electrophoretic mobility of the ionic species i, which return:

$$\begin{aligned} I =& 2\pi F \int_0^{d/2} r \frac{\varepsilon E_{\text{ext}}}{\eta} (\varphi_{\text{mid}} - \varphi_0) \sum_i c_i z_i \, dr \\ &+ E_{\text{ext}} 2\pi F \int_0^{d/2} r \sum_i c_i z_i \mu_{\text{EP},i} \, dr \end{aligned} \tag{3.31}$$

If a symmetric electrolyte such as KCl is considered, the equation can be further simplified by approximating $|\mu_{\text{EP}}| = \mu_{\text{EP},K^+} = -\mu_{\text{EP},Cl^-}$ and by defining the electroosmotic coefficient as $\mu_{EO} = \frac{\varepsilon \varphi_0}{\eta} E_{\text{ext}}$.

$$\begin{aligned} I =& \underbrace{2\pi F \mu_{EO} \int_0^{d/2} r \Big(\frac{\varphi_{\text{mid}} - \varphi_0}{\varphi_0} \Big) (c_{K^+} - c_{Cl^-}) \, dr}_{i_{\text{conv}}} \\ &+ \underbrace{E_{\text{ext}} |\mu_{\text{EP}}| 2\pi F \int_0^{d/2} r (c_{K^+} + c_{Cl^-}) \, dr}_{i_{\text{EP}}} \end{aligned} \tag{3.32}$$

It has to be noted that the ratio between the current in the nanofluidic channel I and the current in the "bulk" case I_{bulk} (which is in a nanofluidic channel without the ionic enrichment due to the EDL) correspond to the parameter $\beta_{22} = I / I_{\text{bulk}}$ of equation 3.26 where the bulk current can be expressed as

$$I_{\text{bulk}} = E_{\text{ext}} r^2 \pi F \sum_i \mu_{\text{EP},i} c_{i,\infty} z_i \tag{3.33}$$

3.8.1 Ideal solution - point-charge ions

The current in the nanochannel can thus be derived by estimating the concentration profile of both potassium c_{K^+} and chloride c_{Cl^-} ions by considering every ion as a point charge as in one ideal solution. The concentration profile is therefore dictated by the potential $\varphi(r)$ in the nanochannel as a function of the radius, as

$$\varphi(r) = \varphi_0 \frac{\cosh r/\lambda_D}{\cosh d/2\lambda_D} \tag{3.34}$$

$$c_{K^+}(r) = c_{0,\infty} \exp\Big(-\frac{F}{RT}\varphi(r)\Big) \tag{3.35}$$

$$c_{Cl^-}(r) = c_{0,\infty} \exp\Big(+\frac{F}{RT}\varphi(r)\Big) \tag{3.36}$$

The current I as a function of the surface potential and the concentrations c_{K^+,Cl^-} as a function of the potential distribution can thus be numerically evaluated.
As an example figure 3.6 considers a membrane with 49 cylindrical nanopores with $d = 50\,\text{nm}$

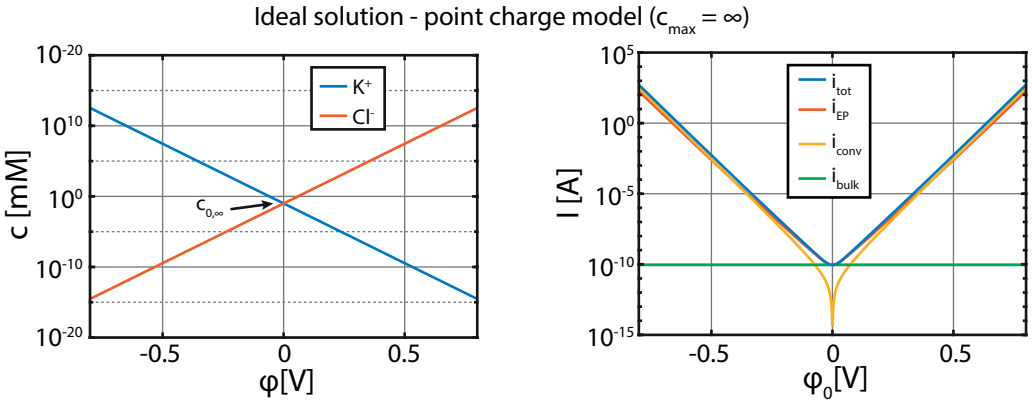

Figure 3.6 – Concentration as a function of the potential (**left**) and current modulation as a function of the nanopore surface potential (**right**) calculated with the point charge model that doesn't take in account a finite maximal ionic concentration $c_{\max}$.

and $L = 800\,\text{nm}$, with a transmembrane voltage of $V_{\text{ext}} = 0{,}5\,\text{V}$ filled with a solution of KCl 0,1 mM where the electrophoretic coefficient was derived through the Einstein relationship stating $\mu_{EP} = D_i F/RT$ where $D_i = 2{,}0 \times 10^{-9}\,\text{m}^2\,\text{s}^{-1}$ for both potassium and chloride. The dependence of the ionic concentration from the electrical potential is shown on the left, while the expected current as a function of the surface potential is presented on the right.
Because of the exponential nature of equations 3.35 and 3.36 describing the relationship between the concentration and the potential distribution, even for low voltages (±800 mV) the potential $\varphi(r)$ becomes dominant over the thermal voltage of $RT/F = 25\,\text{mV}$ (at room temperature) which results in an increase of the concentration up to 13 orders of magnitude until a theoretical concentration of $10 \times 10^{10}\,\text{M}$ of counterions at the extrema of the graph. Such high ionic concentrations leads to currents of some hundreds of amperes as shown in figure 3.6 - right.
This calculation is not realistic and derives by the hypothesis that ions can be represented as a point charge without considering any upper boundaries to the maximal concentration that can be obtained. The point charge model is therefore valid for diluted solutions but is not representative any more of the physics of the liquid for concentrated solutions.

3.8.2 Steric correction of the ideal solution

The point charge model can be improved if the ions are considered as hard spheres with a defined radius rather than point charges with an infinitesimal radius. Taking in to account the finite volume of the ions in the models inctroduces a maximum volumic concentration into which the ions can be packed, which differs from the point charge model.[4, p. 213] A maximum ion number density $n_{\max} = \lambda_{HS}^{-3}$ can be estimated by taking into account the approximate diameter λ_{HS} of an ion with its hydration shell, typically 3 Å. The maximal ionic

concentration can be therefore derived as

$$c_{i,\max} = \frac{1}{N_A \lambda_{HS}^3} \tag{3.37}$$

and the Poisson-Boltzmann model describing the relationship between the ionic concentration c_i and the potential $\varphi(r)$ can therefore be modified for a generic electrolyte as

$$c_{\mathrm{HS},i}(r) = \frac{c_{i,\infty} \exp\left(\frac{F z_i \varphi(r)}{RT}\right)}{1 + \sum_i \frac{c_{i,\infty}}{c_{i,\max}} \left[\exp\left(\frac{F z_i \varphi(r)}{RT}\right) - 1\right]} \tag{3.38}$$

Which in the case of a symmetric electrolyte as KCl can be simplified by assuming $c_{\mathrm{K}^+,\max} = c_{\mathrm{Cl}^-,\max} = c_{\max}$ as

$$c_{\mathrm{HS},i}(r) = \frac{c_\infty \exp\left(\frac{F\varphi(r)}{RT}\right)}{1 + 2\Lambda \sinh^2\left(-\frac{F\varphi(r)}{2RT}\right)} \tag{3.39}$$

where Λ is a packing parameter defined as $\Lambda = 2c_\infty / c_{\max} = 2N_A c_\infty \lambda_{HS}^3$.
For a solution of KCl at 0,1 mM which ions exhibit an hydration shell of 3 Å it corresponds to $\Lambda = 3{,}2520 \times 10^{-6}$. Small potentials φ or small values of Λ make the denominator ≈ 1 and therefore the hard sphere model tend to the point charge model since the ionic crowding is not present. Large values of Λ deriving either from big ions or from the presence of large potentials on the other hand results in the denominator to become dominant and the concentration thus tends to $c_{\max}$.

Figure 3.7 show a comparison between the ionic concentration profiles calculated with the point charge model (on the left) and the hard sphere model (on the right) along the diameter of one nanochannel of 50 nm filled with KCl 0,1 mM at three different applied surface potentials, $\varphi_0 = [0.1, 0.4, 0.8]$V. It's possible to observe how for small voltages ($\varphi_0 = 0{,}1$ V) both profiles are identical, whereas at higher voltages the effect of the ionic crowding starts to appear in the hard sphere model, first close to the borders where the electrical field is higher (at $\varphi_0 = 0{,}4$ V), then on the whole diameter for larger values of the surface potential. (at $\varphi_0 = 0{,}8$ V).

The conductivity of the nanochannels can be then evaluated by considering the concentration

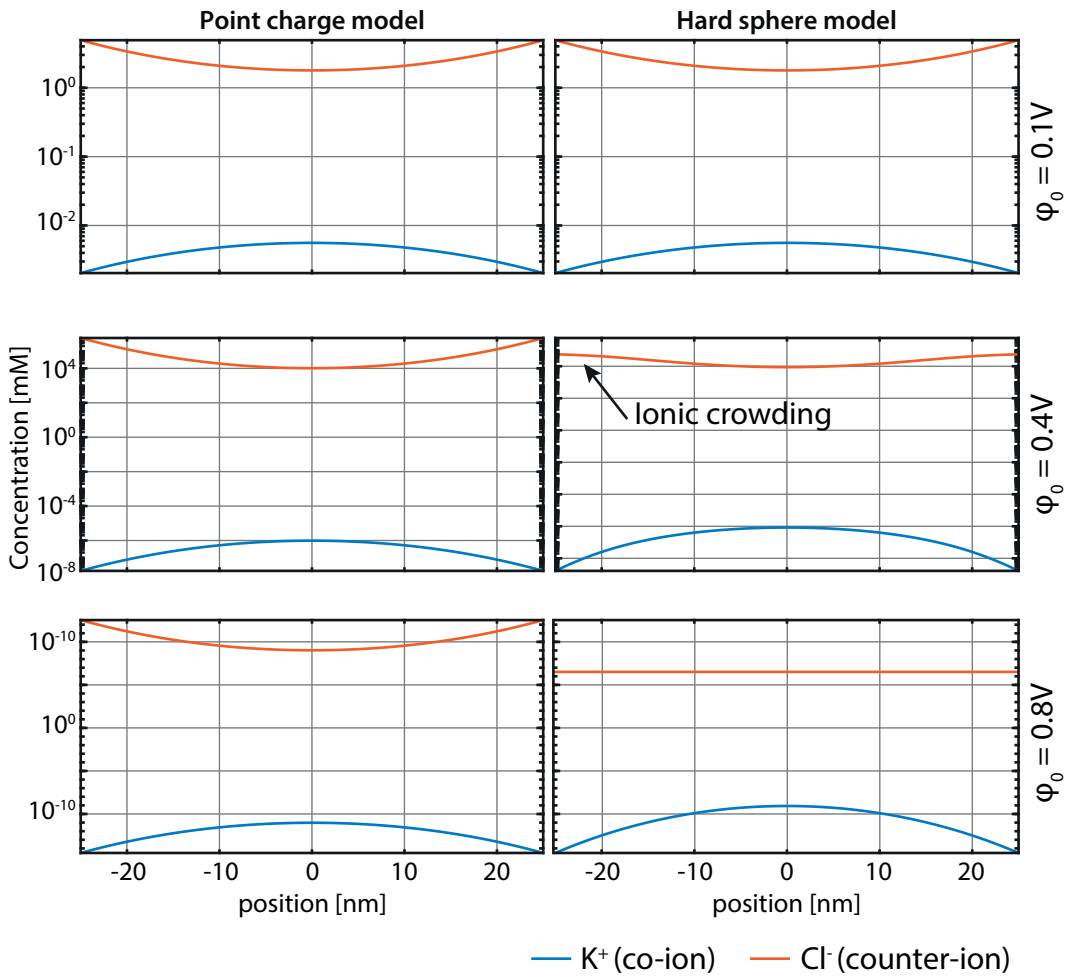

Figure 3.7 – Comparison between the ionic concentrations on a nanochannel of 50 nm calculated through the point charge model (**left**) and the hard sphere model (**right**) at three different surface potentials φ_0.

profile with the hard-sphere correction rather than the point charge giving

$$I = \underbrace{2\pi F \mu_{EO} \int_0^{d/2} r\left(\frac{\varphi_{\text{mid}} - \varphi_0}{\varphi_0}\right)(c_{\text{HS},K^+} - c_{\text{HS},Cl^-})\, dr}_{i_{\text{conv}}} + \underbrace{E_{\text{ext}}|\mu_{EP}|2\pi F \int_0^{d/2} r\,(c_{\text{HS},K^+} + c_{\text{HS},Cl^-})\, dr}_{i_{\text{EP}}} \tag{3.40}$$

Figure 3.8 shows the ionic concentrations (left) and current (center) as a function of the surface potential as calculated with the hard sphere correction of equation 3.40 in the same conditions previously used for the point charge model in section 3.8.1. The maximal concentration is now limited to c_{max} by physically meaningful values as it is possible to observe in the left graph.

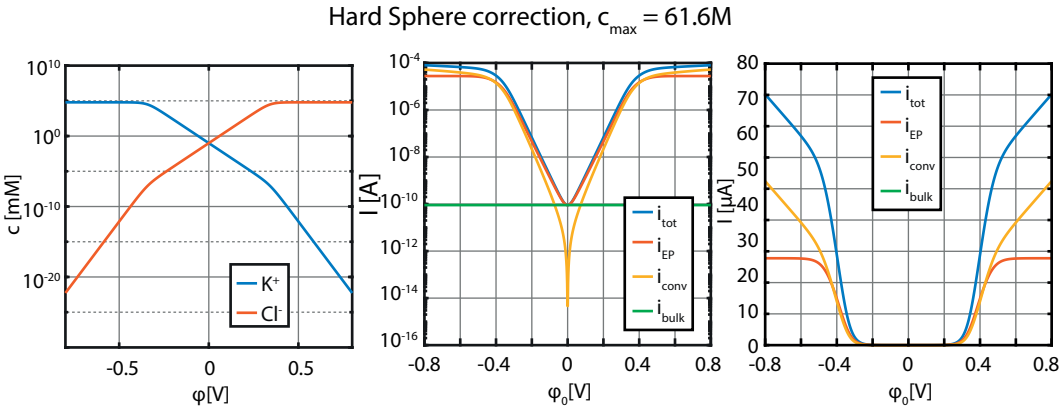

Figure 3.8 – Ionic concentration as a function of the potential (**left**) and current modulation as a function of the nanopore surface potential(**center** and **right**) calculated through the hard sphere model, with a maximal ionic concentration of $c_{\max} = 61{,}6\,\mathrm{M}$.

At voltages greater than 0,5 V the number of ions inside the channel is limited by the ionic crowding which saturates *de facto* the contribution of the electrophoretic current to a total current in the nanochannel.
Figure 3.8-right shows the current modulation as a function of the surface potential calculated with the hard sphere correction (exactly as figure 3.8-center) but plotted on a linear axis. It becomes now evident how the electrophoretic current i_{EP} is limited for $\varphi_0 > |0{,}5\,\mathrm{V}|$ and in this regime of saturation the convective contribution to the total current becomes dominant.

3.8.3 Discussion

The inclusion of the hard sphere correction in the model provides a meaningful upper boundary which limits the current density at high potentials, and results in a modulation of the transmembrane current of 6 orders of magnitudes. However, the maximal concentration calculated for KCl through the typical diameter of hydrated ions (3 Å leads to a maximal *"crowded"* ionic concentration of 61,1 M. This value is not reasonable when compared with pure water maximal concentration of $55{,}5\,\mathrm{mol\,L^{-1}}$ and with KCl solubility limit in water of $3{,}4\,\mathrm{mol\,L^{-1}}$(25.39wt% at 20 °C [114]). Furthermore, the maximal solubility of KCl in wafer consider the presence of both K and Cl ions whereas if only one of the two ions is present and the other one is excluded such as in the "crowded" case, is reasonable to expect a lower solubility because of the greater repulsive interaction between ions.
Figure 3.9 shows the concentration and modulation as a function of the surface potential if a maximal concentration of 1,6 M is considered, the half of the saturation value for KCl corresponding to $\lambda_{\mathrm{HS}} = 10\,\text{Å}$. In this case the modulation of the transmembrane current is lower (of 4 orders of magnitudes with $\lambda_{\mathrm{HS}} = 10\,\text{Å}$ compared to the previous 6 orders of magnitude with $\lambda_{\mathrm{HS}} = 3\,\text{Å}$) and the potential necessary to saturate the transmembrane current is lower

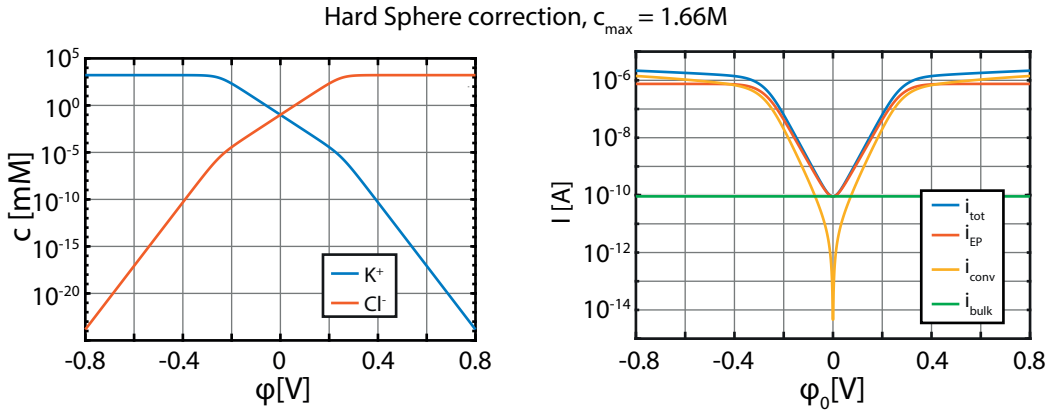

Figure 3.9 – Ionic concentration as a function of the potential (**left**) and current modulation as a function of the nanopore surface potential (**right**) calculated through the hard sphere model, with a maximal ionic concentration of $c_{\max} = 1{,}6\,\mathrm{M}$.

too (0,3 V compared to 0,5 V). Nevertheless, even in this worst case scenario, the potential for the control of ionic flow through direct control of the surface potential of the nanopore remains huge and vastly unexplored, considered that in practice typical modulations of the transmembrane current were demonstrated to be typically in the order of 0,5.

3.9 Conclusions

This short overview showed the basic phenomena that governs the movement of liquids inside a nanochannel. First the origins of the surface charge and its dependency from the pH was discussed, then the structure of the EDL was described and an interpretation was given through a comparison between the common Debye-Hückel approximation and the non-linear Poisson-Boltzmann equation. Such comparison highlighted how integrating electrodes and active nanofluidic devices allows to achieve relatively higher surface charge densities compared to native surface charges proper of passive devices. Finally electroosmosis and electrophoresis were quickly reviewed and their contribution to the current modulation evaluated.

4 Nanofluidic transistor with polarizable gate

In this chapter is shown a solid-state nanofluidic transistor membrane with electrostatically gated nanopores made of amorphous carbon, a polarizable material. The use of a polarizable material at the nanopore-electrolyte interface avoids covering the gate electrode with a dielectric insulation, which potentially leads to more efficient and more sensitive devices. The fabricated membranes have nanopores with critical dimensions ranging from 30 nm *to* 70 nm *obtained through molding of sacrificial silicon templates presented in chapter 2. The membranes were used to demonstrate the ability to modulate the transmembrane ionic conductivity via the variation of the surface charge of the nanochannels with low voltages (*800 mV*) and modulation factors close to 100%. This chapter is based on a publication under review at the date of submission of this thesis.*

Nanofluidic devices able to control the flow of charged molecules with single-molecule precision, as electrical circuits control the flow of electrons, hold the promise for new applications in the fields of energy production, nano-medicine, filtration science, and analysis of biological and chemical samples.[18], [51], [70], [74].

4.1 Motivation

Altough the state of research of smart gating solid-state nanoporous membranes is still in its early stages, three main working principles can be identified[75]: the first principle consist in modulating the properties of the nanochannel, and expecially its surface charge, to modulate the diffusive flow, the EOF and EP through the nanopores. Secondary, one can actively modify the wettability of of the nanopore to physically break the continuity of the solution from one

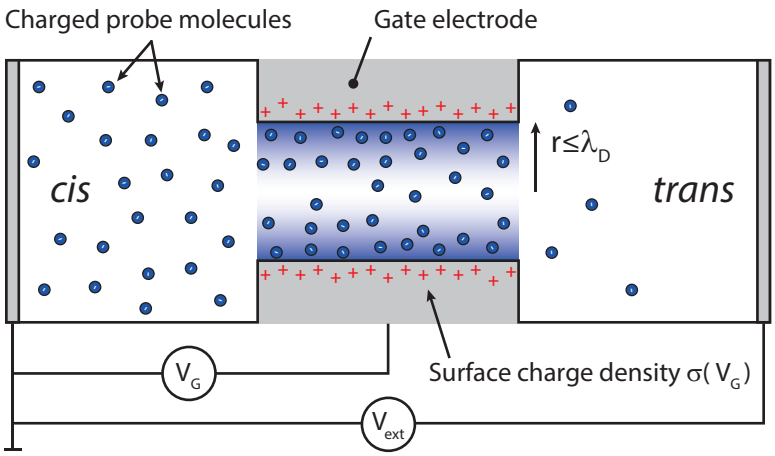

Figure 4.1 – Schematics of a voltage gated nanofluidic transistor with radius $r \ll \lambda_D$. The flow of a charged probe molecule is controlled through an external voltage V_{ext} applied through two external electrodes, and the surface charge σ imposed through a gate electrode of potential φ.

side to the other of the nanochannel. Third, one can deposit a stimuli responsive material on the membrane in order to combine its properties to the ones of the underlying membrane.

Electrostatically gated nanofluidic transistors fall in the first category and were previously introduced in section 1.3.1. They consist in nanochannels with an additional electrode integrated *on* the channel, the *gate electrode*, meant to modulate the ionic permeability of the channel through its electric potential (*i.e.* the surface charge). There are three ways in which the flow of charged molecules through a nanochannel can be electrostatically controlled, which corresponds to the three terms of the Nernst-Planck equation: diffusive, electrokinetic and convective (equation 3.5 on page 45).

4.1.1 Case study

To qualitatively describe how those three flows respond to different voltages let's consider a nanofluidic transistor with a circular nanochannel of radius $r \leq \lambda_D$ (i.e. with EDL overlap) and connecting two reservoirs both filled with the same electrolyte (figure 4.1). The *cis*-reservoir is filled with a charged probe molecule, such as a protein (typically negatively charged), which flow across the nanochannel toward the *trans*-reservoir is controlled *via* three electrodes: one gate electrode which potential V_G is used to modify the surface potential σ of the nanochannels as described by the Grahame equation 3.19; and two electrodes at the extremities of the nanochannel used to modify the electrochemical potential of the reservoirs *via* an external voltage V_{ext}. As a reference the electrode in the *cis*- reservoir represents a reference voltage $V = 0$.

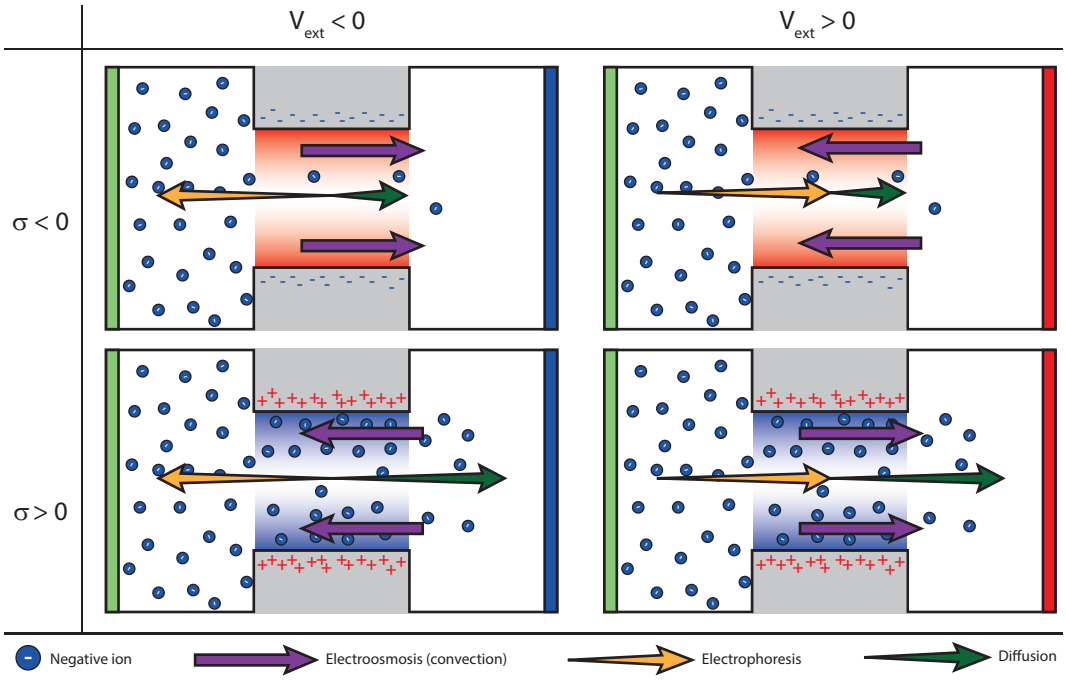

Figure 4.2 – Diffusive, electrophoretic and electroosmotic flows in a nanofluidic transistor in function of the surface potential φ_0 and the external voltage V_{ext}

Figure 4.2 describes the case study corresponding to the four different combinations of external voltages $\pm V_{\text{ext}}$ and gate potential $\pm V_G$. As previously said, three types of flow phenomena govern the total flow of the charged probe molecule across the channel: the diffusive, the electrophoretic and the electroosmotic flow.
The diffusive flow is dictated by the term $\nabla \cdot D_i \nabla c_i$ of the Nernst-Planck equation and has always the same direction from the *cis*- toward the *trans*-reservoir, as the concentration gradient is the same in the four cases. However the diffusive flow is larger in the two bottom cases, when $\sigma > 0$ and the nanochannel is enriched in counter-ions due to EDL overlap.
The electrophoretic flow on the other hand depends exclusively on V_{ext} and therefore can be modulated with an external potential. The electrophoretic flow of the probe molecules will therefore be in the same direction of the diffusive flow for $V_{\text{ext}} > 0$ (figure 4.2 - right) or opposed to the diffusive flow for $V_{\text{ext}} < 0$ (figure 4.2 - left).
In the absence of an external pressure the convective flow corresponds to the electroosmotic flow (EOF) which is uniquely dependent from the channel surface charge and from the applied external potential. The EOF is opposed to the diffusive flow when surface charge and external potential have the same polarity ($V_{\text{ext}} \cdot \sigma > 0$) and is opposed to the diffusive flow when they have opposite polarity ($V_{\text{ext}} \cdot \sigma < 0$).
To control the flow of molecules through a nanochannel one must be able to set a phase ON or *open*, where the molecules flow across the channel, from the *cis* to the *trans* reservoir, and a phase OFF or *close*, when the flow of molecules is interrupted or reduced. Figure 4.2 shows how with this configuration the ON phase is possible to obtain with $\sigma > 0$, $V_{\text{ext}} > 0$ where the

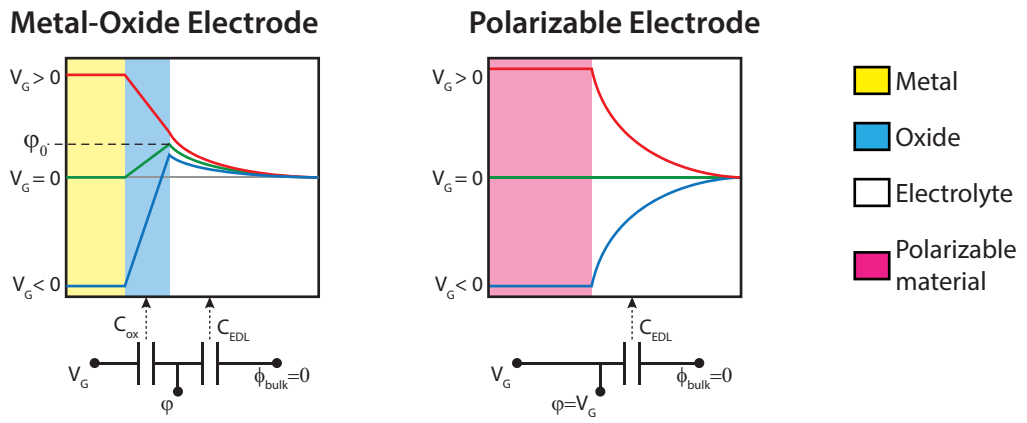

Figure 4.3 – Metal-Oxide electrode vs. Polarizable electrode

three components of the flow are in the same *cis-trans* direction across the nanochannel. On the other hand, phase OFF is more difficult to obtain since in any of the presented cases the three flows retain the molecules from crossing the channel.
In the case where the surface charge of the nanochannel has the same polarity of the charged probe molecule ($\sigma < 0$) the EOF and EP are in both cases opposed to each other which is detrimental if the objective is to stop the flow. On the other hand, the case where the EOF and the EP are opposed to the diffusive flow is for $\sigma > 0$, $V_{\text{ext}} < 0$ for which the diffusive flow is maximum. In this case the diffusive flow is dominant especially in the ideal case when the *cis* reservoir is uniformly filled with the charged probe molecule and the *trans* reservoir is empty and the gradient of concentration is maximum.

Let's compare a passive nanochannels, characterized by one *fixed* surface charge dependent either by the material used or by a functionalization of the nanochannel, with a nanofluidic transistor.
With a passive nanochannels one must choose a given surface charge, then control the flow with an external voltage. In figure 4.2 this corresponds to switching either between the two cases at the top, when nanochannel walls and the molecules have the same polarity, or between the two cases at the bottom, for which the nanochannel has opposite polarity of the molecule.
Nanofluidic transistors on the other hand, provide the capability to inverse the surface charge of the nanochannel, allowing to switch "vertically" and "horizontally" between cases in figure 4.2 since they allow to actively control both the surface potential of the nanochannel as well as the external voltage.

4.2 Polarizable electrode

Active nanofluidic devices as well as FET rely on the same principle of a gate electrode which modulates the charge carrier density of a region connecting two reservoirs. This require the gate electrode to be electrically insulated from the channel underneath in a typical metal-oxide

configuration.

Limitations of metal-oxide gates The addition of this insulating layer however attenuate the influence of the gate voltage V_G on the surface charge density at the electrolyte-nanopore interface. The oxide layer behaves like a capacitor C_{ox} in series with the capacitance of the EDL C_{EDL} and results in a capacitive voltage divider (figure 4.3 - left). Since the two capacitors have the same area A we can express the equivalent circuit of a metal-oxide electrode as

$$\varphi = V_G \frac{C_{\text{ox}}}{C_{\text{ox}} + C_{\text{EDL}}} = V_G \frac{\varepsilon_{SiO_2} / t_{SiO_2}}{\varepsilon_{SiO_2} / t_{SiO_2} + \varepsilon_{H_2O} / \lambda_D} \tag{4.1}$$

where ε_{H_2O} and ε_{SiO_2} are the relative permittivity of water and silicon dioxide, respectively. The C_{EDL} is defined by the thickness of the EDL which is typically in the range of 1 nm to 100 nm. In order to maximize φ a big value of C_{ox} is desired, which can be achieved by using thin oxides t_{SiO_2} (some tenth of nanometers).
In semiconductor FET the insulating material has been optimized through the years by reducing the defect density of the oxides and by increasing their breakdown voltage, leading to actual materials which are vitually flawless, with high breakdown voltages and can be as thin as 2,3 nm.[115]
In the case of the nanofluidic transistor, being in a liquid environment, even the slightest defect or pinhole in contact with the electrolyte easily creates short-circuits from the gate to the electrolyte. Consequently, to limit gate current leakages, thick oxides are often used (up to 2 µm)[30], dramatically reducing the oxide capacitance. The small value of C_{ox} compared to C_{EDL} in nanofluidic transistors is even more evident when considered that the relative permittivity of SiO_2 typically used as insulator, is 20 times smaller than the relative permittivity of H_2O ($\varepsilon_{SiO_2} = 3.8$ and $\varepsilon_{H_2O} = 80$).[3, p. 65]
Besides greatly increasing (up to hundred volts) the voltage needed to obtain some tens of millivolts of variation at the nanochannel-electrolyte interface, the presence of a native surface charge at the dieletric surface makes the inversion of the surface charge practically impossible, since the gate voltage necessary to inverse the surface charge would overcome the breakdown voltage of the dielectric.

The interest of using polarizable electrodes This limitation can be overcome by using polarizable electrodes instead of metal-oxide electrodes.[111] Polarizable electrodes are characterized by a polarizability window in the order of ± 1 V, where no electrochemical reaction with the electrolyte is possible and therefore the interface resistance is practically infinite. Polarizable electrodes, not being damped by the C_{ox}, directly apply the external voltage at the electrode-electrolyte interface and therefore $V_G = \varphi_0$ can be assumed as shown in figure 4.3-right. Typically this type of electrodes are made of boron-doped diamond, highly oriented pyrolytic graphene (HOPG), glassy carbon or other flavours of carbon. The use of such materials at the nanopore-electrolyte interface removes the need for a dielectric, thus reducing

the voltage needed at the gate. Furthermore, since the surface charge is directly proportional to the voltage applied, it becomes possible to inverse the surface charge of the electrode and therefore of the nanopore.
This ability would be extremely useful since simulations[116] have shown that to obtain an important ON/OFF ratio is very difficult relying solely on the exclusion/enrichment effect and therefore on the *diffusive* ionic flow. Even for small nanochannels of 20 nm at low ionic strenght (1×10^{-1} mM) where the EDL overlap is important, the presence of the native charge of the electrolyte allows a maximal ON/OFF ratio smaller than 10, while in the same condition with an electrode without native surface charge (and therefore inversable) the ON/OFF ratio would be of 1×10^{4}.

In this chapter is therefore presented a nanoporous membrane with electrostatically gated nanopores made of a polarizable material, a-C:N:H, allowing to avoid using the gate-oxide insulation. The integration of a polarizable gate electrode in the nanochannel allows to directly control the surface charge without having to insulate the gate electrode from the bulk, thus resulting in a greater sensitivity of the membrane conductance to the gate voltage. The fabrication of nanoporous membranes with polarizable gates is made possible by the conformal material deposition on high aspect-ratio templates presented in chapter 2.

4.3 Choice of polarizable material

In electrochemistry, and more specifically in electrochemical sensing, the interest in polarizable electrodes comes from the fact that they present very small or negligible interaction with aqueous electrolyte within the polarization window. Practically this translates in low detection limits since any readout stems from the analyte reacting with the electrode and not from a background signal from an interaction between the solvent and the electrode. In other terms, a polarizable electrode has very little background signal and therefore a high signal-to-noise ratio and high sensitivity.

Pure diamonds are well known for their extreme hardness and thermal conductivity but are not a candidate for electrochemical electrodes since they present a wide bandgap (5,47 eV at 300 K). Diamonds however, being a semiconductor, can be doped with Boron, which provide charge carriers for electrochemical reactions. Electrochemical electrodes known as boron doped diamond (BDD) demonstrate outstanding electrochemical properties such as the largest polarizability window, almost 5 V, low capacitance and low background current, resistance to corrosion and pressure in harsh environment, biocompatibility and resistance to biofouling.[117]–[121]
Given those favourable properties, BDD would be the perfect candidate for a polarizable gate electrode. However, since thermodynamically the spontaneous transformation of graphite to diamond isn't possible at pressures lower than 15 000 atmospheres at ambient temperature,

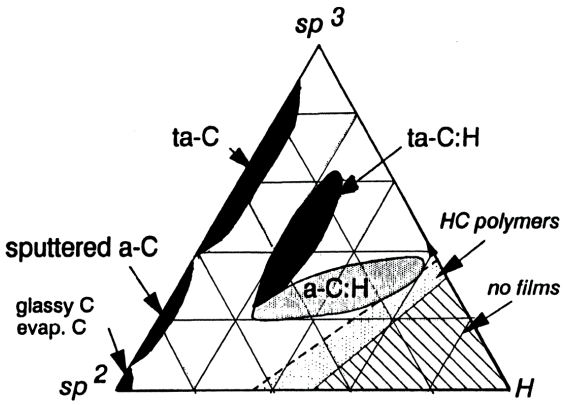

Figure 4.4 – Nomemclature of different types of carbon depending on their atomic structure and nature of their atomic hybridization. Source:A. Grill, "Diamond-like carbon: state of the art" Diam. Relat. Mater., vol. 8, no. 2–5, pp. 428–434, 1999[124].

deposition or growth of BDD in thin films is a technically challenging process that cannot be achieved with standard physical vapor deposition (PVD) or CVD cleanroom equipment. However, other carbon electrodes such as diamond-like carbon (DLC) or highly oriented pyrolytic graphene (HOPG), made of a different combinations of sp, sp^2 and sp^3 bonds (figure 4.4), were reported to present a wide polarizability window and attractive electrochemical properties. Even though they don't possess the outstanding properties of BDD electrodes, those types of carbon can be easily deposited in thin films through standard cleanroom equipment and were therefore investigated as candidates to be used as polarizable gate. [108], [109], [122]–[126]

4.3.1 Amorphous carbon as candidate for polarizable electrodes

Three different types of carbon films were tested as candidate material for the polarizable gate:

- DLC film deposited through CVD but in a RIE reactor (here named DLC-RIE), following the recipe given by Oxford, the manufacturer of the RIE-reactor.
- DLC thin film deposited through CVD in a DRIE reactor typically dedicated solely to the etch of silicon (here named DLC-AMS), following a recipe developed by two users of the machine, Dr. Cyrille Hibert and Dr. Michael Zervas.
- hydrogenated amorphous carbon–nitrogen (a-C:N:H) deposited through PECVD following the guidelines published in a paper by Kyziol and coworkers.[100].

The peculiar electrochemical properties of different types of carbon electrodes stems mostly from the types of bonds in their atomic lattice, sp^3 for BDD and sp^2 for graphene or HOPG. The test described in the following lines were done to investigate if, by changing the parameters of PECVD deposition, or by using different deposition techniques we had available in the laboratory, it was possible to obtain a type of carbon film with wide polarizability window

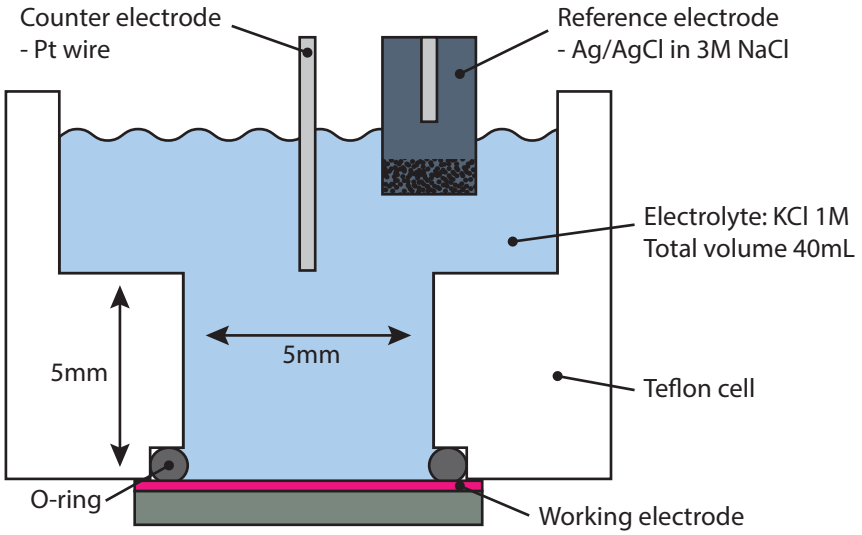

Figure 4.5 – Schematics of the cross section of the electrochemical cell used to test different types of amorphous carbon through cyclic voltammetry.

similar to the one of BDD electrodes.

Variables tested For a-C:N:H the gas proportion and flow rates suggested from Kyziol and coworkers were used.[100] Temperature plays an important role in the deposition rate (the lower the temperature, the faster the deposition). As the chuck of the CVD reactor used is not cooled, the lowest temperature that can be maintained during the 30 min necessary for the deposition was used, corresponding to 45 °C. The variables tested were the pressure of the plasma during deposition and the radio frequency (RF) power of the antenna generating the plasma.
The DLC-RIE was deposited following the recipe given by Oxford, the manufacturer of the reactor, at the CSEM in Neuchâtel. Following the experience of the operator we tried different pressures and powers while not modifying the gas flows.
DLC-AMS was deposited in a inductively coupled plasma reactive ion etching (ICP-RIE) reactor based on the recipe developed by Dr. Cyrille Hibert from the EPFL Center of MicroNanoTechnology (CMi) and Dr. Michael Zervas from EPFL. In this case the pressure was not modified and was chosen as the lowest possible. Different powers of both the coil and plate of the reactor were tested with both RF and low frequency (LF) (with cycles of 25 ms ON and 75 ms OFF) configurations of the generator.

Evaluation of materials The thin films were all deposited on 100 mm silicon wafers and tested through cyclic voltammetry, with a three-electrode configuration, in an electrochemical cell built on purpose (figure 4.5).
To control the cyclic voltammetry and to record data a potentiostat from Autolab was used with one Pt wire as counter electrode and one Ag/AgCl electrode in 3 M NaCl as reference. The

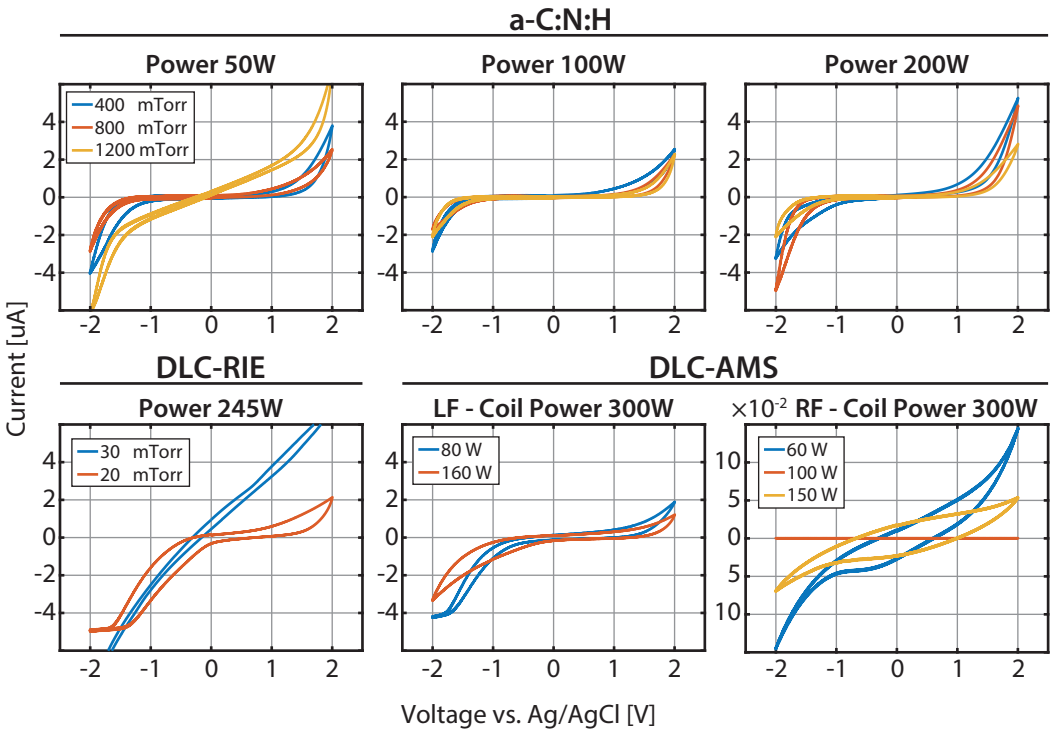

Figure 4.6 – Cyclic voltammetry of a-C:N:H, DLC-RIE and DLC-AMS. The scan rate used was 100 mVs^{-1}.

sweep speed was 100 mVs^{-1} in order to be able to compare our results with the ones reported in the literature.

Other than the electrochemical properties of the electrodes, it is important that the material of choice is compatible with the rest of the microfabrication process. Therefore the stress of the deposited films was measured since a highly stressed material would be detrimental for a suspended structure as a nanoporous membrane.

4.3.2 Results

The different combinations tried and the measurements of stress and thickness are shown in in table 4.1 whereas the a selection of results for the cyclic voltammetry is presented in figure 4.6.

The best trade-off between low leakage currents and wide polarizability window was shown by the **a-C:N:H films**. At 50 W of generator power, the wider polarizability window and currents were obtained with a pressure of 800 mtorr. With a power of 100 W we could not observe a significant difference between the I-V curves, regardless of the deposition pression, while at 200 W the current flowing through the interface is larger than at 50 W, expecially for negative voltages corresponding to the evolution of hydrogen. Given the similarity between the film obtained with 50 W/800 mtorr and the films deposited at 100 W, the sample 50 W/800 mtorr was chosen given the lower stress of the thin film measured.

	a-C:N:H	DLC-AMS	DLC-RIE
Deposition time	30 min	5 min	5 min
Reactor	CVD - Oxford Plasmalab System 100	DRIE - Alcatel AMS 200	RIE - Oxford Plasmalab system 80+
Temperature	45 °C	20 °C	None
Gas mixture	Ar:75 sccm, CH_4:10 sccm, N_2:84 sccm	CH_4:50 sccm	CH_4:50 sccm

	Pressure mtorr	Coil Power W	Plate Power W	Generator	Thickness nm	Stress MPa
a-C:N:H	400	50		RF	115,9	−41,4
	800	50		RF	247,5	−23,2
	1200	50		RF	287,6	−20,9
	400	100		RF	113,5	−52,8
	800	100		RF	265,5	−32,0
	1200	100		RF	265,7	−30,5
	400	200		RF	251,3	−29,8
	800	200		RF	245,4	−15,4
	1200	200		RF	359,2	−35,9
DLC-AMS	8	300	60	RF	106,9	−2883,1
	8	300	100	RF	111,4	−2350,2
	8	300	150	RF	121,1	−1899,8
	8	1500	60	RF	281,6	−1354,3
	8	1500	100	RF	267,7	−889,3
	8	1500	150	RF	-	-
	8	300	80	LF	86,5	−657,7
	8	300	160	LF	85,8	−609,9
	8	1500	80	LF	123,1	−370,5
	8	1500	160	LF	95,4	−1087,2
DLC-RIE	30	245		RF	89,4	−1375,8
	20	245		RF	79,2	−1182,9
	20	340		RF	76,8	−1154,6
	30	340		RF	90,9	−1206,9

Table 4.1 – Results for amorphous carbon and DLC electrodes.

The films made of **DLC-RIE** always demonstrated a significant asymmetry of the I-V plot toward negative values, independently from pressures and power of deposition. This electrochemical characteristic, combined with their high stress make those films not suited to be used as polarizable electrode.
DLC-AMS was tested with both RF and LF configurations of the generator. In LF configuration, the shape of the I-V plots is very similar to the DLC-RIE, with a higher current injection for negative voltages. During discussions with Dr. Zervas and Dr. Hibert who developed the recipe, was suggested that this was due to the LF pulsed bombardment of the substrate by the CH_4 plasma, a configuration similar to the one of the RIE reactor.
The deposition in RF configuration on the other hand, resulted in highly insulating films, which are not adequate for electrochemistry. A comparison between the I-V curves for a-C:N:H samples and the ones for DLC-AMS in the RF configuration shows how for voltages higher than ±1,5 V, the a-C:N:H films start to see an important charge injection symptom of hydrogen or oxygen evolution proper of an electrochemical active electrode. This marked transition between a highly resistive plateau in the polarizability window, and hydrogen/oxygen evolution at higher voltages is not visible with the DLC-AMS films. Furthermore both DLC layers have shown a high stress, 3 orders of magnitude greater than the a-C:N:H films.

4.4 Fabrication of nanoporous membranes

The fabrication of nanoporous membranes integrating polarizable a-C:N:H gate electrodes is possible by using the fabrication method presented in section 2.4 based on conformal coating of sacrificial templates. Since the a-C:N:H layer is meant to be electrically connected to an external electrical potential the approach previously presented was slightly modified by using silicon-on-insulator (SOI) wafers for the fabrication and by adding an insulating Polyimide (PI) layer on the top of the membrane. The purpose of both the buried oxide (BOx) and the PI layers is to electrically insulate the a-C:N:H and prevent leakage of current through the thick silicon backside of the chip, or through pinholes/defects of the topmost SiO_2 layer.

On a SOI wafer (BOx: 1 µm, device: 1 µm), sacrificial silicon nanotemplates were obtained through EBL followed by DRIE (figure 4.7.a). The templates determine the final geometry of the nanopores and in this case two different shapes were used: wavy and cylindrical. Elongated and wavy templates exhibit greater stability and allow to obtain smaller critical dimensions, down to 30 nm, whereas cylindrical templates are less stable and easily collapse at critical dimensions smaller than 50 nm as previously discussed in section 2.2. An important difference with the SOI wafer compared to the bulk Si structures previously presented is that on SOI wafers the templates could not be etched completely until the BOx. Previous experiments demonstrated that is necessary to leave a thin layer of Si in the range of 100 nm between the templates and the BOx to ensure the necessary mechanical stability to the templates. This suggest that the continuity of the crystalline structure between the templates and their base plays an important role in the stability of the structures

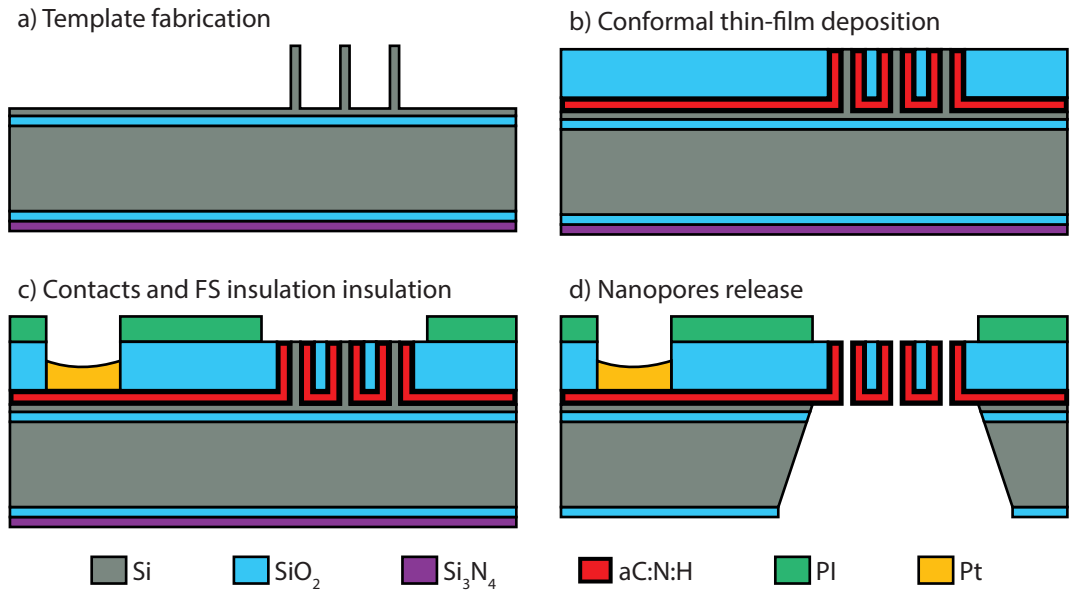

Figure 4.7 – Graphical representation of the process flow to fabricate a nanofluidic transistor. a) First the nanopore templates are etched in the device layer of a SOI wafer. b) Second, the membrane materials a-C:N:H and SiO_2 are deposited on the templates and planarized. c) The Pt external contact for the gating electrode as well as the PI insulation are structured. d) Finally the nanopores are released through a combination of KOH and HF wet etch and XeF_2 pulsed gas etch. The final geometry of the nanopore is the negative of the silicon template.

Two layers, 250 nm of a-C:N:H and 2 µm of SiO_2 were then deposited on the nanotemplates and planarized until the silicon nanopillars surfaced from the surrounding material (figure 4.7.b). Platinum contacts were then deposited on the a-C:N:H layer and an electrical insulation made of a 5 µm of PI was structured to cover the whole chip but the area of the membranes (figure 4.7.c). Finally the membranes were released through a KOH backside etch stopped on the BOx layer, an HF dip to remove the BOx and finally a short XeF_2 pulsed etch releasing finally the nanopores (figure 4.7.d). The fabrication details are given in annex A.

4.5 Measurements

4.5.1 Setup description

To measure the modulation of the conductivity of the nanochannel as a function of the membrane voltage, the chip was tested in a setup able to apply an electrical potential difference across the membrane through two external Ag/AgCl electrodes, independently modulate the surface charge of the nanopores through a gate electrode, and simultaneously measure the currents flowing in and out of the system on all three electrodes. As shown in figure 4.8.a the gate voltage V_G and current i_G correspond to the potential and current of the a-C:N:H gate electrode that modulates the surface charge of the nanopores. The electrode that controls the current across the membrane is referred to as the “source” electrode and its voltage and

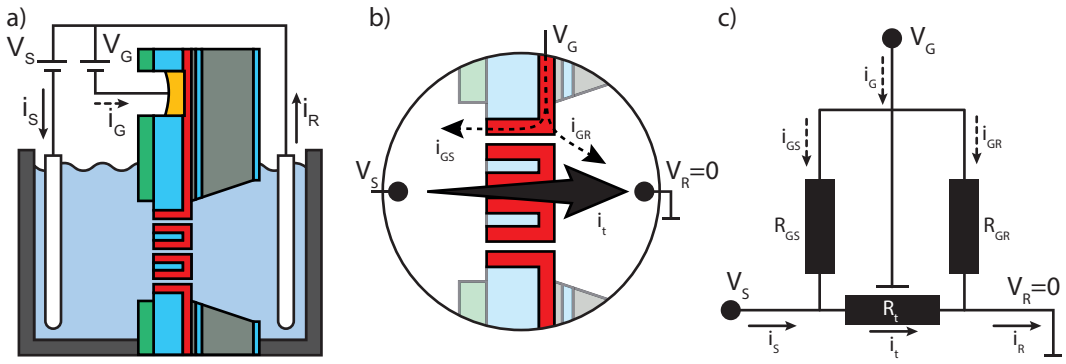

Figure 4.8 – a) Diagram of the setup used to measure the modulation of the transmembrane current. b) Detail of the gate electrode highlighting the leakages from the gate to the source and to the gate (i_{GS} and i_{GR} respectively). c) Equivalent circuit of the setup. The resistances R_{GS} and R_{GR} are added to model the leakages from the gate and are supposed to be infinite in ideal conditions.

current are noted V_S and i_S respectively. The source and gate voltages are expressed with respect to a third electrode referred to as "reference electrode" whose current and voltage are named i_R and V_R respectively. The voltage V_R of the reference electrode is zero by definition and its current i_R corresponds to the sum of the currents from the two others electrodes.
Since the membrane is asymmetric, with the KOH pyramid present only on one side of the chip and with the a-C:N:H electrode with greater surface toward the backside of the wafer, it is important to maintain a coherent terminology when referring to the transmembrane electrodes. Therefore the source electrode is by convention placed opposite from the KOH pyramid of the chip whereas the reference electrode defines the electrode placed on the same side of the KOH pyramid.
The transmembrane conductivity was measured at different fixed values of the gate voltage by applying a cyclic staircase voltage profile at the source electrode, for voltages ranging from $V_G = \pm 0{,}8\,\mathrm{V}$ and $V_S = \pm 0{,}5\,\mathrm{V}$. The measure was done with a semiconductor analyzer (Agilent 4156C) in grounded faraday cage and at each voltage step a stabilization time of 45 s was spent before measurement to limit the contribution of faradaic currents.

4.5.2 Gate leakages and equivalent circuit

Preliminary measurements have shown that, contrary to semiconductor FET, the current I_g leaking from the gate electrode is not negligible but is of the same order of magnitude as the transmembrane currents measured (see figure 4.8.b and figure 4.9). The direct consequence of such leakage is that it is not possible to *directly* measure the modulation of transmembrane current in function of the gate voltage, since the variation observed on the transmembrane electrodes is the sum of both the variation of the transmembrane current and the leakages from the gate as shown in figure 4.8.b. The leakage currents from the gate can thus be represented with an equivalent circuit shown in figure 4.8.c which takes into account the transmembrane resistance $R_t(V_G)$ and the contributions of the leakages from the gate to the source $R_{GS}(\Delta V_{GS})$

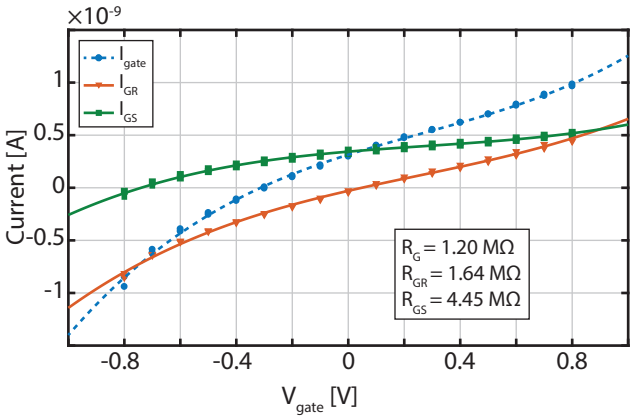

Figure 4.9 – Gate leakage currents measured when $V_S = V_R = 0$ as defined in the equivalent circuit of figure 4.8.c.

and from the gate to the reference $R_{GR}(\Delta V_{GR})$.
With an ideally polarizable gate electrode the gate-source R_{GS} and gate-reference R_{GR} interface resistances can be considered infinite and i_G, i_{GS} and i_{GR} neglected compared to the transmembrane current i_t, leading to $i_S \approx i_t \approx i_R$. In the experimental measurements, being the leakage currents not negligible any more, the transmembrane current must be derived based on the equivalent circuit of figure 4.8.c with the following equations:

$$i_S + i_{GS} = i_t \tag{4.2}$$

$$i_{GR} + i_{GS} = i_G \tag{4.3}$$

$$i_t + i_{GR} = i_R \tag{4.4}$$

4.5.3 Quantification of leakage currents

In order to determine the transmembrane current i_t from equations 4.2 and 4.4 it is necessary to quantify the leakages i_{GS} and i_{GR}. According to the equivalent circuit of figure 4.8.c, if $V_s = V_r = 0$V we can assume that the transmembrane current $i_t = 0$, and so $i_{GS} = -i_S$ and $i_{GR} = i_R$ can be directly measured.
From the full matrix of experiments $i_G(V_S, V_G)$, $i_R(V_S, V_G)$ and $i_S(V_S, V_G)$, the I-V characteristic of both interfaces were measured by imposing

$$i_{GS}(V_{GS}) = i_S(V_S = 0, V_G) \tag{4.5}$$

$$i_{GR}(V_{GR}) = i_R(V_S = 0, V_G) \tag{4.6}$$

.

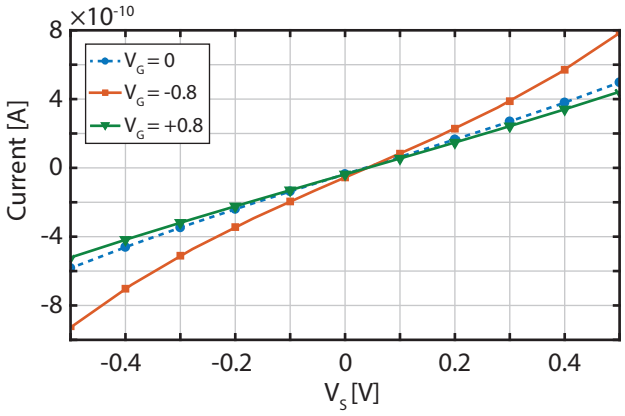

Figure 4.10 – Calculated transmembrane current i_t versus the transmembrane voltage V_S at three different gate voltages V_G.

The transmembrane current can thus be derived in two different ways, either by adding the leakage i_{GS} to the source current measured (equation 4.2) or by removing the leakage i_{GR} from the current measured at the reference (equation 4.4). The calculations were based on the measurements at the reference electrode (i.e. on equation 4.4 and 4.6) for the two following reasons: first, as shown in figure 4.9, the measured I-V characteristic of the leak i_{GR} rightfully cross the origin, whereas i_{GS} has a clear offset, probably due to remanent capacitive current. Second, the leakages i_{GS} and i_{GR} have both been measured and characterized within a window of voltages $V_{GS} = V_{GR} = \pm 0{,}8\,\mathrm{V}$. However, V_{GS} can reach higher voltages than ΔV_{GR}, up to $\pm 1{,}3\,\mathrm{V}$, for which i_{GS} has not been measured. This is not happening in the case of i_{GR} since it depends on $V_{GR} \equiv V_G = \pm 0{,}8\,\mathrm{V}$. The transmembrane current i_t can thus be derived by combining equations 4.4 and 4.6 as

$$i_t(V_S, V_G) = i_R(V_S, V_G) - i_{GR}(V_G) \equiv i_R(V_S, V_G) - i_R(V_S = 0, V_G) \tag{4.7}$$

4.6 Results and discussion

4.6.1 Test description

In order to demonstrate the modulation of the transmembrane current i_t by the gate voltage, membranes with 5 different nanopores geomeries were fabricated. Membranes with pore dimensions of 30 nm and 40 nm were obtained through wavy templates whereas membranes with pore dimensions of 50 nm, 60 nm and 70 nm were obtained with columnar templates. Each membrane had 49 nanopores disposed in an hexagonal lattice and spaced 3 µm from each other. All nanopores had the same lenght of 800 nm since they were produced on the same wafer. (Figure 4.11)

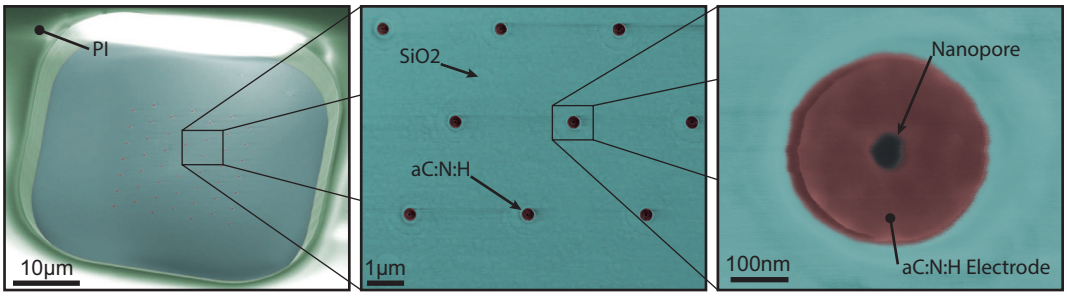

Figure 4.11 – Colored SEM micrographs showing the final result of the fabrication of a nanoporous membrane with nanopores 50 nm in diameter. Left - Tilted overview of the membrane where the 5 µm thick PI insulation surrounding the nanopores is visible. Center- Magnification on the nanopore array, which highlights the regularly spaced hexagonal lattice of a-C:N:H nanopores enclosed in the SiO_2 matrix. Right - Further enlargement of one single 50 nm nanopore, showing the a-C:N:H electrode in red and the surrounding SiO_2 in light blue.

4.6.2 Results

Each chip was tested in a low a ionic strength solution of KCl at 1×10^{-1} mM. The transmembrane current i_t was then calculated for each of the 5 chips as a function of the applied gate voltage. Figure 4.10 shows the transmembrane current i_t of a membrane with 50 nm nanopores as a function of the transmembrane voltage V_S at 3 different gate voltages (−0,8 V, 0 V and 0,8 V). At $V_G = -0{,}8$ V the I-V characteristic is steeper than at the two others voltages and the transmembrane conductance larger. In order to quantify the dependence of the transmembrane conductivity with the gate V_G and transmembrane V_S voltages, a modulation factor MF was computed representing the increase in conductance of the membrane with respect to the nanopore conductivity when the gate is at $V_G = 0$.

$$MF(V_S, V_G) = \frac{i_t(V_S, V_G) - i_t(V_S, V_G = 0)}{i_t(V_S, V_G = 0)} \tag{4.8}$$

Figure 4.12.a shows the modulation factor MF as a function of both V_S and V_G for each of the 5 tested nanopore dimensions. Based on these results two observations can be made: First, the magnitude of the modulation is more important in nanopores with small critical dimensions since the EDL overlap, responsible for ionic enrichment of the nanopore, is larger. The Debye length for the solution of 1×10^{-1} mM KCl used is equal to $\lambda_D = 30$ nm; which is coherent with our observations since the modulation can be noticed for critical dimensions smaller than $2\lambda_D \approx 60$ nm. Second, the modulation depends mostly on the applied gate voltage and not on the source voltage since the contour plots are mostly horizontal, thus proving that the modulation of the transmembrane current depends on the nanopore surface charge.
The evolution of the modulation factor with the gate voltage is shown in figure 4.12.b for different nanopore dimensions. As expected the modulation is directly proportional to the gate voltage and inversely proportional to the channel dimension. Figure 4.12.c shows the

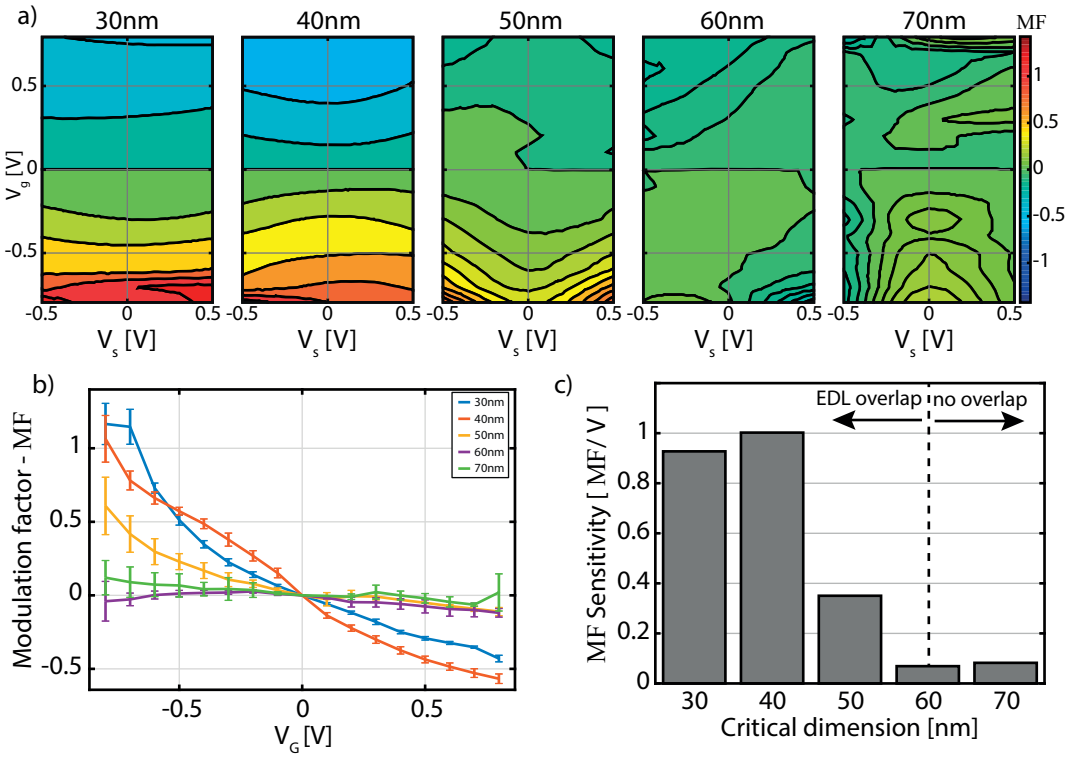

Figure 4.12 – a) Contour plot of the relative modulation factor $MF(V_S, V_G) = \frac{i_t(V_S,V_G) - i_t(V_S,V_G=0)}{i_t(V_S,V_G=0)}$ as a function of both V_G and V_S for 5 different chips with increasing critical dimensions, from 30 nm to 70 nm. b) Relative modulation extracted from figure 4.12.a versus of the applied gate voltage at different nanopore critical dimensions. c) Comparison of the modulation factor as a function of the applied gate voltage. The magnitude of the modulation factor clearly depends on the overlap of the EDL.

average modulation factor per volt for nanopores of different critical dimensions calculated as the slope of the linear interpolation of the curves in figure 4.12.b. For dimensions smaller than $2 \times \lambda_D$ the modulation is significant.

Control experiments These tests were repeated with new nanoporous membranes with the same critical dimensions but at high ionic strength, with a solution of 1×10^3 mM KCl. At that ionic strength the Debye length is $\lambda_D = 0{,}3$ nm and therefore no EDL overlap is present inside the nanopores used. The average relative modulation measured of 0,0032 MF/V is 3 orders of magnitude smaller than the relative modulation we calculated at low ionic strength, coherently with our expectations.

The precision of the recording setup was measured in two independent ways. First the input noise of the semiconductor analyzer we used was measured to be some hundreds of femtoampere. Second the sum of currents was calculated as $I_{tot} = I_s + I_g + I_r = -5{,}26\,\text{pA} \pm 5{,}13$. Those two results exclude any significative contribution from external sources of current such as inductive coupling or chemical reactions to our measurements.

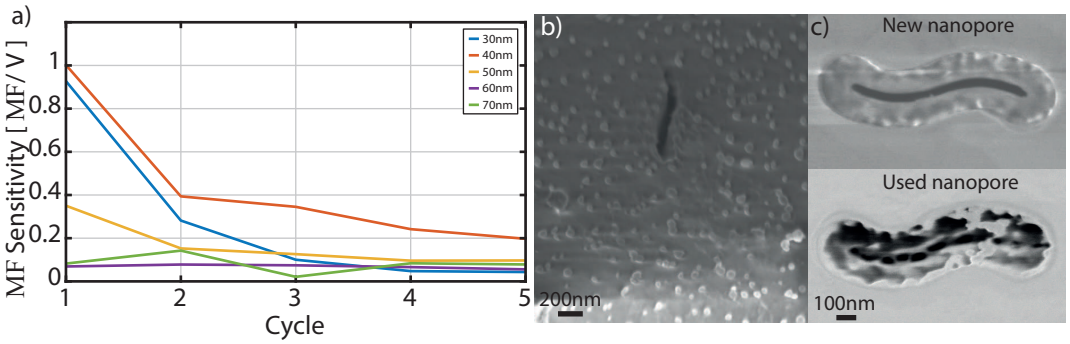

Figure 4.13 – Analysis of the degradation of the modulation factor with time and its causes. a) Evolution of the modulation factor MF during 5 consecutive measurement cycles in the case of nanopores of different critical dimensions. b) Micrograph of the backside of the membrane (the side with the biggest a-C:N:H surface exposed) which shows the deposition of a contamination on the electrode. c) The origin of this contamination is of electrochemical nature since only the a-C:N:H electrode appears to be contaminated.

4.6.3 Electrode stability over time

To investigate the evolution of the MF with time, five full cycles of experiments were performed consecutively, each cycle consisting of a measurement of the transmembrane conductivity at low ionic strength of all combinations of gate and source voltage, with a stabilization time of 45 s spent before each measurement, for a total length of the experiment of 23h30' for each membrane. Figure 4.13.a shows a decrease of the modulation factor with time, regardless of the nanopore dimensions. A closer look to the currents i_S, i_G, and i_R shows that all the values decrease over time, and this in a more pronounced way for membranes with smaller nanopores. SEM inspection of the surface of the nanopores after the experiments revealed the presence of an irregular film of contamination, deposited exclusively on the a-C:N:H electrodes and not on the supporting SiO_2. Figure 4.13 shows the contamination on the backside (4.13.b) and frontside (4.13.c) of the membrane. The backside of the membrane is entirely made of a-C:N:H and therefore is completely covered with contaminations while the front side shows the presence of the contaminations only on the electroactive carbon layer demonstrating how the growth of this unwanted layer progressively clogs the nanopores.
The nature of this contamination was investigated with energy-dispersive X-ray spectroscopy (EDX), revealing a high Ag content as shown in figure 4.14. This contamination was therefore identified as Ag leakage from the Ag/AgCl pseudo reference electrodes. Leakage of Ag^+ and AgCl nanoparticles from chloridized Ag wires has been reported and characterized in the literature, and can occur as fast as 5 min after the introduction of the electrode in the buffer.[127] This contamination of the buffer is expected to occur because of the instability of the chloride surface, limited polarization of the electrode and mechanical stress. In the case of the SEM micrograph shown in Figure 4.13, the shape and size of the contamination are consistent

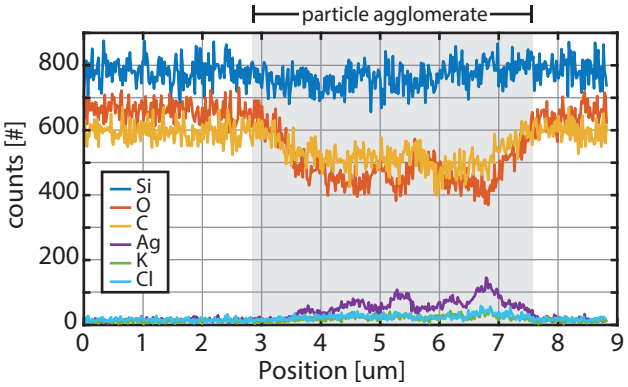

Figure 4.14 – EDX linescan of a particle agglomerate showing the presence of Ag.

with the electrodeposition of Ag particles at the surface, triggered by nucleation at specific adsorption sites of the electrode,[128] thus possibly hinting at the deposition of Ag particles rather than AgCl.
This contamination is coherent with the generalized decrease of currents and modulation factor that we previously observed. Figure 4.13.c reveals that the particles are located at the entrance and in the *lumen* of the pore, thus reducing the section of the nanopore and decreasing the transmembrane current measured. This effect is more pronounced for small nanopores since the variation of the nanopore section is greater for nanopores with smaller critical dimension.
Moreover, the contamination can alter the modulation of the surface charge, as metal electrodes typically have a shorter stability window than a-C:N:H surfaces, opening the possibility to the formation of bubbles or metal oxides. This would partially block the gate, decrease the gate leakage currents and attenuate the modulation factor coherently with the observations previously mentioned.
Several technical solutions can limit the sensitivity of the device to contamination. Principally, the Ag/AgCl electrodes can be coated with a porous protective material to avoid pollution of the buffer while allowing ionic exchange with the electrolyte. Nafion layers,[129] or agarose gels [130] have already been proposed. Using a complete reference electrode, fitted with a porous saline bridge, is another possibility. Overall, separating the reference electrode from the nanopore device with gels or membranes will limit the contamination by slowing or blocking the diffusion of the contaminants while allowing for using a higher chloride concentration at the vicinity of the reference, thus increasing its stability.

4.7 Discussion

The use of a polarizable gate electrode instead of a metal-oxide gate electrode strongly increases the sensitivity of the modulation factor to the gate voltage. This results in a modulation which is twice as large as other reported values for nanofluidic transistors under similar conditions (up to 1 as presented here, compared to about 0.5 as reported in the literature[30]),

obtained with small gate voltages. The sensitivity of the transmembrane current to the variations of gate voltage we could measure with polarizable nanopores is 2-3 orders of magnitude larger than the ones reported in the literature and obtained with SiO_2 insulated gates at similar experimental conditions where typical values are in the order of 0,02 MF/V to 0,002 MF/V.[30], [31], [131]
The non-ideal polarizability of the gate electrode is currently the main limitation for application since the current leak results in an important degradation of the sensitivity of the transmembrane current to the gate voltage throughout its use. Such leakages can be reduced by using a material with a higher interface resistance within the polarization window and lower backgrounds currents, such as BDD, a high-performance electrode material.[121] The higher modulation factor at low gate voltages and the degradation of the electrodes performances due to the injection of current at the gate are consistent with the observations of previous work where polarizable electrodes were used to modulate electroosmotic flow in a microchannel.[111] It is worth mentioning that even in that case the electrodes made of sputtered carbon have demonstrated the best modulation factors compared to electrodes made of SiC and Al, with an absolute magnitude similar to the one we observed ($MF = 0{,}5$), which degrades with the use.
Electrochemical reactions at the gate electrode are undesired for applications such as electrostatic gating but, on the other hand, could be used to fabricate biochemical sensors that exploit this variation of transmembrane current and gate leakages as working principle, similarly to the functioning of Coulter counters.[54] Importantly, the method used to fabricate the membranes can be easily adapted to build nanopores made of other materials, this way facilitating either the grafting of a selective molecule inside the nanopore or the integration of an electrode with optimal electrochemical affinity for the analyte. Nanoelectrodes are attracting interest as potential tools for single particle or single molecule electrochemistry.[132] Some examples of recessed nanoelectrodes have been reported in the literature, hinting that the current measured at these devices is mostly controlled by the geometry of the pore,[133] and electrochemistry coupled to nanopores has been used for single molecule sensing.[134] In this context, fabricating a nanopore membrane with a well-chosen, highly conductive material could be used for trace analysis or the quantitative detection of electroactive nanoparticles. The method presented here allows for the fabrictaion of well-structured, high-density array of open nanopores with a conductive *lumen* surface. From an analytical perspective, this opens the possibility to force the analyte through the pore, here used as an electrode. The small electrode dimension, possibly coupled to convection, would dramatically constrict the thickness of the diffusion layer, thus paving the way for lower limits of detection and opening opportunities in single molecule sensing.

Recently the research trend in nanofluidic solid-state membranes was toward the fabrication and study of molecularly thin solid-state membranes.[135] Membranes with short nanopores exhibit small fluidic resistance which demonstrated outstanding power generation through osmotic pressure[136], high-performance electroosmotic pumps[22] and high flows for charge- and size based- separation[137]. The interest in long nanopores has been shown in one

analysis from Vlassiouk and coworkers where was highlighted the impact of the geometry and surface charge of the nanochannel on its selectivity.[138] Thicker membranes with long nanopores in the range of 1 µm possess better permselectivity than short ones as well as highly charged nanopores compared to weakly charged nanopores. The membranes presented in this thesis follow this direction by enabling the fabrication of high aspect-ratio and polarizable nanochannels allowing to reach higher surface charge than metal-oxide gates or than passive nanochannels with naturally charged surfaces. Furthermore, thicker membranes provide better mechanical resistance and are easier to handle and inspect compared to molecularly thin ones.

4.8 Conclusions

In this chapter was demonstrated the fabrication and testing of voltage gated nanoporous membranes made of polarizable a-C:N:H. The manufacturing of these membranes was made possible using the process based on coating of sacrifical silicon nanostructures presented in chapter 2, that allows to finely control both the placement and geometry of nanopores made of a-C:N:H and to electrically contact them to an external voltage source. The use of a-C:N:H, a polarizable material, demonstrated the possibility to actively modulate the conductivity of the nanopores through an external voltage with a sensitivity to the gate voltage 2-3 orders of magnitude larger than other metal-oxide gate technologies. The modulation factor has been proven to be dependent from the nanopore critical dimension given the greater EDL overlap at smaller dimensions. However, the non-ideal polarizability of the a-C:N:H used is still a limiting factor since the leak current observed complicated the measurements and degraded the sensitivity of the transmembrane current to the gate voltage over time.

5 Conclusion

Nanofluidics is the study of liquids when confined in dimensions smaller than 100 nm. At such small dimension the surface effects take over the bulk properties of the liquid resulting in peculiar effects such as ionic exclusion. The evolution of micro-manufacturing techniques has recently enabled the controlled fabrication of nanochannels which demonstrated applications in filtration of solutions, pre-concentration of analytes, particle analysis and control of ionic flows with nanofluidic transistors or diodes.
However, being nanofluidics a relatively recent field of research, its potential applications are still vastly unexplored. One of the elements retaining its development are the lack of manufacturing methods for nanochannels providing the necessary freedom in engineering the nanofluidic devices.
The first part of this work directly addressed this issue and presented a novel micro-fabrication process for nanoporous membranes providing greater flexibility in the design of the nanopores. The second part of the thesis used this micro-fabrication technology to fabricate a nanoporous membrane which nanopores are made of a polarizable material. This allowed to fabricate a nanoporous membrane electrostatically gated able to actively control the ionic flow through its nanopores.

5.1 Summary of results

Fabrication of nanoporous membranes The first part of the thesis describes a novel wafer-scale technical solution for the fabrication of nanoporous membranes based on sacrificial templates. The developed technology allow to fabricate nanoporous membranes with arbitrarily controlled porosity, pore geometry, thickness, and material composition. The process is based on two major ideas. First, the nanopores are casted through a Si template and not etched in a film as most of other processes do. This allows to take advantage of the well known technology for structuring silicon and its numerous technical developments. Second, the use of XeF_2 gas phase etch to remove the Si template results in the process being compatible with a wide range of materials thanks to the high selectivity of the XeF_2 etch to silicon.

The use of well developed DRIE processes for Si etch allow to obtain high aspect ratio nanostructures. Circular templates 1 µm tall were fabricated with diameters down to 40 nm resulting in a maximal aspect-ratio of about 35. It was further demonstrated that templates with elongated and wavy geomery are more stable, allowing to reach critical dimensions down to 20 nm for heights up to 2,4 µm. The use of evaporation to cast the membrane results in conical nanopores with minimal critical dimension of 50 nm but offers to the possibility to stack multiple layers to fabricate the membrane, which is potentially useful to integrate multiple electrodes in the nanochannel. On the other hand the use of conformal methods such as sputtering or CVD to cast the membrane results in nanopores which shape is the exact negative of the silicon template, and therefore can be as small as 30 nm, but which interface nanopore-electrolyte is entirely made of the same material.

Voltage gated nanopore with polarizable gate The second part of the thesis demonstrates the fabrication of a voltage gated nanoporous membrane with polarizable gate made of a-C:N:H. The manufacturing of this device was possible only through the use of sacrificial silicon templates, the amorphous carbon being too delicate to be structured otherwise. The material for the gate electrode was chosen among different options considering its polarizability window, the intrisic stress of the film and its deposition method. However the a-C:N:H used, when integrated in the nanoporous membrane, demonstrated leakage currents in the same order of magnitude as the transmembrane current measured. This resulted in a indirect quantification of the dependance of the transmembrane current from the gate voltage, which typically characterize a transistor. Furthermore the presence of non-negligible leakage currents from the gate caused the deposition of a layer of contamination on the electrode that deteriorated the sensibility of the device to the gate voltage and decreased the *lumen* of the pore. Even with this limitation the use of a polarizable material demonstrated to be advantageous compared to common metal-oxide gates making the device two to three orders of magnitude more sensible to the variation of the gate potential while applying low gate voltages (< 800 mV).

5.2 Outlook

Natural continuation of this work would exploit the reliable micromanufacturing methods developed to test new materials for active nanochannels. In this work BDD was not used because requires expensive and technically challenging equipment not available in the lab but, preliminary tests show that the wavy sacrifical templates resist the wet seeding process required for the deposition of BDD films. This is especially interesting because BDD would exhibit higher conductivity and greater interface resistance as well as greater mechanical robustness than the a-C:N:H used. One other important property of BDD electrodes is their ability to change surface termination, from H-terminated (hydrophobic) to OH-terminated (hydrophillic) according to the overpotential applied.[121] The ability to fabricate nanopores with BDD at

the interface with the electrolyte would therefore enable the fabrication of nanopores with controlled wettability, that would exhibit an almost infinite ON/OFF ratio independently from chemical properties of the electrolyte, and the EDL overlap.
The ability to precisely control by design the positioning and shape of each nanopore may be exploited to fabricate new sensors. More in detail, the ability to modify the section of the nanopore along the pore axis, for example by controlling the scallopping effect when etching the template with a Bosch DRIE, could be exploited to gather new insights on the shape of translocating particles based on the same principle as Coulter counters.
Furthermore, a thick and mechanically robust membrane with relatively big nanopores of 70 nm to 80 nm can be used as a support for molecularly thin membranes with smaller nanopores, tipically 1 nm to 5 nm. The molecularly thin membrane can be deposited and structured on top of unreleased nanopore, and then at the end of the process, only before use, the supporting template can be removed leaving suspended and untouched the thin membrane, so taking advantage of the high selectivity of XeF_2.
Finally, the technological solution developed to fabricate nanoporous membranes can be extended to application more oriented toward biology, where the highly controllable positioning and shape of the nanopore can be used to integrate nanopores in microfluidic channels for efficient and high throughput nanoelectroporation.[139]

A Fabrication details for the nanoporous membrane

Wafer preparation A SOI wafer with 2 µm of device layer, 1 µm of BOx and 525 µm of handle was first thermally oxidized for 1 µm then covered with 200 nm of Si_3N_4. The frontside of the wafer was then partially etched in a CHF_3/SF_6 plasma until 200 nm of thermal SiO_2 are left. The thermal oxide left frontside was then completely removed with a 10 min HF 49% wet etch, while leaving untouched both the SiO_2 and Si_3N_4 films backside. After thorough rinsing the resulting wafer is a SOI wafer with a thinned device layer (from 2 µm to 1 µm) from the growth and removal of the thermal oxide, 1 µm BOx, 525 µm handle and a stacked layers of 1 µm thermal SiO_2 and 200 nm backside. The SiO_2 layer is used in the last XeF_2 etch to protect the backside of the chips while the Si_3N_4 film is used as hard mask for KOH etch.

Sacrificial silicon templates A frontside e-beam lithography was done on the device layer to define the geometries of the templates. A negative tone e-beam resist (HSQ 6% Dow Corning, XR-1541-006) was used with a thickness of 140 nm with an exposure dose of 8500 $\mu C\,cm^{-1}$, grid resolution of 1 nm and a beam of 1 nA with a spot size of 4 nm. The sacrificial structures were then etched in the device silicon layer with a SF_6/C_4F_8 based plasma DRIE (adapted from [95]) to obtain the sacrificial siclicon templates. The details of this fabrication step are presented in section 2.2

Membrane materials deposition and planarization Two films of 250 nm of a-C:N:H and 2 µm of SiO_2 were then deposited on the templates through PECVD (a-C:N:H: 50 W of RF generator power, 800 mtorr deposition chamber pressure at a temperature of 45 °C for 40 min[100]. SiO_2: 20 W of RF generator power, 1500 mtorr deposition chamber pressure at a temperature of 300 °C for 40 min. Both materials on a Oxford PlasmaLab 100 reactor). The SiO_2 film was planarized and thinned to make the silicon templates surface from the surrounding materials as shown in figure 4.7.b using a combination of CMP and IBE. First a 1 min CMP is done frontside to level the wafer and remove the "bumps" resulting from the conformal deposition on top of the templates, then once a flat surface is obtained an IBE etch is done to uniformly erode the SiO_2 and a-C:N:H layer to uncover the silicon templates from the surrounding material.

CMP:ω_{head} = 65 rpm, ω_{plate} = 75 rpm, head pressure = 0,76 bar, Backside pressure = 0,76 bar, slurry 30N50 from KLEBOSOL, on a pad IC1000 from DOW with a specific gravity of 0.794. IBE: Veeco NEXUS IBE350, 600 W, incidence angle of 60°.

Gate contacts and PI insulation To fabricate the contacts for the a-C:N:H gate layer the follwing steps were performed: first a mask defining the 1 mm in diameter contact areas were defined through standard photolithography (AZ9260, 2 µm thick), then opened through the SiO_2 layer with a CHF_3/SF_6 plasma until the a-C:N:H layer is exposed. The 200 nm of Pt were then sputtered through a silicon stencil on the a-C:N:H openings to form the contacts. The frontside was then coated with 5 µm of PI. To promote the adhesion of PI on the SiO_2 the wafers were first dehydrated at 130 °C for 3 min, then a solution of VM561 2% in ethanol was spincoated and the wafer was dehydrated again at 130 °C for 3 min. PI2611 from Dupont was then spincoated at 3000 rpm then softbaked under nitrogen atmosphere at 300 °C. The PI layer was then structured with a thick photolithography (AZ9260, 8 µm thick) and anisotropic O_2 plasma etching. Photoresist was finally removed with 1165 remover to prevent damaging the PI layer. The result is sketched in figure 4.7.c.

Membrane release To finally release the membranes a combination of KOH, HF and XeF_2 was used. The Si_3N_4 and SiO_2 backside layers were structured with standard photolithography processes (2 µm of AZ9260) and etched with He/CHF_3 dry etch to expose the silicon of the handle layer. The wafer was mounted on a teflon chuck to protect the wafer frontside then etched in KOH (40% at 60 °C) for about 19 h until the etch stopped on the BOx layer. After rinsing in deionized wafer for 2 h at 70 °C to remove KOH residuals, the frontside was protected with a teflon chuck and its backside was etched in concentrated HF 49% for 2 min to remove the BOx exposed by the KOH. Finally to release the membranes from the sacrificial structures and remove the last nanometers of silicon, the chips were etched with pulsed XeF_2 gas (4 × 60 s at 2000 mtorr). The result is shown in figure 4.7.d.

Bibliography

[1] H. Daiguji, "Ion transport in nanofluidic channels", *Chemical Society reviews*, vol. 39, no. 3, pp. 901–911, 2010.

[2] G. M. Whitesides, "What comes next?", *Lab on a Chip*, vol. 11, no. 2, pp. 191–3, 2011.

[3] J. N. Israelachvili, *Electrostatic Forces between Surfaces in Liquids*, Third edit. Elsevier, 2011.

[4] B. J. Kirby, *Micro-and nanoscale fluid mechanics: transport in microfluidic devices*. Cambridge University Press, 2010.

[5] H. Miedema, M. Vrouenraets, J. Wierenga, W. Meijberg, G. Robillard, and B. Eisenberg, "A biological porin engineered into a molecular, nanofluidic diode", *Nano letters*, vol. 7, no. 9, pp. 5–10, 2007.

[6] J. Kudr, S. Skalickova, L. Nejdl, A. Moulick, B. Ruttkay-Nedecky, V. Adam, and R. Kizek, "Fabrication of solid-state nanopores and its perspectives", *Electrophoresis*, vol. 36, no. 19, pp. 2367–2379, 2015.

[7] X. Hou, H. Zhang, and L. Jiang, "Building bio-inspired artificial functional nanochannels: From symmetric to asymmetric modification", *Angewandte Chemie - International Edition*, vol. 51, no. 22, pp. 5296–5307, 2012.

[8] M. Tagliazucchi and I. Szleifer, "Transport mechanisms in nanopores and nanochannels: Can we mimic nature?", *Materials Today*, vol. 18, no. 3, pp. 131–142, 2015.

[9] P. Apel, "Track etching technique in membrane technology", *Radiation Measurements*, vol. 34, no. 1-6, pp. 559–566, 2001.

[10] K. A. Mauritz and R. B. Moore, "State of understanding of Nafion", *Chemical Reviews*, vol. 104, no. 10, pp. 4535–4585, 2004.

[11] R. Fan, S. Huh, R. Yan, J. Arnold, and P. Yang, "Gated proton transport in aligned mesoporous silica films.", *Nature materials*, vol. 7, no. 4, pp. 303–7, 2008.

[12] W. Sparreboom, A. Van den Berg, and J. C. T. Eijkel, "Principles and applications of nanofluidic transport.", *Nature nanotechnology*, vol. 4, no. 11, pp. 713–20, 2009.

[13] Z. Jiang and D. Stein, "Electrofluidic gating of a chemically reactive surface.", *Langmuir*, vol. 26, no. 11, pp. 8161–73, 2010.

[14] L. Bocquet and E. Charlaix, "Nanofluidics, from bulk to interfaces.", *Chemical Society reviews*, vol. 39, no. 3, pp. 1073–95, 2010.

[15] M. A. M. Gijs, "Will fluidic electronics take off?", *Nature nanotechnology*, vol. 2, no. May, pp. 268–270, 2007.

[16] D. Stein, M. Kruithof, and C. Dekker, "Surface-Charge-Governed Ion Transport in Nanofluidic Channels", *Physical Review Letters*, vol. 93, no. 3, p. 035 901, 2004.

[17] Y. Ma, L.-H. Yeh, and S. Qian, "pH-regulated ionic conductance in a nanopore", *Electrochemistry Communications*, vol. 43, pp. 91–94, 2014.

[18] R. B. Schoch, A. Bertsch, and P. Renaud, "PH-controlled diffusion of proteins with different pl values across a nanochannel on a chip", *Nano Letters*, vol. 6, no. 3, pp. 543–547, 2006.

[19] S. Yao, D. E. Hertzog, S. Zeng, J. C. Mikkelsen, and J. G. Santiago, "Porous glass electroosmotic pumps: Design and experiments", *Journal of Colloid and Interface Science*, vol. 268, no. 1, pp. 143–153, 2003.

[20] S. K. Vajandar, D. Xu, D. a. Markov, J. P. Wikswo, W. Hofmeister, and D. Li, "SiO2-coated porous anodic alumina membranes for high flow rate electroosmotic pumping", *Nanotechnology*, vol. 18, no. 27, p. 275 705, 2007.

[21] S. A. Miller and C. R. Martin, "Redox modulation of electroosmotic flow in a carbon nanotube membrane", *Journal of the American Chemical Society*, vol. 126, pp. 6226–6227, 2004.

[22] J. L. Snyder, J. Getpreecharsawas, D. Z. Fang, T. R. Gaborski, C. C. Striemer, P. M. Fauchet, D. a. Borkholder, and J. L. McGrath, "High-performance, low-voltage electroosmotic pumps with molecularly thin silicon nanomembranes.", *Proceedings of the National Academy of Sciences*, vol. 110, no. 46, pp. 18 425–30, 2013.

[23] I. V. Vlassiouk and Z. S. Siwy, "Nanofluidic diode.", *Nano letters*, vol. 7, no. 3, pp. 552–6, 2007.

[24] I. V. Vlassiouk, S. Smirnov, and Z. S. Siwy, "Nanofluidic ionic diodes. Comparison of analytical and numerical solutions.", *ACS nano*, vol. 2, no. 8, pp. 1589–602, 2008.

[25] L.-J. Cheng and L. J. Guo, "Ionic current rectification, breakdown, and switching in heterogeneous oxide nanofluidic devices.", *ACS nano*, vol. 3, no. 3, pp. 575–84, 2009.

[26] S. Wu, F. Wildhaber, O. Vazquez-Mena, A. Bertsch, J. Brugger, and P. Renaud, "Facile fabrication of nanofluidic diode membranes using anodic aluminium oxide.", *Nanoscale*, vol. 4, no. 18, pp. 5718–23, 2012.

[27] C. Wei, A. J. Bard, and S. W. Feldberg, "Current rectification at quartz nanopipet electrodes", *Analytical Chemistry*, vol. 69, no. 22, pp. 4627–4633, 1997.

[28] Z. S. Siwy, "Ion-Current Rectification in Nanopores and Nanotubes with Broken Symmetry", *Advanced Functional Materials*, vol. 16, no. 6, pp. 735–746, 2006.

[29] J. Cervera, B. Schiedt, R. Neumann, S. Mafé, and P. Ramírez, "Ionic conduction, rectification, and selectivity in single conical nanopores.", *The Journal of chemical physics*, vol. 124, no. 10, p. 104 706, 2006.

[30] R. Karnik, R. Fan, M. Yue, D. Li, P. Yang, and A. Majumdar, "Electrostatic control of ions and molecules in nanofluidic transistors.", *Nano letters*, vol. 5, no. 5, pp. 943–8, 2005.

[31] W. Guan, S. X. Li, and M. A. Reed, "Voltage gated ion and molecule transport in engineered nanochannels: theory, fabrication and applications", *Nanotechnology*, vol. 25, no. 12, p. 122 001, 2014.

[32] W. Guan, R. Fan, and M. a. Reed, "Field-effect reconfigurable nanofluidic ionic diodes.", *Nature communications*, vol. 2, p. 506, 2011.

[33] S. Wu, F. Wildhaber, A. Bertsch, J. Brugger, and P. Renaud, "Field effect modulated nanofluidic diode membrane based on Al2O3/W heterogeneous nanopore arrays", *Applied Physics Letters*, vol. 102, no. 21, p. 213 108, 2013.

[34] E. B. Kalman, I. V. Vlassiouk, and Z. S. Siwy, "Nanofluidic Bipolar Transistors", *Advanced Materials*, vol. 20, no. 2, pp. 293–297, 2008.

[35] M. E. Gracheva, D. V. Melnikov, and J.-P. Leburton, "Multilayered semiconductor membranes for nanopore ionic conductance modulation.", *ACS nano*, vol. 2, no. 11, pp. 2349–55, 2008.

[36] J. Bai, D. Wang, S.-W. Nam, H. Peng, R. Bruce, L. Gignac, M. Brink, E. Kratschmer, S. Rossnagel, P. Waggoner, K. Reuter, C. Wang, Y. Astier, V. Balagurusamy, B. Luan, Y. Kwark, E. Joseph, M. Guillorn, S. Polonsky, A. Royyuru, S. Papa Rao, and G. Stolovitzky, "Fabrication of sub-20 nm nanopore arrays in membranes with embedded metal electrodes at wafer scales.", *Nanoscale*, vol. 6, pp. 8900–6, 2014.

[37] S.-W. Nam, M. J. Rooks, K.-B. Kim, and S. M. Rossnagel, "Ionic field effect transistors with sub-10 nm multiple nanopores.", *Nano letters*, vol. 9, no. 5, pp. 2044–8, 2009.

[38] S. S. G. Varricchio, C. Hibert, A. Bertsch, and P. Renaud, "Fabrication of multilayered nanofluidic membranes through silicon templates", *Nanoscale*, vol. 7, no. 48, pp. 20 451–20 459, 2015.

[39] K. Scott, *Handbook of industrial membranes*, 2nd Editio. Elsevier, 1995.

[40] B. S. Lalia, V. Kochkodan, R. Hashaikeh, and N. Hilal, "A review on membrane fabrication: Structure, properties and performance relationship", *Desalination*, vol. 326, pp. 77–95, 2013.

[41] K. P. Lee, T. C. Arnot, and D. Mattia, "A review of reverse osmosis membrane materials for desalination-Development to date and future potential", *Journal of Membrane Science*, vol. 370, no. 1-2, pp. 1–22, 2011.

[42] G.-d. Kang and Y.-m. Cao, "Development of antifouling reverse osmosis membranes for water treatment: A review", *Water Research*, vol. 46, no. 3, pp. 584–600, 2012.

[43] A. W. Mohammad, Y. H. Teow, W. L. Ang, Y. T. Chung, D. L. Oatley-Radcliffe, and N. Hilal, "Nanofiltration membranes review: Recent advances and future prospects", *Desalination*, vol. 356, pp. 226–254, 2015.

[44] I. Xiarchos, D. Doulia, V. Gekas, and G. Tragardh, "Polymeric Ultrafiltration Membranes and Surfactants", *Separation and Purification Reviews*, vol. 32, no. 2, pp. 215–278, 2007.

[45] R. Van Reis and A. Zydney, "Membrane separations in biotechnology", *Current Opinion in Biotechnology*, vol. 12, no. 2, pp. 208–211, 2001.

[46] R. W. Baker, "Membrane Technology", in *Kirk-Othmer Encyclopedia of Chemical Technology*, vol. 26, John Wiley & Sons, Inc., 2000, pp. 20–21.

[47] M. Li and R. K. Anand, "Recent advancements in ion concentration polarization", *The Analyst*, vol. 141, no. 12, pp. 3496–3510, 2016.

[48] S. Y. Son, S. Lee, H. Lee, and S. J. Kim, "Engineered nanofluidic preconcentration devices by ion concentration polarization", *Biochip Journal*, vol. 10, no. 4, pp. 251–261, 2016.

[49] S. J. Kim, Y.-A. Song, and J. Han, "Nanofluidic concentration devices for biomolecules utilizing ion concentration polarization: theory, fabrication, and applications.", *Chemical Society reviews*, vol. 39, no. 3, pp. 912–922, 2010.

[50] Y. C. Wang, A. L. Stevens, and J. Han, "Million-fold preconcentration of proteins and peptides by nanofluidic filter", *Analytical Chemistry*, vol. 77, no. 14, pp. 4293–4299, 2005.

[51] S. Prakash, A. Piruska, E. N. Gatimu, P. W. Bohn, J. V. Sweedler, and M. A. Shannon, "Nanofluidics : Systems and Applications", *IEEE Sensors Journal*, vol. 8, no. 5, pp. 441–450, 2008.

[52] L. J. Steinbock and a. Radenovic, "The emergence of nanopores in next-generation sequencing", *Nanotechnology*, vol. 26, no. 7, p. 074 003, 2015.

[53] L. Rems, D. Kawale, L. James Lee, and P. E. Boukany, "Flow of DNA in micro/nanofluidics: From fundamentals to applications", *Biomicrofluidics*, vol. 10, no. 4, p. 043 403, 2016.

[54] W. H. Coulter, *Means for counting particles suspended in a fluid*, 1953.

[55] I. Makra and R. E. Gyurcsányi, "Electrochemical sensing with nanopores: A mini review", *Electrochemistry Communications*, vol. 43, pp. 55–59, 2014.

[56] B. M. Venkatesan and R. Bashir, "Nanopore sensors for nucleic acid analysis", *Nature Nanotechnology*, vol. 6, no. 10, pp. 615–624, 2011.

[57] W. Shi, A. K. Friedman, and L. A. Baker, "Nanopore Sensing", *Analytical Chemistry*, vol. 89, no. 1, pp. 157–188, 2017.

[58] M. Davenport, K. Healy, M. Pevarnik, N. Teslich, S. Cabrini, A. P. Morrison, Z. S. Siwy, and S. E. Létant, "The role of pore geometry in single nanoparticle detection", *ACS Nano*, vol. 6, no. 9, pp. 8366–8380, 2012.

[59] E. C. Yusko, B. R. Bruhn, O. M. Eggenberger, J. Houghtaling, R. C. Rollings, N. C. Walsh, S. Nandivada, M. Pindrus, A. R. Hall, D. Sept, J. Li, D. S. Kalonia, and M. Mayer, "Real-time shape approximation and fingerprinting of single proteins using a nanopore", *Nature Nanotechnology*, vol. 12, no. 4, pp. 360–367, 2016.

[60] D. Pedone, M. Firnkes, and U. Rant, "Data analysis of translocation events in nanopore experiments", *Analytical Chemistry*, vol. 81, no. 23, pp. 9689–9694, 2009.

[61] S. Shekar, D. J. Niedzwiecki, C. C. Chien, P. Ong, D. A. Fleischer, J. Lin, J. K. Rosenstein, M. Drndic, and K. L. Shepard, "Measurement of DNA translocation dynamics in a solid-state nanopore at 100 ns temporal resolution", *Nano Letters*, vol. 16, no. 7, pp. 4483–4489, 2016.

[62] C. Wang, Q. Fu, X. Wang, D. Kong, Q. Sheng, Y. Wang, Q. Chen, and J. Xue, "Atomic Layer Deposition Modified Track-Etched Conical Nanochannels for Protein Sensing", *Analytical Chemistry*, vol. 87, no. 16, pp. 8227–8233, 2015.

[63] Y. Liu and L. Yobas, "Slowing DNA Translocation in a Nanofluidic Field-Effect Transistor", *ACS Nano*, vol. 10, no. 4, pp. 3985–3994, 2016.

[64] R. Ren, Y. Zhang, B. P. Nadappuram, B. Akpinar, D. Klenerman, A. P. Ivanov, J. B. Edel, and Y. Korchev, "Nanopore extended field-effect transistor for selective single-molecule biosensing", *Nature Communications*, vol. 8, 2017.

[65] D. Brambilla, P. Luciani, and J. C. Leroux, "Breakthrough discoveries in drug delivery technologies: The next 30 years", *Journal of Controlled Release*, vol. 190, pp. 9–14, 2014.

[66] T. M. Allen and P. R. Cullis, "Liposomal drug delivery systems: From concept to clinical applications", *Advanced Drug Delivery Reviews*, vol. 65, no. 1, pp. 36–48, 2013.

[67] A. Wicki, D. Witzigmann, V. Balasubramanian, and J. Huwyler, "Nanomedicine in cancer therapy: Challenges, opportunities, and clinical applications", *Journal of Controlled Release*, vol. 200, pp. 138–157, 2015.

[68] A. C. Anselmo and S. Mitragotri, "An overview of clinical and commercial impact of drug delivery systems.", *Journal of controlled release*, vol. 190, pp. 15–28, 2014.

[69] P. D. Jones and M. Stelzle, "Can Nanofluidic Chemical Release Enable Fast, High Resolution Neurotransmitter-Based Neurostimulation?", *Frontiers in Neuroscience*, vol. 10, no. 138, 2016.

[70] C. Duan, W. Wang, and Q. Xie, "Fabrication of nanofluidic devices", *Biomicrofluidics*, vol. 7, no. 2, p. 026 501, 2013.

[71] M. Napoli, J. C. T. Eijkel, and S. Pennathur, "Nanofluidic technology for biomolecule applications: a critical review.", *Lab on a Chip*, vol. 10, no. 8, pp. 957–985, 2010.

[72] L. Bocquet and P. Tabeling, "Physics and technological aspects of nanofluidics.", *Lab on a Chip*, vol. 14, no. 17, pp. 3143–58, 2014.

[73] S. S. G. Varricchio, N. Piacentini, A. Bertsch, and P. Renaud, "Multimaterial Nanoporous Membranes Shaped through High Aspect-Ratio Sacrificial Silicon Nanostructures", *ACS Omega*, vol. 2, no. 6, pp. 2387–2394, 2017.

[74] A. Piruska, M. Gong, J. V. Sweedler, and P. W. Bohn, "Nanofluidics in chemical analysis.", *Chemical Society reviews*, vol. 39, no. 3, pp. 1060–72, 2010.

[75] X. Hou, "Smart Gating Multi-Scale Pore/Channel-Based Membranes", *Advanced Materials*, vol. 28, pp. 7049–7064, 2016.

[76] S. Chakarvarti, "Track-etch membranes enabled nano-/microtechnology: A review", *Radiation Measurements*, vol. 44, no. 9-10, pp. 1085–1092, 2009.

[77] J. K. Kim, S. Y. Yang, Y. Lee, and Y. Kim, "Functional nanomaterials based on block copolymer self-assembly", *Progress in Polymer Science*, vol. 35, no. 11, pp. 1325–1349, 2010.

[78] E. J. Vriezekolk, T. Kudernac, W. M. De Vos, and K. Nijmeijer, "Composite ultrafiltration membranes with tunable properties based on a self-assembling block copolymer/homopolymer system", *Journal of Polymer Science, Part B: Polymer Physics*, vol. 53, no. 21, pp. 1546–1558, 2015.

[79] J. Li, D. Stein, C. McMullan, D. Branton, M. J. Aziz, and J. Golovchenko, "Ion-beam sculpting at nanometre length scales.", *Nature*, vol. 412, no. 6843, pp. 166–169, 2001.

[80] Y. Xu and N. Matsumoto, "Flexible and in situ fabrication of nanochannels with high aspect ratios and nanopillar arrays in fused silica substrates utilizing focused ion beam", *RSC Advances*, vol. 5, no. 62, pp. 50 638–50 643, 2015.

[81] N. Sobel, C. Hess, M. Lukas, A. Spende, B. Stühn, M. E. Toimil-Molares, and C. Trautmann, "Conformal SiO2 coating of sub-100 nm diameter channels of polycarbonate etched ion-track channels by atomic layer deposition", *Beilstein Journal of Nanotechnology*, vol. 6, pp. 472–479, 2015.

[82] N. Cele and S. S. Ray, "Recent progress on nafion-based nanocomposite membranes for fuel cell applications", *Macromolecular Materials and Engineering*, vol. 294, no. 11, pp. 719–738, 2009.

[83] D. H. Choi, Y. D. Han, B. K. Lee, S. J. Choi, H. C. Yoon, D. S. Lee, and J. B. Yoon, "Use of a columnar metal thin film as a nanosieve with sub-10 nm pores", *Advanced Materials*, vol. 24, pp. 4408–4413, 2012.

[84] S. Chakarvarti and J. Vetter, "Template synthesis - A membrane based technology for generation of nano-/micro materials: a review", *Radiation Measurements*, vol. 29, no. 2, pp. 149–159, 1998.

[85] W.-H. Chu, R. Chin, T. Huen, and M. Ferrari, "Silicon membrane nanofilters from sacrificial oxide removal", *Journal of Microelectromechanical Systems*, vol. 8, no. 1, pp. 34–42, 1999.

[86] F. Martin, R. Walczak, A. Boiarski, M. Cohen, T. West, C. Cosentino, J. Shapiro, and M. Ferrari, "Tailoring width of microfabricated nanochannels to solute size can be used to control diffusion kinetics", *Journal of Controlled Release*, vol. 102, no. 1, pp. 123–133, 2005.

[87] M. Bassu, P. Holik, S. Schmitz, S. Steltenkamp, and T. P. Burg, "Continuous high throughput nanofluidic separation through tangential-flow vertical nanoslit arrays", *Lab on a Chip*, vol. 16, pp. 4546–4553, 2016.

[88] H. Gardeniers and A. Van den Berg, "Micro- and nanofluidic devices for environmental and biomedical applications", *International Journal of Environmental Analytical Chemistry*, vol. 84, no. 11, pp. 809–819, 2004.

[89] H. F. Winters and J. W. Coburn, "The etching of silicon with XeF2 vapor", *Applied Physics Letters*, vol. 34, no. 1979, pp. 70–73, 1979.

[90] K. R. Williams and R. S. Muller, "Etch Rates for Micromachining Processing", *Journal of Microelectromechanical systems*, vol. 5, no. 4, pp. 256–269, 1996.

[91] K. R. Williams, K. Gupta, and M. Wasilik, "Etch Rates for Micromachining Processing - Part II", *Journal of Microelectromechanical Systems*, vol. 12, no. 6, pp. 761–778, 2003.

[92] N. Megouda, G. Piret, E. Galopin, Y. Coffinier, T. Hadjersi, O. Elkechai, and R. Boukherroub, "Lithographically patterned silicon nanostructures on silicon substrates", *Applied Surface Science*, vol. 258, no. 16, pp. 6007–6012, 2012.

[93] Q. Yu, H. Liu, and H. Chen, "Vertical SiNWAs for biomedical and biotechnology applications", *Journal Of Materials Chemistry B*, vol. 2, no. 45, pp. 7849–7860, 2014.

[94] G. Singh, P. Stenberg, P. Vahima, M. Kuittinen, R. P. Yadav, and V. Janyani, "Hydrogen silsesquioxane (HSQ): a perfect negative tone resist for developing nanostructure patterns on a silicon platform", in *Proceedings of SPIE*, vol. 7927, 2011, p. 792 715.

[95] C. Hibert, J. O'Brien, B. McCarthy, A. M. Kelleher, B. O'Neill, and P. J. Hughes, "High Aspect Ratio Silicon Nanofabrication (HARSiN) Technology", in *MNE 2005: Proceedings of the 31st International Conference on Micro and Nano Engineering*, H. Loeschner, Ed., Wien: Elsevier Ltd, 2005.

[96] L. M. Murphy, "Linear feature detection and enhancement in noisy images via the Radon transform", *Pattern Recognition Letters*, vol. 4, no. September, pp. 279–284, 1986.

[97] J. Cervera, B. Schiedt, and P. Ramírez, "A Poisson/Nernst-Planck model for ionic transport through synthetic conical nanopores", *Europhysics Letters (EPL)*, vol. 71, no. 1, pp. 35–41, 2005.

[98] M. Zhang, T. A. Desai, and M. Ferrari, "Proteins and cells on PEG immobilized silicon surfaces", *Biomaterials*, vol. 19, no. 10, pp. 953–960, 1998.

[99] O. Peleg, M. Tagliazucchi, M. Kröger, Y. Rabin, and I. Szleifer, "Morphology control of hairy nanopores", *ACS nano*, vol. 5, no. 6, pp. 4737–4747, 2011.

[100] K. Kyzioł, S. Jonas, K. Tkacz-Śmiech, and K. Marszałek, "A role of parameters in RF PA CVD technology of a-C:N:H layers", *Vacuum*, vol. 82, no. 10, pp. 998–1002, 2008.

[101] Y. Tanaka, M. Furuta, K. Kuriyama, R. Kuwabara, Y. Katsuki, T. Kondo, A. Fujishima, and K. Honda, "Electrochemical properties of N-doped hydrogenated amorphous carbon films fabricated by plasma-enhanced chemical vapor deposition methods", *Electrochimica Acta*, vol. 56, no. 3, pp. 1172–1181, 2011.

[102] C. C. Wong, A. Agarwal, N. Balasubramanian, and D. L. Kwong, "Fabrication of self-sealed circular nano/microfluidic channels in glass substrates.", *Nanotechnology*, vol. 18, no. 13, p. 135 304, 2007.

[103] J. Hall, "Access Resistance of a Small Circular Pore", *Journal of General Physiology*, vol. 66, no. 2, pp. 531–532, 1975.

[104] A. Plecis, R. B. Schoch, and P. Renaud, "Ionic transport phenomena in nanofluidics: experimental and theoretical study of the exclusion-enrichment effect on a chip.", *Nano letters*, vol. 5, no. 6, pp. 1147–55, 2005.

[105] R. B. Schoch, J. Han, and P. Renaud, "Transport phenomena in nanofluidics", *Reviews of Modern Physics*, vol. 80, no. 3, pp. 839–883, 2008.

[106] Y. Qiu, P. Hinkle, C. Yang, H. E. Bakker, M. Schiel, H. Wang, D. V. Melnikov, M. E. Gracheva, M. E. Toimil-Molares, A. Imhof, and Z. S. Siwy, "Pores with Longitudinal Irregularities Distinguish Objects by Shape", *ACS Nano*, vol. 9, no. 4, pp. 4390–4397, 2015.

[107] B. Wu, A. Kumar, and S. Pamarthy, "High aspect ratio silicon etch: A review", *Journal of Applied Physics*, vol. 108, no. 5, p. 051 101, 2010.

[108] A. Zeng, V. F. Neto, J. J. Gracio, and Q. H. Fan, "Diamond-like carbon (DLC) films as electrochemical electrodes", *Diamond and Related Materials*, vol. 43, pp. 12–22, 2014.

[109] J. Robertson, *Diamond-Like Carbon Films, Properties and Applications*. Elsevier Ltd, 2014, vol. 3, pp. 101–139.

[110] Y. Pleskov, M. Krotova, V. Polyakov, A. Khomich, A. Rukovishnikov, B. Druz, and I. Zaritskiy, "Electrochemical behaviour of a-C:N:H films", *Journal of Electroanalytical Chemistry*, vol. 519, no. 1-2, pp. 60–64, 2002.

[111] A. Plecis, J. Tazid, a. Pallandre, P. Martinhon, C. Deslouis, Y. Chen, and a. M. Haghiri-Gosnet, "Flow field effect transistors with polarisable interface for EOF tunable microfluidic separation devices.", *Lab on a Chip*, vol. 10, no. 10, pp. 1245–1253, 2010.

[112] G. Pardon and W. van der Wijngaart, "Modeling and simulation of electrostatically gated nanochannels.", *Advances in colloid and interface science*, vol. 199-200C, pp. 78–94, 2013.

[113] V. M. Lobo, A. C. Ribeiro, and L. M. Verissimo, "Diffusion coefficients in aqueous solutions of potassium chloride at high and low concentrations", *Journal of Molecular Liquids*, vol. 78, no. 1-2, pp. 139–149, 1998.

[114] J. R. Rumble, "Aqueous solubility of inorganic compounds at various temperatures", in *CRC Handbook of Chemistry and Physics*, CRC Press/Taylor & Francis, Ed., 98th Editi, Boca Raton, FL, 2018, pp. 166–171.

[115] S. Thompson, P. Packan, and M. Bohr, "MOS Scaling : Transistor Challenges for the 21st Century", *Intel Technology Journal*, 1998.

[116] S. Kim, E. I. Ozalp, V. Sundar, J. G. Zhu, and J. A. Weldon, "Modeling of electrically controlled molecular diffusion in a nanofluidic channel", *Journal of Applied Physics*, vol. 118, no. 7, 2015.

[117] S. Ferro and A. De Battisti, "The 5-V Window of Polarizability of Fluorinated Diamond Electrodes in Aqueous Solutions", *Analytical Chemistry*, vol. 75, no. 24, pp. 7040–7042, 2003.

[118] M. Panizza and G. Cerisola, "Application of diamond electrodes to electrochemical processes", *Electrochimica Acta*, vol. 51, pp. 191–199, 2005.

[119] A. Kraft, "Doped diamond: A compact review on a new, versatile electrode material", *International Journal of Electrochemical Science*, vol. 2, no. 5, pp. 355–385, 2007.

[120] R. Trouillon and D. O'Hare, "Comparison of glassy carbon and boron doped diamond electrodes: Resistance to biofouling", *Electrochimica Acta*, vol. 55, no. 22, pp. 6586–6595, 2010.

[121] J. V. Macpherson, "A practical guide to using boron doped diamond in electrochemical research", *Physical Chemistry Chemical Physics*, vol. 17, pp. 2935–2949, 2015.

[122] N. Mutsukura and K. Miyatani, "Deposition of diamond-like carbon film in CH4-He r.f. plasma", *Diamond and Related Materials*, vol. 4, no. 4, pp. 342–345, 1995.

[123] a. Grill, "Electrical and optical properties of diamond-like carbon", *Thin Solid Films*, vol. 355, pp. 189–193, 1999.

[124] A. Grill, "Diamond-like carbon: state of the art", *Diamond and Related Materials*, vol. 8, no. 2-5, pp. 428–434, 1999.

[125] G. Fedosenko, a. Schwabedissen, J. Engemann, E. Braca, L. Valentini, and J. M. Kenny, "Pulsed PECVD deposition of diamond-like carbon films", *Diamond and Related Materials*, vol. 11, no. 3-6, pp. 1047–1052, 2002.

[126] K. Bewilogua and D. Hofmann, "History of diamond-like carbon films — From first experiments to worldwide applications", *Surface and Coatings Technology*, vol. 242, pp. 214–225, 2014.

[127] A. Yakushenko, D. Mayer, J. Buitenhuis, A. Offenhäusser, and B. Wolfrum, "Electrochemical artifacts originating from nanoparticle contamination by Ag/AgCl quasi-reference electrodes", *Lab on a Chip*, vol. 14, pp. 602–607, 2014.

[128] R. L. McCreery, "Advanced Carbon Electrode Materials for Molecular Electrochemistry", *Chemical reviews*, vol. 108, pp. 2646–2687, 2008.

[129] F. Moussy and D. J. Harrison, "Prevention of the Rapid Degradation of Subcutaneously Implanted Ag / AgCI Reference Electrodes Using Polymer Coatings", *Analytical Chemistry*, vol. 66, no. 5, pp. 674–679, 1994.

[130] I.-y. Huang, R.-s. Huang, and L.-h. Lo, "Improvement of integrated Ag / AgCl thin-film electrodes by KCl-gel coating for ISFET applications", *Sensors and Actuators B: Chemical*, vol. 94, pp. 53–64, 2003.

[131] R. Fan, M. Yue, R. Karnik, A. Majumdar, and P. Yang, "Polarity Switching and Transient Responses in Single Nanotube Nanofluidic Transistors", *Physical Review Letters*, vol. 95, no. 8, p. 086 607, 2005.

[132] J. T. Cox and B. Zhang, "Nanoelectrodes : Recent Advances and New Directions", *Annual Review of Analytical Chemistry*, vol. 5, pp. 253–72, 2012.

[133] B. Zhang, Y. Zhang, and H. S. White, "The Nanopore Electrode", *Analytical Chemistry*, vol. 76, no. 21, pp. 6229–6238, 2004.

[134] R. Gao, Y.-l. Ying, Y.-x. Hu, Y.-j. Li, and Y.-t. Long, "Wireless Bipolar Nanopore Electrode for Single Small Molecule Detection", *Analytical Chemistry*, vol. 89, pp. 7382–7387, 2017.

[135] L. Wang, M. S. H. Boutilier, P. R. Kidambi, D. Jang, N. G. Hadjiconstantinou, and R. Karnik, "Fundamental transport mechanisms, fabrication and potential applications of nanoporous atomically thin membranes", *Nature Nanotechnology*, vol. 12, no. 6, pp. 509–522, 2017.

[136] J. Feng, M. Graf, K. Liu, D. Ovchinnikov, D. Dumcenco, M. Heiranian, and V. Nandigana, "Single-layer MoS2 nanopores as nanopower generators", *Nature Publishing Group*, vol. 536, no. 7615, pp. 197–200, 2016.

[137] C. C. Striemer, T. R. Gaborski, J. L. McGrath, and P. M. Fauchet, "Charge- and size-based separation of macromolecules using ultrathin silicon membranes.", *Nature*, vol. 445, no. 7129, pp. 749–753, 2007.

[138] I. V. Vlassiouk, S. Smirnov, and Z. S. Siwy, "Ionic selectivity of single nanochannels.", *Nano letters*, vol. 8, no. 7, pp. 1978–85, 2008.

[139] X. Xie, A. M. Xu, S. Leal-Ortiz, Y. Cao, C. C. Garner, and N. A. Melosh, "Nanostraw-electroporation system for highly efficient intracellular delivery and transfection", *ACS Nano*, vol. 7, no. 5, pp. 4351–4358, 2013.

Acronyms

a-C:N:H	hydrogenated amorphous carbon–nitrogen
ALD	atomic layer deposition
AR	aspect ratio
BDD	boron doped diamond
BOx	buried oxide
BSA	bovine serum albumin
CD	critical dimension
CMi	EPFL Center of MicroNanoTechnology
CMP	chemical mechanical polishing
CVD	chemical vapor deposition
DLC	diamond-like carbon
DNA	deoxyribonucleic acid
DRIE	deep reactive ion etching
EBL	electron beam lithography
EDL	electric double layer
EDX	energy-dispersive X-ray spectroscopy
EOF	electroosmotic flow
EP	electrophoretic flow
FET	field effect transistor
FIB	focused ion beam
HOPG	highly oriented pyrolytic graphene
HSQ	hydrogen silsesquioxane

IBE	ion beam etcher
ICP	ion concentration polarization
ICP-RIE	inductively coupled plasma reactive ion etching
LF	low frequency
MEMS	micro electromechanical systems
PECVD	plasma enhanced chemical vapor deposition
PEG	polyethylene glycol
PET	polyethylene terephthalate
PI	Polyimide
PVD	physical vapor deposition
RF	radio frequency
RIE	reactive ion etching
SEM	scanning electron microscopy
SiNW	silicon nanowire
SOI	silicon-on-insulator

Av. Ruchonnet 9
CH-1003 Lausanne

stevarri@gmail.com

SKYPE : stefanovarricchio

Nationality: Swiss

June 1986, age 31

TECHNICAL SKILLS

PROJECT MANAGEMENT
PRINCE2 FOUNDATION

CLEANROOM TECHNOLOGIES

NANOSTRUCTURATION OF SILICON
RIE, IBE, CMP, XeF_2, wet etching

ELECTRON-BEAM LITHOGRAPHY

PHOTOLITHOGRAPHY
positive/negative and structural resists (SU8 and parylen-c)

ADVANCED METROLOGY
SEM, FIB, EDX, ellipsometry, profilometry

THIN FILM DEPOSITION
PVD, CVD and heterogeneous structures

MICROSCOPY
bright-field, fluorescence and confocal

ELECTRO-CHEMICAL SENSING
impedance spectroscopy, cyclic voltammetry, semiconductor analysis

SOFTWARES

- MatLab
- C/C++
- LabWin
- Comsol
- SolidWorks
- CleWin
- Catia
- ProEngineer

LANGUAGES

- native
- fluent
- average
- fluent
- basic

A1 A2 B1 B2 C1 C2

STEFANOVARRICCHIO

ENGINEER SPECIALIZED IN MICRO AND NANOTECHNOLOGIES

EDUCATION

2012-2017	Ph.D - Microsystems and Microelectronics	EPF LAUSANNE
2009-2011	Master of Science - Micro and Nano Systems Thesis at UNIVERSITY OF CALIFORNIA, BERKELEY Minor degree in biomedical technologies	EPF LAUSANNE
2005-2008	Bachelor of Science - Microengineering	EPF LAUSANNE

PROFESSIONAL EXPERIENCE

PH.D. CANDIDATE AND RESEARCH ASSISTANT — EPFL

2012-2017, Lausanne (CH)

Development, nano-fabrication and validation of a nanofluidic transistor, a device capable to selectively control flow of chemicals, that mimics fluid mechanics principles of living cells. Derivatives of this technology were used in side projects in the fields of photovoltaics and biosafety. The results were published in renowned scientific journals and presented at international conferences.

- **Development, management and presentation** of interdisciplinary projects applying nanotechnologies to electrochemistry and biology.
- **Extensive hands-on micromachining** and cleanroom experience.
- Experience in biosensing, cell manipulation and optical microscopy techniques including bright-field, fluorescence and confocal.
- Characterization of physical and electrochemical properties of varius material such as amorphous carbons, boron-doped diamonds (BDD) and metals.
- **International collaborations** with prominent research groups studying applications of nanostructures in research fields of Photovoltaics and Biosafety.
- Teaching assistant for “Electronics” , “Bio-Inspired AI” and “Biosensors” classes.
- **Faculty representative** during science popularization events and hiring days.

2 NEW TECHNOLOGIES DEVELOPED

2 RESEARCH PROJECTS COLLABORATIONS

2 ARTICLES PUBLISHED

SECTION DELEGATE

MAIN PUBLICATIONS

PATENTS

Maesani, Biasiucci and **Varricchio**, "Non-Invasive Drawable Electrode for Neuromuscular Electrical Stimulation and Biological Signal Sensing" **INTENTO SA, 2015**

SCIENTIFIC ARTICLES

Varricchio et al., "Fabrication of multilayered nanofluidic membranes through silicon templates", **Nanoscale**, 2015

Varricchio et al., "Multimaterial Nanoporous Membranes Shaped through High Aspect-Ratio Sacrifical Silicon Nanostructures", **ACS Omega**, 2017

CONFERENCES - TALKS

Varricchio et al., "Fabrication of nanoporous membranes through silicon templates : two different approaches", 5th Micro and Nano Flows Conference (**MNF 2016**), Milan, Italy

Varricchio et al., "Fabrication of solid-state nanoporous membranes made of amorphous carbon and SiO2 with high aspect-ratio nanopores" 43rd International conference on micro and nanoengineering (**MNE 2017**), Braga, Portugal

CONFERENCES - POSTERS

Varricchio et al., "Manufacturing of nanoporous membranes with sacrificial silicon structures", **Nano-BioTech-Montreux 2016**, Montreux, Switzerland

Varricchio et al., "Sub-30 nm, high aspect-ratio and monocrystalline Si nanoWires and nanoFins : fabrication and characterization", 43rd International conference on micro and nanoengineering (**MNE 2017**), Braga, Portugal

HOBBIES

ICEHOCKEY: 10 years as goalkeeper
MOUNTAIN: trekking and climbing
SQUASH: weekly
RUNNING: mostly to stay fit.

TECHNICAL CONSULTANT — INTENTO SA

2014-2017, Lausanne (CH)

As part of a team, I invented and patented an innovative wearable technology for neuromuscular electrical stimulation composed of a biocompatible hydrogel and a smart-garment. The technology showed greater comfort compared to the state-of-the-art without losses in electrical performances over extended period of use.

- Conception and design of a smart-garment.
- Development and characterization of biocompatible and conductive hydrogel.
- **Patent writing and filing.**

1 PATENT PUBLISHED

WEARABLE TECHNOLOGY

FABRICATION OUTSOURCING

DEVELOPMENT ENGINEER — ABIONIC SA

2010, Lausanne (CH)

Feasibility study and prototyping of an integrated FCS molecule detector exploiting nanoscale phenomena. Upon good results I was attributed a follow-up project as independent contractor about the design of a key component of the system.

- Reverse engineering and definition of data-sheet requirements.
- Electronic circuit design and close-loop control.
- Functional design of lab-on-a-chip component and outsourcing of prototype fabrication to a third partner. The design is still used.

CIRCUIT DESIGN

1 PROTOTYPE BUILT

FABRICATION OUTSOURCING

DEVELOPMENT ENGINEER - INTERNSHIP — ALLEGRO MICROSYSTEMS

2009, Annecy (FR)

Conception and fabrication of a rotating magnetic field simulator to provide clients with remote and rapid support on magnetic sensors.

- Magnetic and electric circuit dimensioning and characterization
- Closed-loop control and data processing
- User interface design

SIGNAL PROCESSING

MAGNETIC CIRCUIT DESIGN

USER INTERFACE DESIGN

C++

ADDITIONAL EXPERIENCES

- Master Thesis at **UC Berkeley** about design optimization of optical grating couplers through gradient-following algorithms based on adjoint optimization and genetic algorithms. The coupling **efficency improved from 25% to about 53%**.
- Member of EPFL team at the International Genetically Engineered Machine (iGEM) competition of 2010 organized by **MIT**. The aim of the project was to fight the spread of malaria by using genetically modified bacteria. **The project was awarded a Gold Medal and a "iGEMmers prize"**
- Former member of **Swiss Army** (mandatory duty is over).